Příloha 1

Chen, C. C. L., Deshmukh, S., Jessa, S., Hadjadj, D., Lisi, V., Andrade, A. F., **Vanova, K.**… Jabado, N. (2020). Histone H3.3G34-Mutant Interneuron Progenitors Co-opt PDGFRA for Gliomagenesis. ***Cell***, *183*(6), 1617-1633.e22 **[IF 41.58]**

Autorský podíl: Genetická a epigenetická testování – Sangerovo sekvenování, methylační array, identifikace patogenní mutace, zpracování příslušných klinických dat

Cell

Histone H3.3G34-Mutant Interneuron Progenitors Co-opt *PDGFRA* for Gliomagenesis

Graphical Abstract

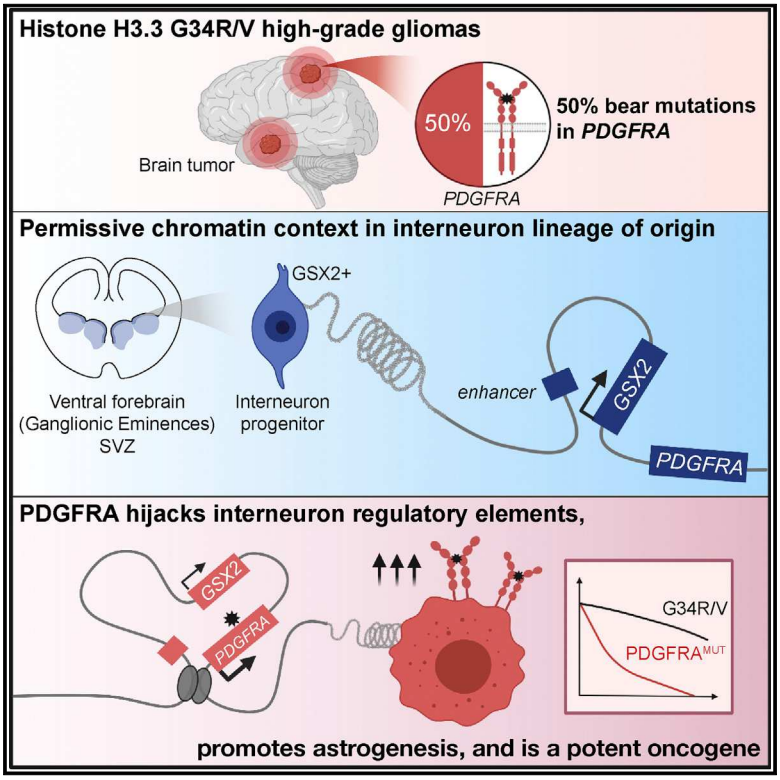

Highlights

- 50% of H3.3 G34R/V high-grade gliomas carry activating *PDGFRA* mutations
- G34R/V gliomas originate in *GSX2*-expressing interneuron progenitors
- *PDGFRA* co-opts *GSX2* enhancer elements for aberrant expression
- Mutant PDGFRA promotes astrogenesis and is a potent oncogenic driver, unlike G34R/V

Authors

Carol C.L. Chen, Shriya Deshmukh, Selin Jessa, ..., Paolo Salomoni, Claudia L. Kleinman, Nada Jabado

Correspondence

claudia.kleinman@mcgill.ca (C.L.K.), nada.jabado@mcgill.ca (N.J.)

In Brief

Lethal pediatric glioma arises from misregulation of interneuron differentiation.

Chen et al., 2020, Cell *183*, 1617–1633
December 10, 2020
https://doi.org/10.1016/j.cell.2020.11.012

CellPress

Cell

CellPress

Article

Histone H3.3G34-Mutant Interneuron Progenitors Co-opt *PDGFRA* for Gliomagenesis

Carol C.L. Chen,[1,47] Shriya Deshmukh,[2,47] Selin Jessa,[3,4,47] Djihad Hadjadj,[1,47] Véronique Lisi,[1] Augusto Faria Andrade,[1] Damien Faury,[5] Wajih Jawhar,[1] Rola Dali,[6] Hiromichi Suzuki,[7,8] Manav Pathania,[9,10,11] Deli A,[12] Frank Dubois,[13] Eleanor Woodward,[13] Steven Hébert,[1,4] Marie Coutelier,[1,4] Jason Karamchandani,[14] Steffen Albrecht,[15] Sebastian Brandner,[16] Nicolas De Jay,[1,4] Tenzin Gayden,[1] Andrea Bajic,[1] Ashot S. Harutyunyan,[5] Dylan M. Marchione,[17] Leonie G. Mikael,[5] Nikoleta Juretic,[5] Michele Zeinieh,[1] Caterina Russo,[5] Nicola Maestro,[11] Angelia V. Bassenden,[18] Peter Hauser,[19] József Virga,[20,21] Laszlo Bognar,[20] Almos Klekner,[20] Michal Zapotocky,[22] Ales Vicha,[22] Lenka Krskova,[23] Katerina Vanova,[22] Josef Zamecnik,[23] David Sumerauer,[22] Paul G. Ekert,[24] David S. Ziegler,[25,26] Benjamin Ellezam,[27] Mariella G. Filbin,[28] Mathieu Blanchette,[29] Jordan R. Hansford,[24] Dong-Anh Khuong-Quang,[30] Albert M. Berghuis,[18]

(Author list continued on next page)

[1]Department of Human Genetics, McGill University, Montreal, QC H3A 0C7, Canada
[2]Division of Experimental Medicine, Department of Medicine, McGill University, Montreal, QC H4A 3J1, Canada
[3]Quantitative Life Sciences, McGill University, Montreal, QC H3A 2A7, Canada
[4]Lady Davis Research Institute, Jewish General Hospital, Montreal, QC H3T 1E2, Canada
[5]Department of Pediatrics, McGill University, and The Research Institute of the McGill University Health Centre, Montreal, QC H4A 3J1, Canada
[6]Canadian Centre for Computational Genomics, McGill University, Montreal, QC H3A 0E9, Canada
[7]Developmental and Stem Cell Biology Program, The Hospital for Sick Children, Toronto, ON M5G 0A4, Canada
[8]The Arthur and Sonia Labatt Brain Tumour Research Centre, The Hospital for Sick Children, Toronto, ON M5G 0A4, Canada
[9]Department of Oncology and The Milner Institute, Jeffrey Cheah Biomedical Centre, University of Cambridge, Cambridge CB2 0AW, UK
[10]CRUK Children's Brain Tumour Centre of Excellence, University of Cambridge, Cambridge CB2 0RE, UK
[11]Samantha Dickson Brain Cancer Unit, University College London Cancer Institute, London, United Kingdom
[12]Nuclear Function in CNS Pathophysiology, German Center for Neurodegenerative Diseases (DZNE), Bonn 53127, Germany
[13]Dana-Farber/Boston Children's Cancer and Blood Disorders Center, Boston, MA, 02215, USA
[14]Department of Pathology, Montreal Neurological Institute, McGill University, Montreal, QC H3A 2B4, Canada
[15]Department of Pathology, Montreal Children's Hospital, McGill University Health Centre, Montreal, QC H4A 3J1, Canada
[16]UCL Queen Square Institute of Neurology, London WC1N 3BG, UK
[17]Department of Biochemistry and Biophysics and Penn Epigenetics Institute, Perelman School of Medicine, University of Pennsylvania, Philadelphia, PA 19104-6073, USA
[18]Department of Biochemistry, McGill University, Montreal, QC H3A 1A3, Canada
[19]Second Department of Paediatrics, Semmelweis University, Budapest 1094, Hungary

(Affiliations continued on next page)

SUMMARY

Histone H3.3 glycine 34 to arginine/valine (G34R/V) mutations drive deadly gliomas and show exquisite regional and temporal specificity, suggesting a developmental context permissive to their effects. Here we show that 50% of G34R/V tumors (n = 95) bear activating *PDGFRA* mutations that display strong selection pressure at recurrence. Although considered gliomas, G34R/V tumors actually arise in *GSX2*/*DLX*-expressing interneuron progenitors, where G34R/V mutations impair neuronal differentiation. The lineage of origin may facilitate *PDGFRA* co-option through a chromatin loop connecting *PDGFRA* to *GSX2* regulatory elements, promoting *PDGFRA* overexpression and mutation. At the single-cell level, G34R/V tumors harbor dual neuronal/astroglial identity and lack oligodendroglial programs, actively repressed by *GSX2*/*DLX*-mediated cell fate specification. G34R/V may become dispensable for tumor maintenance, whereas mutant-*PDGFRA* is potently oncogenic. Collectively, our results open novel research avenues in deadly tumors. G34R/V gliomas are neuronal malignancies where interneuron progenitors are stalled in differentiation by G34R/V mutations and malignant gliogenesis is promoted by co-option of a potentially targetable pathway, *PDGFRA* signaling.

INTRODUCTION

High-grade gliomas (HGGs) are deadly primary brain tumors and a leading cause of mortality in children and young adults. These tumors frequently harbor somatic mutations in genes encoding histone 3 (H3) variants or epigenetic modifiers with remarkable neuroanatomical and age specificity (Fontebasso et al., 2014b; Khuong-Quang et al., 2012; Schwartzentruber

Alexander G. Weil,[31] Benjamin A. Garcia,[17] Livia Garzia,[32,33] Stephen C. Mack,[34] Rameen Beroukhim,[35,36] Keith L. Ligon,[35,37] Michael D. Taylor,[7,8] Pratiti Bandopadhayay,[13,35,38] Christoph Kramm,[39] Stefan M. Pfister,[40,41,42] Andrey Korshunov,[43,44] Dominik Sturm,[39,45] David T.W. Jones,[44,46] Paolo Salomoni,[11,12] Claudia L. Kleinman,[1,4,*] and Nada Jabado[1,2,5,48,*]

[20]Department of Neurosurgery, University of Debrecen, Debrecen 4032, Hungary
[21]Department of Oncology, Faculty of Medicine, University of Debrecen, Debrecen 4032, Hungary
[22]Department of Paediatric Haematology and Oncology, Second Faculty of Medicine, Charles University and University Hospital Motol, Prague 150 06, Czech Republic
[23]Department of Pathology and Molecular Medicine, Second Faculty of Medicine, Charles University and University Hospital Motol, Prague 150 06, Czech Republic
[24]Children's Cancer Center, The Royal Children's Hospital; Murdoch Children's Research Institute; Department of Pediatrics, University of Melbourne, Parkville, VIC 3052, Australia
[25]Kids Cancer Centre, Sydney Children's Hospital, Randwick, NSW 2031, Australia
[26]School of Women's and Children's Health, UNSW Sydney, Kensington, NSW 2052, Australia
[27]Department of Pathology, Centre Hospitalier Universitaire Sainte-Justine, Université de Montréal, Montréal, QC H3T 1C5, Canada
[28]Department of Pediatric Oncology, Dana-Farber Boston Children's Cancer and Blood Disorders Center, Boston, MA 02215, USA
[29]School of Computer Science, McGill University, Montreal, QC H3A 2A7, Canada
[30]Children's Cancer Center, The Royal Children's Hospital; and Murdoch Children's Research Institute; Parkville, VIC 3052, Australia
[31]Department of Pediatric Neurosurgery, Centre Hospitalier Universitaire Sainte-Justine, Université de Montréal, Montréal, QC H3T 1C5, Canada
[32]Cancer Research Program, The Research Institute of the McGill University Health Centre, Montreal, QC H4A 3J1, Canada
[33]Division of Orthopedic Surgery, Faculty of Surgery, McGill University, Montreal, QC H3G 1A4, Canada
[34]Department of Pediatrics, Division of Hematology and Oncology, Texas Children's Cancer and Hematology Centers, Dan L. Duncan Cancer Center, Baylor College of Medicine, Houston, TX 77030, USA
[35]Department of Medical Oncology, Dana-Farber Cancer Institute, Boston, MA 02215-5450, USA
[36]Broad Institute of MIT and Harvard, Boston, MA 02142, USA
[37]Department of Pathology, Boston Children's Hospital and Brigham and Women's Hospital, Harvard Medical School, and Department of Oncologic Pathology, Dana-Farber Cancer Institute, Boston, MA 02115, USA
[38]Department of Pediatrics, Harvard Medical School, Boston, MA 02115, USA
[39]Division of Pediatric Hematology and Oncology, University Medical Center Goettingen, Goettingen 37075, Germany
[40]Hopp Children's Cancer Center Heidelberg (KiTZ) and Department of Pediatric Oncology, Hematology and Immunology, University Hospital Heidelberg, Heidelberg 69120, Germany
[41]Division of Pediatric Neurooncology, German Cancer Consortium (DKTK) and German Cancer Research Center (DKFZ), Heidelberg 69120, Germany
[42]Department of Pediatric Hematology and Oncology, Heidelberg University Hospital, Heidelberg 69120, Germany
[43]Department of Neuropathology, Institute of Pathology, University Hospital Heidelberg, Heidelberg 69120, Germany
[44]Clinical Cooperation Unit Neuropathology, German Cancer Consortium (DKTK), German Cancer Research Center (DKFZ), Heidelberg 69120, Germany
[45]Pediatric Glioma Research Group, German Cancer Research Center (DKFZ), 69120 Heidelberg, Germany
[46]Hopp Children's Cancer Center Heidelberg (KiTZ), Heidelberg 69120, Germany
[47]These authors contributed equally
[48]Lead Contact
*Correspondence: claudia.kleinman@mcgill.ca (C.L.K.), nada.jabado@mcgill.ca (N.J.)
https://doi.org/10.1016/j.cell.2020.11.012

et al., 2012; Sturm et al., 2012; Wu et al., 2012). HGGs in adolescents and young adults (12–35 years old) primarily occur in cerebral hemispheric lobes, and a large number are considered epigenetic disorders (Fontebasso et al., 2013, 2014a; Parsons et al., 2008; Verhaak et al., 2010). More than 30% of these HGGs bear heterozygous mutations in the non-canonical H3.3 variant, leading to glycine 34 to arginine or valine (G34R/V) amino acid substitutions (Fontebasso et al., 2014b; Schwartzentruber et al., 2012; Wu et al., 2012, 2014). G34R/V tumors are understudied and likely underestimated because their unique histopathological heterogeneity, with dual neuronal-glial compartments present at variable degrees, leads to misdiagnosis. Indeed, close to 30% of central nervous system primitive neuroectodermal tumors (CNS-PNETs), a now obsolete entity of mixed high-grade neuronal tumors (Sturm et al., 2016), have been shown to be G34R/V mutant HGGs (Gessi et al., 2013; Korshunov et al., 2016). At the molecular level, on the other hand, G34R/V HGGs show unifying features; they almost invariably carry mutations in alpha thalassemia/mental retardation syndrome X-linked (*ATRX*) and tumor protein p53 (*TP53*) (Korshunov et al., 2016; Liu et al., 2012; Schwartzentruber et al., 2012), lack immunoreactivity for the oligodendroglial marker OLIG2 (Sturm et al., 2012), and cluster distinctly from other glioma entities based on DNA methylation (Sturm et al., 2012). In contrast to lysine 27 to methionine (K27M) or lysine 36 to methionine (K36M) mutations that affect canonical H3.1/2 and H3.3 variants, G34R/V occur exclusively on the non-canonical H3.3 and have been suggested to act in *cis*, with the bulky amino acid replacement preventing post-translational modification of the neighboring H3.3K36 residue (Lewis et al., 2013) and/or its recognition by specific readers (Wen et al., 2014).

Limited information exists regarding oncogenic or developmental pathways in these tumors, hampering their modeling and development of therapeutic strategies. Compiling comprehensive cohorts to study their molecular landscape has been challenging because this age group spans pediatric and adult care and has a high rate of misdiagnosis. To address this knowledge gap, we assembled the largest cohort of G34R/V HGG tumors to date (n = 95), including primary/relapse pairs; comprehensively profiled them at the genomic, epigenomic, and transcriptomic (bulk and single-cell) levels; and developed *in vitro* and *in vivo* models. We delineate the unique molecular characteristics of G34R/V tumors, define their developmental origins, characterize inter- and intra-tumor heterogeneity, and uncover specific vulnerabilities that may be amenable to targeted therapies in this deadly cancer type.

RESULTS

High Frequency of PDGFRA Mutations in G34R/V HGGs

To define the genetic landscape of G34R/V HGGs, we assembled a multi-institutional cohort of G34R (72 at diagnosis, 8 recurrences) and G34V tumors (9 at diagnosis, 6 recurrences). We compared G34R/V mutation profiles with midline K27M HGGs and with the other hemispheric HGG subgroups occurring in children or adults younger than 50 years; namely, isocitrate dehydrogenase 1 (*IDH1*)- and/or SET domain containing 2 (*SETD2*) mutant HGGs or tumors wild-type for these mutations (Figure 1A; Table S1). In addition to the known genetic alterations in *TP53* and *ATRX* (95% and 84%, respectively), we observed a specific, previously unappreciated high frequency of mutations in platelet derived growth factor receptor alpha ((*PDGFRA*) in G34R/V HGGs (46 of 95) that also showed a high level of *PDGFRA* expression (Figure S1A). The high frequency at diagnosis (44%) was enriched further at recurrence (81%, p = 0.02, Fisher's exact test). Co-occurrence of G34R/V and *PDGFRA* mutations was 7- to 8-fold higher than in any other subgroup, where the highest observed $PDGFRA^{MUT}$ frequency was 7% (p = 2.8E–55, chi-square test). No other recurrent mutations (frequency >10%) were identified beyond *PDGFRA* (Figure S1B). In contrast to K27M HGGs (Khuong-Quang et al., 2012; Sturm et al., 2012; Wu et al., 2014), amplification of *PDGFRA* was relatively rare in G34R/V tumors (6 of 47, 13%) and similar in proportion to other hemispheric HGG subgroups, including *IDH1* mutant and IDH1/H3 wild type (p = 0.64, chi-square test).

PDGFRA is a class III receptor tyrosine kinase (RTK) with five extracellular immunoglobulin-like domains. Within G34R/V HGGs, 85% of *PDGFRA* mutations occurred in the second to fourth extracellular immunoglobulin-like domains (Figure 1B). In contrast, we rarely observed the D842V/Y mutations affecting an autoinhibition site in the kinase domain (n = 2), prevalent and well characterized in gastrointestinal stromal tumors (Heinrich et al., 2003). Most of these extracellular mutations have mainly been reported in brain tumors, particularly pediatric gliomas (Paugh et al., 2013), and are presumed to be activating (Ip et al., 2018; Paugh et al., 2013; Table S1). We performed in *silico* modeling of two extracellular mutations (Figure S1C): cysteine 235 to tyrosine/phenylalanine (C235Y/F), the most prevalent in our cohort (n = 15), and lysine 385 to methionine (K385M), which has been reported recently as the sole recurrent mutation in rare myxoid glioneuronal tumors (Solomon, 2018). Both mutations were predicted to lead to receptor dimerization and constitutive activation, analogous to the well-characterized Y288C mutation (Ip et al., 2018). Accordingly, we observed marked ERK phosphorylation, indicating downstream mitogen-activated protein kinase (MAPK)/ extracellular signal-regulated kinase (ERK) pathway activation in G34R/V-$PDGFRA^{MUT}$ tumors, whereas $PDGFRA^{WT}$ tumors showed limited ERK phosphorylation in cells not expressing this RTK (Figure 1C). Moreover, in one available primary/relapsed pair where the tumor acquired $PDGFRA^{K385M}$ at relapse, ERK phosphorylation was only present at relapse (Figure 1C). Collectively, these results suggest that PDGFRA mutations in G34R/V tumors promote constitutive activation of this RTK and its downstream signaling pathways.

Transcriptional and Epigenetic Programs in G34R/V Gliomas Indicate an Interneuron Progenitor Origin

The high co-occurrence of *PDGFRA* mutations with G34R/V suggests G34R/V context dependency, likely linked to development, as demonstrated recently for several related entities (Jessa et al., 2019; Vladoiu et al., 2019). To define the cellular lineage at the origin of G34R/V tumors, we first assessed cell type-specific signatures derived from single-cell RNA sequencing (scRNA-seq) atlases of forebrain development (Jessa et al., 2019; Nowakowski et al., 2017; Velmeshev et al., 2019) using gene set enrichment analysis (GSEA). Compared with other HGG entities, transcriptomes of G34R/V gliomas showed strong enrichment of the cortical interneuron lineage, including radial glia, neuronal progenitor, and interneuron gene programs, and were depleted of excitatory neuron and oligodendroglial signatures (Figure 2A; Figures S2A and S2B; Table S2). Consistent with the presence of a neuronal compartment, astrocyte gene programs were decreased relative to other gliomas but still highly enriched compared with non-glioma entities, such as high-grade neuroepithelial tumors with BCL6 corepressor (*BCOR*) alteration (HGNET-BCOR) (Figure S2C). Importantly, G34R/V tumors showed enrichment of prenatal but not postnatal interneuron signatures.

Cortical interneurons are generated during embryonic development in transient progenitor domains of the ventral telencephalon, called ganglionic eminences (GEs) (Hansen et al., 2013; Ma et al., 2013; Figure 2B). A network of transcription factors (TFs), including GS homeobox 2 (*GSX2*) and distal-less homeobox1/2 (*DLX1/2*), patterns these domains to specify interneuron fate. *GSX2* is expressed throughout the GEs but most highly in the lateral and caudal GEs, where it acts upstream of *DLX1/2.* All three factors (*GSX2* and *DLX1/2*) are required for interneuron specification and repression of oligodendroglial fate (Chapman et al., 2013; Petryniak et al., 2007). Postnatally, a *Gsx2*+ neural stem cell niche derived from its GE counterpart and regulated by a similar TF hierarchy persists in the murine brain, within the sub-ventricular zone (SVZ) (Chapman et al., 2018; López-Juárez et al., 2013). We thus extended our analysis to include two recently reported scRNA-seq SVZ datasets (Anderson et al., 2020; Mizrak et al., 2019), confirming that G34R/V HGGs significantly upregulated signatures of *Gsx2*+ SVZ progenitors (Figure 2C; Figure S2D). Consistent with GSEA results, G34R/V HGGs significantly

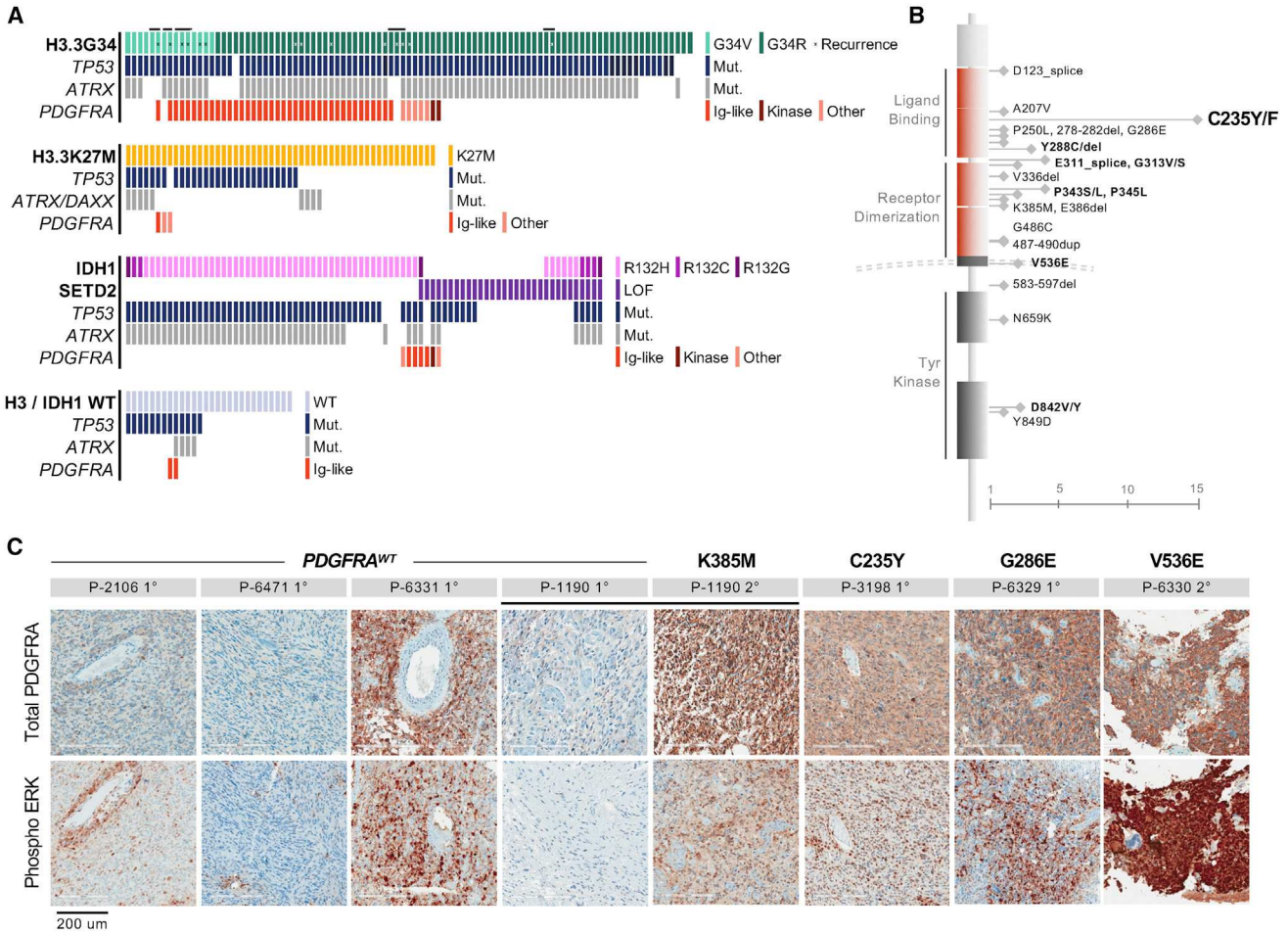

Figure 1. PDGFRA Is Frequently Mutated in G34R/V Tumors

(A) Oncoprint showing frequent occurrence of *PDGFRA* mutations in G34R/V (n = 95) relative to K27M (n = 53), IDH1/SETD2 (n = 80), and H3/IDH1 WT (n = 28) HGG subgroups (details in Table S1). Lines linking consecutive G34R/V samples indicate primary/recurrent tumors from the same individual.

(B) Spectrum and frequency of *PDGFRA* somatic mutations identified in G34R/V HGGs. Boldface indicates mutations observed in 2 or more individuals. Scale bar indicates number of individuals.

(C) Immunohistochemistry staining of total PDGFRA and phosphorylated ERK1/2 in G34R/V HGGs, separated by *PDGFRA* mutation status. A primary $PDGFRA^{WT}$ and recurrence $PDGFRA^{MUT}$ tumor pair (P-1190) is indicated. Scale bar indicates 200 μm.

See also Figure S1 and Table S1.

upregulated *GSX2*; the human radial glia marker *MOXD1* (Pollen et al., 2015); interneuron TFs, including *DLX1/2* (Figure 2D; Figure S2E); and the interneuron markers *GAD2*, *SCGN*, *NPY*, and *CALB2* (Ma et al., 2013; Raju et al., 2018). In contrast, they lacked expression of TFs specifying excitatory neurons, such as *EOMES* and *NEUROD2* (Figure S2E). This transcriptional profile was unique to G34R/V tumors; expression of forebrain interneuron TFs and gene signatures was absent not only in midline K27M tumors but also in other hemispheric HGGs. Thus, we conclude that, at the transcriptional level, G34R/V HGGs resemble *GSX2/DLX+* progenitors of the interneuron lineage.

We next assessed epigenomic profiles of G34R/V tumors, which were also consistent with an interneuron origin. *GSX2* and *DLX1/2* displayed an active chromatin conformation, enriched for the activating histone H3 lysine 27 acetylation (H3K27ac) mark and lacking the repressive histone H3 lysine 27 tri-methylation (H3K27me3) mark (Figure 2E; Table S3). On the other hand, gene sets enriched for H3K27me3 were related to neuronal synapse-, axon-, and ion channel-associated functions (e.g., *NTRK2*, *NXPH1*, and *CHRNA4*) (Figure S2F). The H3K27me3 and H3K27ac marks were absent from the promoter of the oligodendrocyte lineage factor *OLIG2* in G34R/V gliomas, in keeping with previous data showing it to be silenced through DNA methylation in this entity (Sturm et al., 2012; Figure 2E). Furthermore, G34R/V HGGs lacked activation of a core module of TFs necessary for oligodendrocyte specification (Figure S2G).

Finally, to confirm the match to immature interneuron progenitors, we extracted genes driving transcriptional enrichment of signatures in G34R/V tumors as well as genes displaying differential H3K27ac/me3 deposition and profiled their expression along a normal interneuron differentiation trajectory (Figure 2F). G34R/V-upregulated genes were primarily

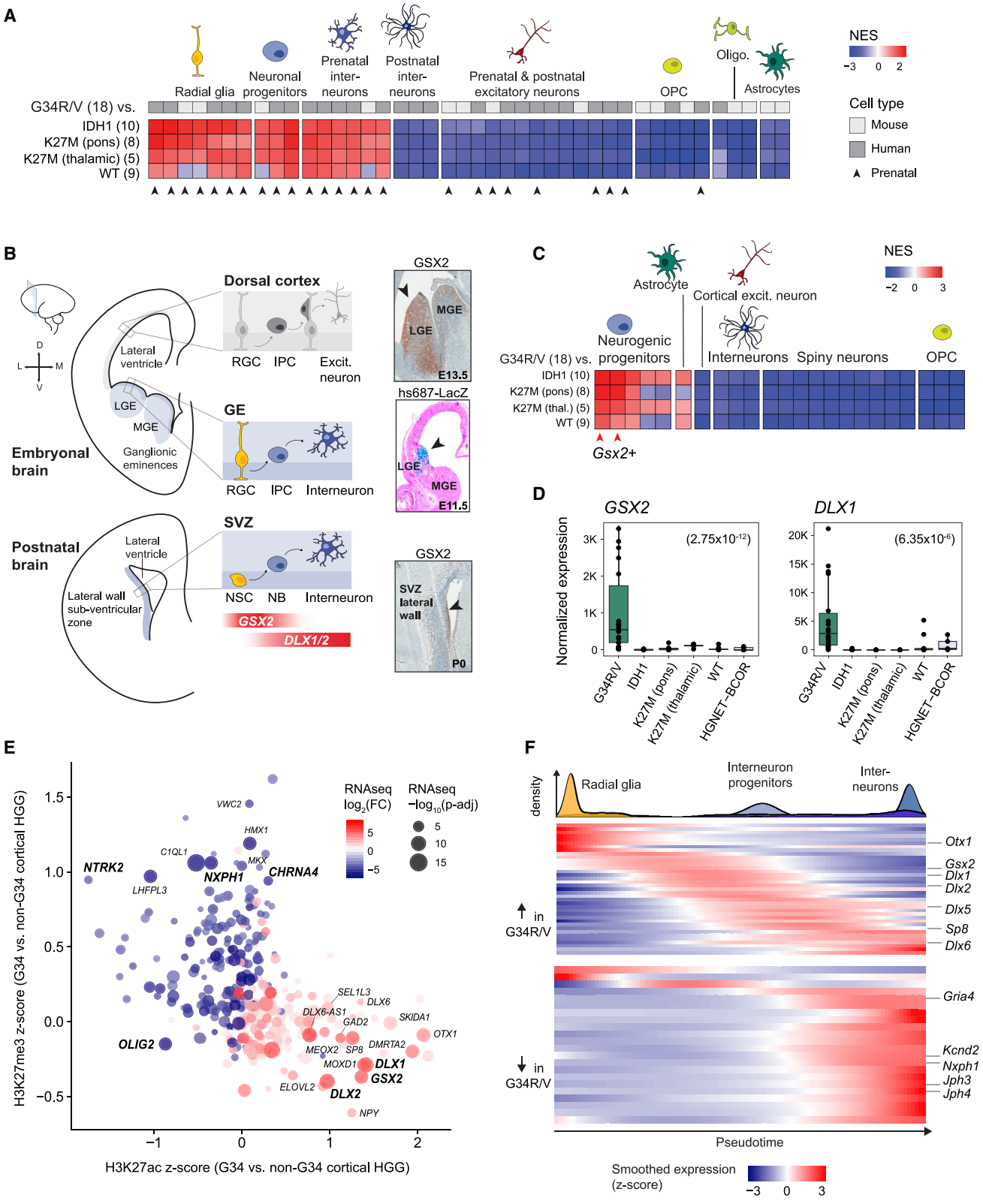

(legend on next page)

expressed in interneuron progenitors. Conversely, genes downregulated and H3K27me3 enriched in G34R/V peaked in expression late in normal interneuron maturation. The transcriptomic and epigenomic profiles of G34R/V HGGs indicate that they arise within ventrally derived progenitors committed to the interneuron lineage, which appear to be restricted from progressing to a mature neuronal state.

G34R/V Mutations Promote H3K27me3 Retention at Genic Promoters and Silencing of Mature Neuronal Genes

H3K27me3 patterns in G34R/V gliomas may reflect their developmental origin or derive from G34R/V-mediated epigenetic dysregulation. H3.3G34R/V substitutions have been shown previously to impair the catalytic deposition of histone H3 lysine 36 tri-methylation (H3K36me3) by SETD2 (Lewis et al., 2013; Zhang et al., 2017), a mark coupled to active transcription and known to directly antagonize H3K27 methylation (Schmitges et al., 2011). Using liquid chromatography-mass spectrometry (LC-MS) of histones extracted from patient-derived cell lines, we observed H3K36me3 loss coupled to reciprocal gain of H3K27me3 specifically on H3.3G34R/V mutant histone peptides (Figure S3A), confirming the *cis* effect of these mutations. At the genome-wide level, chromatin immunoprecipitation sequencing (ChIP-seq) showed H3K27me3 deposition to be significantly enriched at a large number of genic promoters (n = 3,901) in G34R/V HGGs compared with non-G34R/V cortical HGGs (Figure S3B). We observed specific H3K27me3 enrichment at promoters of several genes encoding brain-specific proteins implicated in neuronal function in G34R/V samples. This gain in H3K27me3 contrasted with the relatively balanced changes observed in H3K27ac deposition, where only ~100 promoters showed differential enrichment in G34R/V (Figure S3C).

To determine whether H3K27me3 enrichment is a direct consequence of the G34R/V oncohistone, we targeted the mutation for removal in the HSJD-GBM002 (*H3F3A*^{G34R}) cell line using CRISPR-Cas9 (Figure S3D). There were limited differences in histone marks by ChIP-seq or the transcriptome by RNA-seq between G34R and edited clones (Tables S2 and S3; Figures S3E–S3G), suggesting that the global epigenomic landscape is not actively maintained by G34R/V mutant histones in transformed cells. Expression of the *DLX* family of interneuron TFs was maintained in edited and unedited lines (Figure 3A, top row), suggesting that specification of the interneuron transcriptional program in G34R/V gliomas reflects their lineage of origin. Notably, when assessing genomic bins showing the greatest H3K36me3 loss in G34R, these concurrently displayed increased polycomb repressive complex 2 (PRC2)SUZ12/H3K27me3 enrichment and decreased transcriptional activity, in keeping with the presumed effect of G34R/V on these marks (Figure 3B; Figures S3E–S3G). When edited clones were subjected to serum differentiation, we observed upregulation of *DLX1* but, notably, also of *DLX5*, which is normally induced later in interneuron differentiation (Figure 3A, bottom row). These edited clones showed enrichment of interneuron gene programs and depletion of radial glia cell gene signatures, consistent with further progression into neuronal differentiation upon removal of the mutation (Figure 3C).

Finally, to confirm the G34R-mediated epigenomic and transcriptomic effects *in vivo*, we utilized a previously described *in utero* electroporation (IUE) murine model (Pathania et al., 2017). Embryonic day 13.5 (E13.5) neocortices were electroporated with exogenous empty vector (EV), H3.3 wild type (WT), or H3.3G34R in combination with *Pdgfra* WT, *Atrx* short hairpin RNA (shRNA), and short-guide RNA (sgRNA) for *Trp53*, along with episomal vectors for Cas9 and pBase. We profiled *ex-vivo*-expanded neural precursor cells derived from sorted GFP+TdTomato+ cells after 72 h and in mice older than 1 year (Figure S4A). Minimal changes were observed 72 h after electroporation, whereas marked accumulation of H3K27me3 at genic promoters was observed in adult G34R-expressing cells. Importantly, and consistent with H3K27me3 patterns in human G34R/V tumors and CRISPR lines, the IUE cells also exhibited G34R-specific H3K27me3 retention at genic promoters such as *Jph4* and *Foxp2*, a TF expressed in mature forebrain neurons (Figures S4B and S4C). By leveraging model systems to decouple the effect of G34 mutations from existing lineage of origin programs, we conclude that G34R/V oncohistones may directly impede terminal neuronal differentiation through aberrant H3K27me3 retention at specific neuronal maturation loci.

Figure 2. Transcriptional and Epigenetic Programs in G34R/V Gliomas Indicate an Interneuron Progenitor Origin

(A) Heatmap of enrichment scores of forebrain cell type signatures in G34R/V compared with other HGG subgroups by gene set enrichment analysis (GSEA). Normalized enrichment scores (NES) are shown for all signatures enriched significantly (adjusted $p < 0.01$) in G34R/V versus IDH1. The number of tumor samples is indicated in parentheses. OPC, oligodendrocyte progenitor cell.

(B) Left: schematic of the embryonic and postnatal forebrain, coronal section. LGE, lateral GE; MGE, medial GE; RGC, radial glia cell; IPC, intermediate neuronal progenitor cell; NSC, neural stem cell; NB, neuroblast. Right: immunohistochemistry staining of *Gsx2* in sagittal sections of E13.5 mouse GEs and post-natal day 0 (P0) (SVZ) and enhancer reporter activity of hs687-LacZ in coronal sections of E11.5 mouse embryos, profiled by the VISTA enhancer browser.

(C) Heatmap of enrichment scores of striatal sub-ventricular zone (SVZ) cell type signatures in G34R/V compared with other HGG subgroups by GSEA. NES are shown for all signatures enriched significantly (adjusted $p < 0.01$) in G34R/V versus IDH1. The number of samples is indicated in parentheses.

(D) Expression levels of the interneuron markers *GSX2* and *DLX1* in tumor subgroups. Adjusted p values (negative binomial Wald test) for comparison of G34R/V with other entities are indicated in parentheses.

(E) Promoter-associated H3K27ac and H3K27me3 for genes significantly differentially expressed between G34R/V and IDH1 HGG by bulk RNA-seq. Genes relevant to glioma (*OLIG2*) or with high G34R/V enrichment of either mark (*Z* score > 0.9) and RNA-seq absolute log2 fold change of more than 3 are labeled.

(F) Gene expression levels of G34R/V-specific genes along the interneuron differentiation trajectory (Jessa et al., 2019). Top panel: density of each cell type along pseudotime. Bottom panel: expression of genes identified as specific to G34R/V gliomas by epigenome and transcriptome analyses. Up in G34R/V, genes in the leading edge of the most enriched human interneuron signature or genes upregulated by RNA-seq and enriched for H3K27ac in G34R/V; down in G34R/V, genes in the leading edge of the most depleted human interneuron signature or genes downregulated by RNA-seq and enriched for H3K27me3 in G34R/V (STAR Methods). Expression is *Z* scored across pseudotime.

See also Figure S2 and Tables S2 and S3.

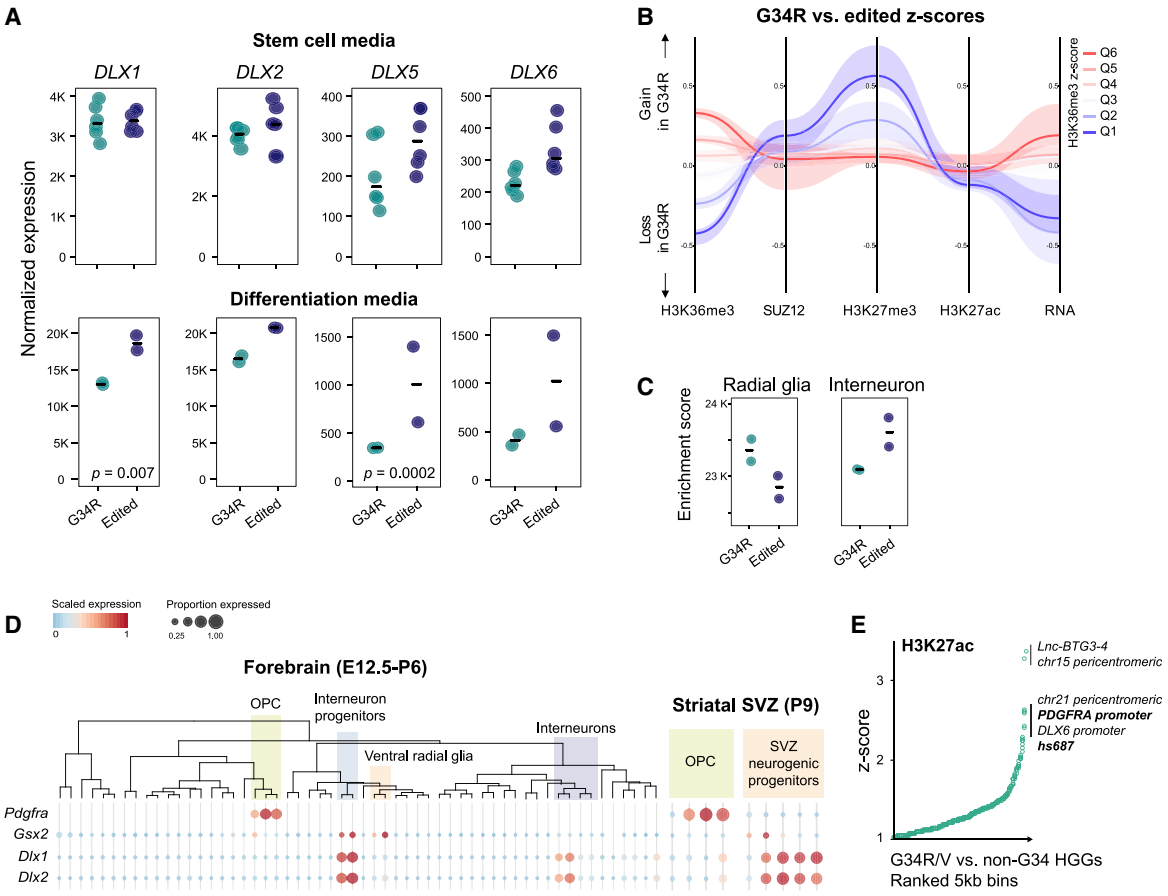

Figure 3. G34R/V HGGs Aberrantly Express PDGFRA, Unlike Normal Interneuron Progenitors

(A) Expression of selected interneuron TFs in the patient-derived cell line HSJD-GBM002 in stem cell media (top, n = 6) or differentiation media (bottom, n = 2). Green, unedited or parental clones containing G34R; blue, edited clones with the G34R mutation removed by CRISPR. The horizontal bar indicates the median. Adjusted p values (negative binomial Wald test) are indicated.

(B) Parallel coordinate plot depicting epigenomic and transcriptomic changes in HSJD-GBM002 G34R and edited clones. Genomic bins (5 kb) were stratified into 6 quantiles (Q1–Q6) based on H3K36me3 difference upon CRISPR editing, and changes for the other histone marks and transcription were computed for each quantile. Solid line, median; shaded area, 25% and 75% percentiles.

(C) Single-sample GSEA (ssGSEA) score for RGC and interneuron gene signatures in transcriptomes of HSJD-GBM002 clones in differentiation media.

(D) *Pdgfra*, *Gsx2*, and *Dlx1/2* expression in the mouse scRNA-seq developmental forebrain atlas (left) and postnatal striatal SVZ atlas (right). Mean expression and proportion of cells expressing the gene are indicated.

(E) 5-kb genomic bins ranked by H3K27ac *Z* score, showing the top-ranking loci with H3K27ac enrichment in G34R/V versus non-G34 HGGs.

See also Figures S3 and S4 and Tables S2 and S3.

Active Chromatin Conformation Facilitates PDGFRA Co-option in G34R/V Tumors

We next investigated the mechanism underlying the association of G34R/V interneuron progenitor programs with *PDGFRA*. The *PDGFRA* gene is located immediately adjacent to the interneuron TF *GSX2*. In G34R/V tumors and cell lines, *PDGFRA* expression was positively correlated with *GSX2* (R^2 = 0.48, p = 0.0002; Figure S5A), whereas in the other subtypes, correlation was lower (R^2 = 0.2), and *GSX2* was very lowly expressed (Figure S1A). This transcriptional coupling observed in G34R/V tumors is likely aberrant because *PDGFRA* and *GSX2* are normally expressed in distinct cell lineages (Figure 3D; Figure S5B), suggesting that *PDGFRA* hijacks surrounding *cis*-regulatory regions to promote its ectopic expression in G34R/V HGGs.

To determine whether epigenetic dysregulation underlies this transcriptional coupling, we first examined H3K27ac profiles in G34R/V tumors. Indeed, the top genomic bins showing differential H3K27ac deposition in G34R/V included the *PDGFRA* promoter as well as a distal enhancer element *hs687*, located near *GSX2*/*PDGFRA* (Visel et al., 2013; Figure 3E). This VISTA-validated enhancer has been shown to drive reporter expression in the lateral GE of the embryonal telencephalon, coincident with *Gsx2* expression, and it is thus likely involved in its regulation (Figure 2B). We next examined *PDGFRA*-adjacent *cis*-regulatory elements and observed specific activation in the form of discrete H3K27ac peaks throughout a 350-kb region on chromosome 4 (chr4), encompassing *PDGFRA*, *GSX2*, and *hs687*, that is unique to G34R/V HGGs (Figure 4A, bottom tracks; Figure S5C).

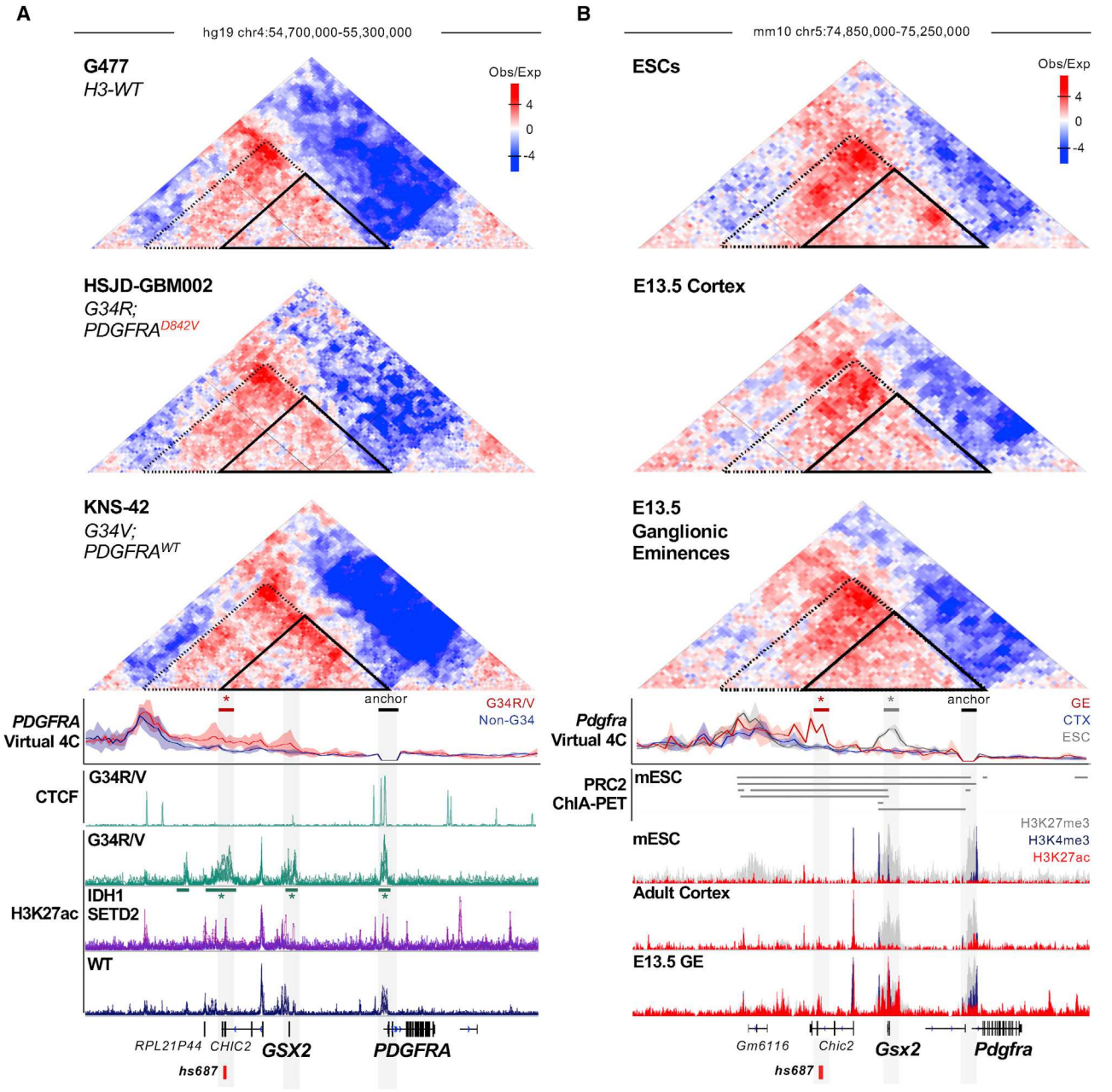

(legend on next page)

To determine whether these H3K27ac peaks correspond to distal regulatory elements used to promote ectopic *PDGFRA* expression, we performed Hi-C chromosome conformation capture and *CCCTC-binding factor* (CTCF) ChIP-seq on G34R/V, K27M, and WT primary cell lines (Figure 4A; Figure S5D; Table S4). We confirmed the presence of a topologically associated domain (TAD) encompassing the *PDGFRA* promoter (Figure 4A, dashed triangle), known to be present in non-cancerous somatic cells (Flavahan et al., 2016). In addition to this non-specific TAD, we uncovered a novel interaction loop in G34R/V cell lines (Figure 4A, solid triangle), linking the *PDGFRA* promoter with *hs687*, the putative *GSX2* enhancer element. In fact, throughout the region spanning *PDGFRA*, *GSX2*, and *hs687*, the TAD in G34R/V glioma cell lines harbored significantly more interactions in G34R/V compared with the H3 WT and K27M lines ($p = 0.04$, one-tailed t test), supporting a conformation with increased potential for ectopic activation of *PDGFRA* in G34R/V HGGs through active enhancer/promoter contacts.

PDGFRA expression in $PDGFRA^{MUT}$ G34R/V HGGs is higher than in $PDGFRA^{WT}$ tumors (Figure S1A), suggesting that additional *cis*-regulatory elements may augment expression of this RTK. We observed that $PDGFRA^{MUT}$ tumors further increased H3K27ac activation of regulatory elements within the neighboring region, including at the *GSX2* promoter and *hs687*, as well as new distal regulatory elements (e.g., chr4, ~53,100,000) (Figure S5E). Consistent with the H3K27ac profile, Hi-C interaction matrices showed more *PDGFRA*-anchored distal interactions in the $PDGFRA^{MUT}$ cell line (Figure S5F, black boxes). This suggests that further activation of the existing chromatin conformation, particularly at key *hs687* and *GSX2* regulatory elements, is used to promote higher *PDGFRA* expression in samples carrying a mutation of this RTK.

The chromatin conformation of G34R/V tumors, bringing the *PDGFRA* promoter in close proximity to active *GSX2* regulatory elements, may be transiently present during normal differentiation of the interneuron lineage. We thus investigated the dynamics of this region during murine development, comparing the epigenomic landscape and chromosome conformation of embryonic stem cells (ESCs) and E13.5 forebrain tissue (Davis et al., 2018; Lindtner et al., 2019). In ESCs, a strong promoter-promoter interaction is present between *Pdgfra* and *Gsx2*, where both genic promoters are bivalently marked with active histone H3 lysine 4 tri-methylation (H3K4me3) and repressive H3K27me3 marks (Figure 4B, bottom tracks). Chromatin interaction analysis by paired-end tag sequencing (ChIA-PET) confirms that this loop between *Pdgfra* and *Gsx2* promoters is anchored by PRC2-mediated contacts, indicating that this interaction is present while both genes are repressed (Ngan et al., 2020). Moreover, no interactions were observed in ESCs between *Pdgfra* and *hs687*. At E13.5, in turn, a loop between *hs687* and *Gsx2* was detected in GEs ($p = 0.03$), confirming the function of this enhancer element as a driver of *Gsx2* expression in the lineage (Figure S5G). More importantly, we observed that a second strong loop between *Pdgfra* and *hs687* is formed uniquely in these GEs. In addition, we identify a TAD anchored at the *Pdgfra* promoter and *hs687,* analogous to the one found in G34R/V tumors, that is significantly enriched in GEs compared with the dorsal cortex ($p = 0.04$) and ESCs ($p = 0.02$). This increase in contact frequency is concurrent with increased H3K27ac at the *hs687* enhancer and *Gsx2*, confirming their active conformation in this developmental window. *Pdgfra* remains transcriptionally repressed in the GEs, retaining bivalent H3K27me3 and H3K4me3 marks, consistent with aberrant oncogenic expression of this RTK in G34R/V gliomas.

The epigenomic profiles of ESCs suggest that the promoters of *Gsx2* and *Pdgfra* are physically anchored by the PRC2 complex and poised for activation (Figure 4C). In the neocortex, where progenitors give rise to excitatory neurons, the *Gsx2-Pdgfra* contact is weakened, and the *Gsx2* promoter no longer possesses the potential to become activated, similar to what is observed in non-G34 HGGs. In contrast, in the GEs, where interneurons are born, *Gsx2* contacts its distal enhancer *hs687* for activation and remains bound to H3K27me3-repressed *Pdgfra*, bringing *Pdgfra* in close proximity to this active chromatin conformation. The transcriptomic and epigenomic evidence suggests that the chromatin architecture of G34R/V HGGs resembles that of a *GSX2+* progenitor, with *PDGFRA* expression reflecting an oncogenic event. These results provide a mechanistic link for the interneuron progenitor-context dependency of *PDGFRA* mutations in G34R/V HGGs, where *GSX2*-associated *cis*-regulatory elements are recruited to induce aberrant *PDGFRA* expression in G34R/V tumors and, possibly, to a greater extent in *PDGFRA* mutants.

Figure 4. Active Chromatin Conformation Facilitates *PDGFRA-GSX2* Co-option in G34R/V Tumors

(A) Top: Hi-C heatmaps depicting sub-TAD structure at the *PDGFRA-GSX2-hs687* locus in glioma cell lines. A small black triangle illustrates a TAD between *PDGFRA* and the hs687 enhancer enriched for contacts in G34R/V lines. A large dashed triangle demarcates the TAD formed by contact to a known distal insulator. The heatmap represents the log2 ratios of observed interactions relative to expected interactions at a 5-kb resolution. Center: virtual 4C plots representing the average intensity of *PDGFRA*-anchored contacts in G34R/V and non-G34 glioma cell lines. A black bar denotes the virtual 4C anchor region. A red bar and asterisk denote regions with significantly increased contact in G34R/V relative to non-G34 lines ($p < 0.05$). Bottom: composite CTCF and H3K27ac ChIP-seq of primary cortical glioma G34R/V, IDH1/SETD2, and WT subgroups. A teal bar and asterisk denote significantly H3K27ac-enriched regions in G34R/V (Z score > 0.5, $p < 0.05$).

(B) Top: Hi-C heatmaps from murine embryonic stem cells (ESCs), E13.5 cortex, and GEs depicting sub-TAD structure at the *Pdgfra-Gsx2-hs687* locus as in (A). Center: virtual 4C plots representing the average intensity of *Pdgfra*-anchored contacts in ESCs, E13.5 cortex, and GEs. A black bar denotes the virtual 4C anchor region. A red bar and asterisk denote regions with significantly increased contact in GE relative to cortex (p value < 0.05). A gray bar and asterisk denote a region with significantly increased contact in ESCs relative to cortex ($p < 0.05$). Bottom: PRC2 ChIA-PET in ESCs illustrating PRC2-bound chromatin contacts. Below, H3K27me3, H3K27ac, and H3K4me3 ChIP-seq for ESCs, murine adult cortex, and E13.5 GE.

(C) Schematic illustrating chromosome conformation and chromatin landscape at the *Pdgfra-hs687* locus. The active hs687 enhancer (yellow) is in close contact with poised *Pdgfra* selectively in the GEs.

See also Figure S5 and Table S4.

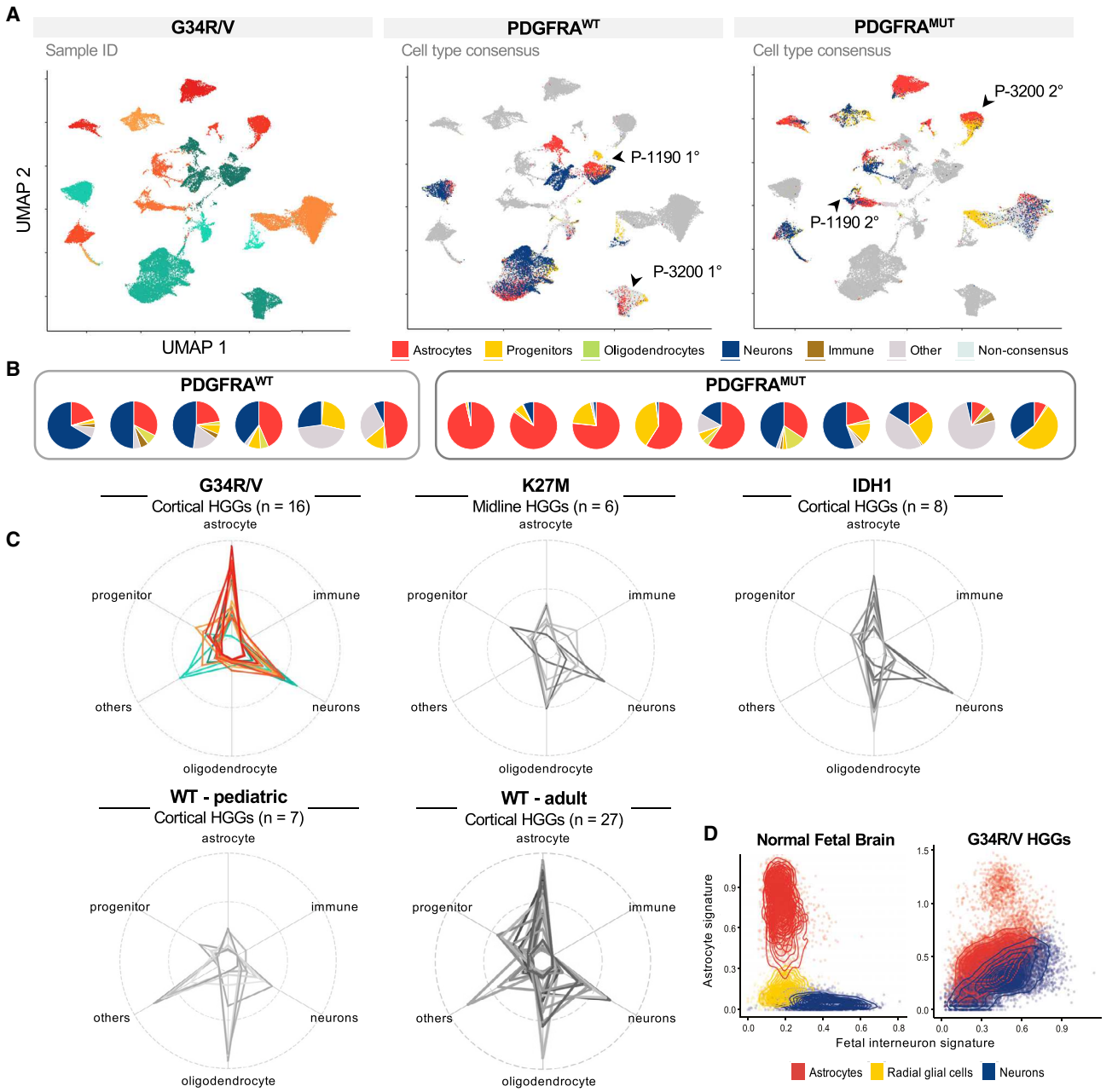

Figure 5. G34R/V Tumors Are Devoid of Oligodendrocytes, and *PDGFRA*-Mutant Tumors Exhibit Expanded Astrocytic Compartments

(A) Uniform manifold approximation and projection (UMAP) embedding of scRNA-seq G34R/V malignant cells from patient samples colored by patient of origin (left) or consensus cell type projection (center and right). The two primary/recurrence tumor pairs are highlighted.

(B) Pie charts depicting the proportion of each cell type in individual tumors.

(C) Radar plots depicting the proportion of cells projected to a certain cell type within each tumor entity. Each line represents one sample, color-coded as in (A) for G34R/V tumors. Outer circle, 100%; center circle, 50%; inner circle, 0%.

(D) Mean expression of fetal interneuron and astrocyte gene signatures in individual cells from the mouse scRNA-seq developmental forebrain atlas (left) and in cells from G34R/V tumors (right). For tumors, only cells called malignant and projected as neurons or astrocytes were included.

See also Figure S6 and Table S5.

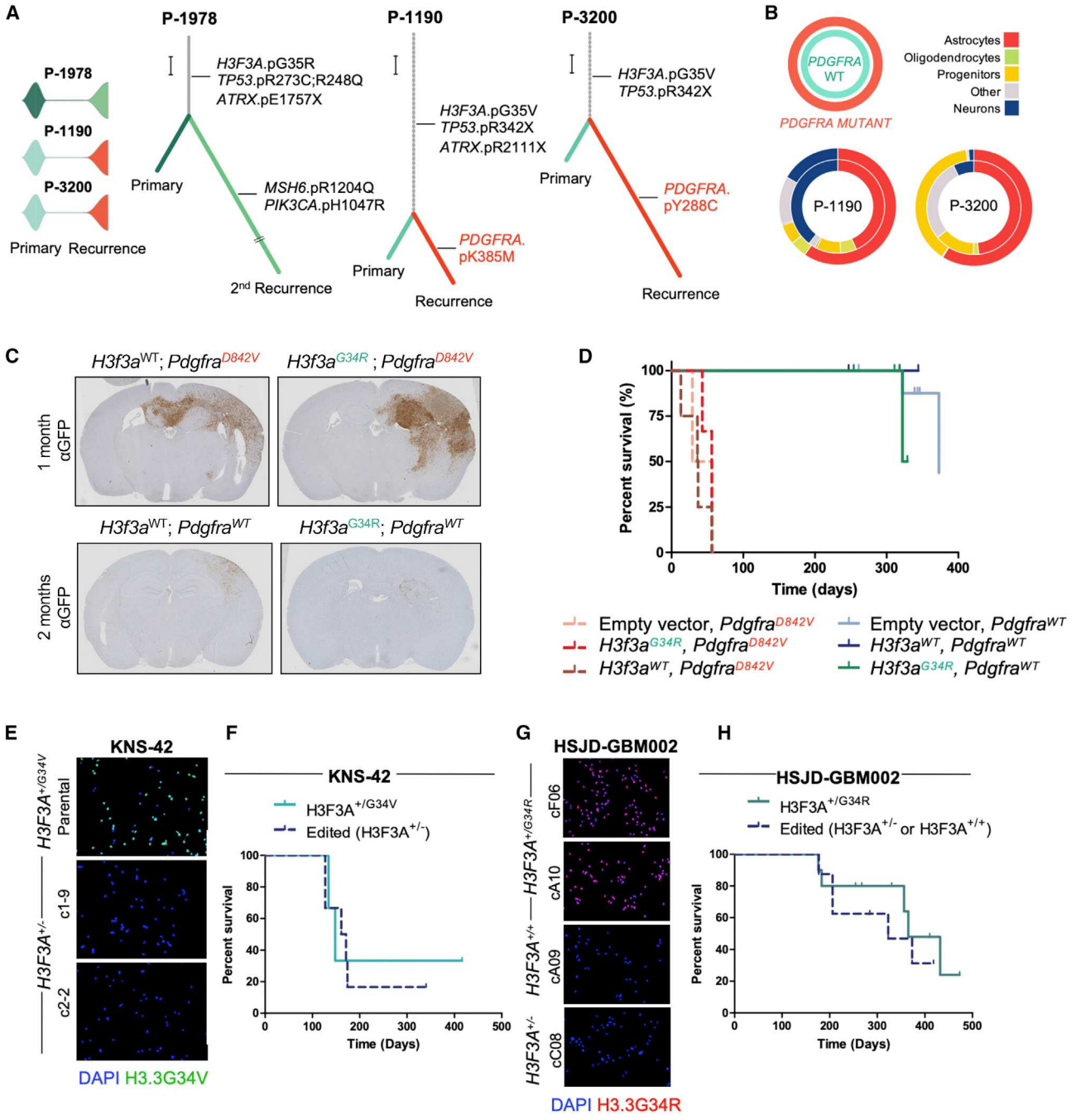

Figure 6. Mutant *Pdgfra* Is a Strong Oncogenic Driver, and G34R/V May Be Dispensable for Tumor Maintenance

(A) Left: fish plots depicting tumor clonal structure of G34R/V primary and matched recurrence samples from individuals P-1978, P-1190, and P-3200. Right: phylogeny of G34R/V primary and matched recurrence samples from individuals P-1978, P-1190, and P-3200. Scale bar, 10 mutations. Dashed lines, potential germline mutations.

(B) Doughnut plots representing the proportion of cells projected to each cell type in two primary/recurrence pairs, highlighting the increased proportion of astrocyte-like cells in the *PDGFRA*^{MUT} recurrence (outer circle) compared with the *PDGFRA*^{WT} primary tumor (inner circle).

(C) Immunohistochemical GFP staining of coronal forebrain sections from IUE mice. All mice received *shAtrx* and *sgTrp53* in addition to *Pdgfra*^{WT} or *Pdgra*^{D842V} and H3.3 WT/G34R.

(D) Kaplan-Meier curve depicting survival of IUE mice. All mice received *shAtrx* and *sgTrp53* in addition to *Pdgfra*^{WT} or *Pdgra*^{D842V} and EV/H3.3 WT/G34R.

(E) Immunofluorescence validation of CRISPR-mediated removal of G34V in KNS-42 clones.

(F) Kaplan-Meier survival curves of KNS-42 clones. A teal line depicts the parental line carrying G34V, and a dashed blue line depicts edited clones.

(legend continued on next page)

G34R/V HGGs Are Neuronal Tumors Devoid of Oligodendroglial Cells Where PDGFRA Mutations Expand Aberrant Astrocytic Compartments

To evaluate the effect of *PDGFRA* mutations on cellular heterogeneity of G34R/V HGGs, we profiled 6 $PDGFRA^{WT}$ and 10 $PDGFRA^{MUT}$ tumors by scRNA-seq (Figures 5A and 5B; Figure S6A; Table S5). Projection of malignant cells to a reference developmental brain atlas (Jessa et al., 2019) revealed that G34R/V tumors were predominantly comprised of neuron- and astrocyte-like cells, consistent with the reported heterogeneous histopathology. We observed a striking absence of oligodendroglial-like cells in all G34R/V tumors, in contrast to other pediatric and adult HGGs entities, where they were readily detectable (Filbin et al., 2018; Neftel et al., 2019; Venteicher et al., 2017), and limited numbers of immune cells, similar to K27M gliomas (Filbin et al., 2018; Figure 5C; Figure S6B). At the level of individual cells, G34R/V astrocytic and neuronal cells were highly dysplastic, with most cells displaying abnormal co-expression of interneuron and astrocytic gene signatures and indefinite segregation between compartments (Figure 5D; Figure S6C). Across individuals, G34R/V HGGs exhibited significant inter-tumor heterogeneity, with varying proportions of neuronal and astrocytic-like cells (Figure 5B; Figure S6A). Importantly, G34R/V tumors mutant for *PDGFRA* displayed an expansion of the astrocytic compartment compared with WT tumors ($p = 0.028$, Wilcoxon rank-sum test), suggesting that acquisition of a *PDGFRA* mutation promotes an astrocytic state at the expense of the neuronal component.

We next examined the role of *PDGFRA* mutations in G34R/V tumor evolution from three available matched primary and recurrent tumor pairs (Figure 6A; Table S6). Phylogenetic trees inferred from allele frequencies revealed a remarkably high mutation burden (n = 4,218) consistent with a temozolomide treatment signature in P-1978 recurrence (G34R; $PDGFRA^{WT}$). In contrast, relatively few new mutations appeared in recurrences of individuals P-1190 and P-3200 (43 and 124 mutations, respectively), with *PDGFRA* the only gene commonly mutated in recurrences of both individuals. Moreover, there was little evidence of clonal heterogeneity (Figure 6A), suggesting strong sweeping selection for the new *PDGFRA* mutations acquired. At the transcriptomic level, scRNA-seq data from both individuals showed an expansion of the astrocytic compartment, with a concomitant decrease of the neuron-like compartment (Figure 6B). Moreover, the MAPK/ERK pathway was significantly more active in tumors mutant for *PDGFRA* (Figure 1C). Together, these findings suggest that the acquisition of *PDGFRA* mutations in G34R/V activates downstream MAPK signaling and leads to clonal selection, astrocytic expansion, and potentially oncogenic addiction upon recurrence.

G34R/V Mutations May Be Dispensable for Tumor Maintenance, and Mutant PDGFRA Is a Potent Oncogenic Driver

To delineate individual effects of *PDGFRA* and G34R/V mutations on gliomagenesis, we compared latency with tumor formation in the murine IUE and CRISPR cell line models (Pathania et al., 2017). Consistent with known oncogenic properties of $PDGFRA^{D842V}$, immunohistochemical GFP staining showed extensive tumor growth in $Pdgfra^{D842V}$-electroporated mice in as little as 1 month (Figure 6C). Addition of the G34R mutation did not affect latency in this model because $H3f3a^{WT}$ and $H3f3a^{G34R}$ IUE mice showed similar tumor growth and survival (Figure 6D). In contrast, GFP staining at 2 months upon electroporation of $Pdgfra^{WT}$ was largely negative. This finding is further reinforced in the time to tumor formation; 12 months post-IUE, $H3f3a^{G34R};Pdgfra^{WT}$ formed tumors with two-thirds penetrance compared with $EV;Pdgfra^{WT}$ with similar latency and one-third penetrance. In contrast, $Pdgfra^{D842V}$ was strongly oncogenic and fully penetrant regardless of G34R presence, decreasing tumor latency for the entire cohort to 50 days.

Consistent with the IUE results, CRISPR editing of H3.3G34V and G34R mutations in the respective patient-derived cell lines KNS-42 and HSJD-GBM002 showed a limited effect on tumorigenicity in orthotopic xenograft models (Figures 6E–6H). Edited lines exhibited comparable latency to tumor formation as G34 mutant lines (median survival G34V/edited, 148/166 days; G34R/edited, 365/323 days) and developed tumors with similar histopathology (Figures S7A and S7B). These findings suggest that G34R/V mutations may become dispensable for oncogenic maintenance and, instead, probably co-opt *PDGFRA* mutations to promote gliomagenesis.

DISCUSSION

We comprehensively profiled the molecular landscape of H3.3G34R/V HGGs in the largest multi-institutional cohort to date, which features several rare cases of matched primary and recurrence tumors. We show an enrichment of activating *PDGFRA* mutations (44%), concurrent with elevated expression, in G34R/V primary tumors relative to all other HGG subtypes. This frequency is higher in the recurrence setting (81%) because tumors initially WT acquired *PDGFRA* mutations with strong selective pressure for the mutant clone at recurrence. PDGFRA is an important RTK in glial development and a recurrent driver in HGGs (Mackay et al., 2017; Sturm et al., 2012; Verhaak et al., 2010), which show distinct mechanisms for its co-option in the different subgroups. Indeed, *PDGFRA* amplifications are commonly observed in K27M mutant midline gliomas (40%) (Khuong-Quang et al., 2012; Mackay et al., 2017; Sturm et al., 2012) and IDH WT pro-neural HGGs (Mackay et al., 2017; Sturm et al., 2012). Conversely, IDH1 mutant HGGs use a distal enhancer through DNA methylation of a proximal CTCF insulator to overexpress *PDGFRA* (Flavahan et al., 2016), whereas activating mutations are more frequently observed in non-brainstem gliomas occurring in older children (14%) (Koschmann et al., 2016; Paugh et al., 2013).

The high frequency of *PDGFRA* mutations unique to G34R/V gliomas is likely due to their distinct differentiation program.

(G) Immunofluorescence validation of CRISPR-mediated repair/removal of G34R in HSJD-GBM002 clones.
(H) Kaplan-Meier survival curves of HSJD-GBM002 clones. A teal line depicts the parental and unedited clones carrying G34R, and a dashed blue line depicts edited clones.
See also Figure S7 and Table S6.

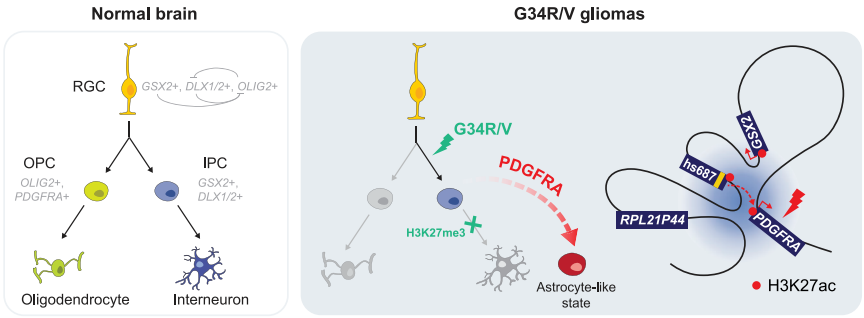

Figure 7. Model of Aberrant Development in G34R/V Gliomas Compared with Normal Development in the Ventral Forebrain

Left: During normal development, radial glial cells (RGCs) in the ventral forebrain give rise to oligodendrocyte precursor cells (OPCs), which differentiate into oligodendrocytes, and (IPCs), which differentiate into cortical interneurons. Right: G34R/V gliomas retain molecular features of a committed interneuron progenitor (*GSX2*, *DLX1/2+*), and oncohistone-mediated H3K27me3 gain may impede terminal neuronal differentiation. G34R/V tumors exhibit dual neuronal and astrocytic components. Elevated expression and oncogenic *PDGFRA* mutation may promote the abnormal astrocyte-like state. G34R/V HGGs display a topologically associated domain (TAD), which brings the *GSX2* associated *cis*-regulatory elements (*hs687*) into proximity of the *PDGFRA* promoter to induce overexpression.

Our data suggest that G34R/V tumors originate in *GSX2+* interneuron progenitors (Figure 7), where the oncohistone impedes terminal neuronal differentiation through altered H3K36me3 deposition and aberrant H3K27me3 retention at specific genes, a pattern suggested by prior biochemical analyses performed on G34R/V mutant nucleosomes (Lewis et al., 2013). This progenitor state likely maintains the lineage-specific *GSX2* enhancer in an active chromatin conformation state, rendering the locus permissive to transcriptional exploitation and aberrant *PDGFRA* expression (Figure 7). The spatial contact between *GSX2* and *PDGFRA* seems to be an early event, present in ESCs, where expression of both genes is repressed by PRC2/H3K27me3. As cells undergo neuronal differentiation, it is uniquely preserved in *Gsx2+* interneuron progenitors in E13.5 GEs, whereas it is lost in other neuronal populations, as our data indicate. In GEs, *Pdgfra* remains in a poised state in close physical proximity with *Gsx2*-associated enhancer machinery (including *hs687*), presenting an opportunity for oncogenic co-option, because the epigenetic landscape favors activation of this lineage factor. We speculate that *PDGFRA*-mutant tumors may form additional contacts with distal regulatory elements to maintain high *PDGFRA* expression, fueling their oncogenic addiction and dependence on PDGFRA, given the selective advantage of this mutant RTK. Whether the G34R/V mutation occurs during this embryonic window of development or in postnatal *GSX2+* interneuron progenitors in the SVZ remains to be determined.

Ectopic *PDGFRA* expression and subsequent acquisition of activating mutations likely promote astroglial features in G34R/V-stalled interneuron progenitors. Notably, a *Nestin*- inducible K27M/*Trp53*^{cKO} mouse model aiming to model K27M midline gliomas led to neuronal high-grade tumors that became HGGs only upon co-expression of *PDGFRA*^{V544ins} (Larson et al., 2019), in keeping with a major role of *PDGFRA* mutations in driving gliogenesis. Specific induction of downstream MAPK signaling is probably necessary for expansion of astrocytic lineage programs in G34R/V tumors because increasing ERK activation has been shown to promote glial specification at the expense of neuronal lineages (Li et al., 2014). Finally, persistent high levels of *GSX2* and *DLX1/2* are likely responsible for the absence of oligodendroglial lineage programs in G34R/V HGGs because downregulation of these TFs is required for transition from neurogenesis to oligodendrocyte formation in the ventral forebrain (Chapman et al., 2013, 2018; Petryniak et al., 2007).

Our data suggest that *PDGFRA* mutants are robust glioma drivers in G34R/V HGGs and that, in contrast to K27M (Harutyunyan et al., 2019; Krug et al., 2019), G34R/V mutations may be dispensable for tumor maintenance. We show that ~80% of *PDGFRA* mutations occurred in the extracellular domain, with the glioma-specific C235Y/F mutations alone accounting for 30% of all *PDGFRA* mutations in G34R/V. These neomorphic mutations constitutively activate this RTK, as also suggested by downstream activation of the MAPK pathway observed in *PDGFRA*^{MUT} G34R/V HGGs. These mutants may have additional biochemical properties that warrant specific investigation, as alluded to by one study indicating that they may be resistant to standard PDGFRA inhibitors (Ip et al., 2018). Initially targeting the downstream MAPK pathway may be of benefit in this context, but further investigations are needed to identify therapeutic vulnerabilities in tumors with extracellular-domain *PDGFRA* mutations.

In sum, we highlight a novel mechanism where *PDGFRA* expression is ectopically promoted by the interneuron TF *GSX2*, potentially leading to the high rate of activating mutations of this RTK specifically in G34R/V HGGs. Cells that acquire a *PDGFRA* mutation undergo sweeping clonal selection and potently activate MAPK signaling to promote gliomagenesis. These mechanisms have important therapeutic implications because G34R/V HGGs are classified as gliomas based on morphology, whereas they seem neuronal in origin based on genetic and molecular markers. These tumors are invariably lethal, and *PDGFRA* mutations and downstream MAPK activation are potentially actionable targets, providing hope for novel therapeutic opportunities in this deadly cancer.

STAR★METHODS

Detailed methods are provided in the online version of this paper and include the following:

- KEY RESOURCES TABLE
- RESOURCE AVAILABILITY
  - Lead Contact
  - Materials Availability
  - Data and Code Availability
- EXPERIMENTAL MODEL AND SUBJECT DETAILS
  - Patient samples and clinical information

- Primary cell lines
- Animal models

- METHOD DETAILS
  - Immunohistochemistry for patient tumors
  - CRISPR/Cas9 gene editing
  - Immunofluorescence
  - Histone post-translational modification by nLC/MS
  - Mouse orthotopic xenograft
  - Ganglionic eminences and cortices isolation
  - IHC for PDOX and mouse brain tissue
  - Mouse in utero electroporation (IUE)
  - Model Figures
- QUANTIFICATION AND STATISTICAL ANALYSIS
  - Structural molecular modeling
  - Whole exome- and RNA-sequencing
  - Variant calling
  - Reconstruction of tumor phylogeny
  - Gene expression quantification from RNA-seq data
  - Assessment of developmental programs in tumors
  - Gene expression profiling in normal development
  - Gene expression along interneuron differentiation
  - Chromatin immunoprecipitation sequencing
  - Hi-C chromatin conformation capture
  - Single-cell and single-nuclei RNaseq

SUPPLEMENTAL INFORMATION

Supplemental Information can be found online at https://doi.org/10.1016/j.cell.2020.11.012.

ACKNOWLEDGMENTS

We thank the patients and their families for their invaluable contributions to this research, without whom it would be impossible. This work was supported by funding from a large-scale applied research project grant from Genome Quebec, Genome Canada, the Government of Canada, and the Ministère de l'Économie, de la Science et de l'Innovation du Québec with support from the Ontario Institute for Cancer Research through funding provided by the Government of Ontario (to N. Jabado., M.D.T., and C.L.K.); Fondation Charles-Bruneau (to N. Jabado); National Institutes of Health (NIH) grants P01-CA196539 (to N. Jabado) and R01CA148699 and R01CA159859 (to M.D.T.); Canadian Institutes of Health Research (CIHR) grants MOP-286756 and FDN-154307 (to N. Jabado) and PJT-156086 (to C.L.K.); Canadian Cancer Society (CCSRI) grant 705182 and a Fonds de Recherche du Québec – Santé (FRQS) salary award (to C.L.K.); the Fonds de recherche du Québec - Santé, Génome Québec, and the Cancer Research Society (to C.L.K.); NSERC RGPIN-2016-04911 (to C.L.K.); CFI Leaders Opportunity Fund 33902 (to C.L.K.); and Genome Canada Science Technology Innovation Centre, Compute Canada Resource Allocation Project WST-164-AB. Data analyses were enabled by computing and storage resources provided by Compute Canada and Calcul Québec. N.J. is a member of the Penny Cole Laboratory and holds a Canada Research Chair Tier 1 in Paediatric Oncology from CIHR. This study was partly funded by ERC Consolidator Award H3.3Cancer (to P.S.). This work was performed within the context of the International Childhood Astrocytoma Integrated Genomic and Epigenomic (ICHANGE) consortium and Stand Up To Cancer (SU2C) Canada Cancer Stem Cell Dream Team research funding (SU2C-AACR-DT-19-15 to M.D.T. and N. Jabado) with funding from Genome Canada and Genome Quebec. M.D.T. is supported by the Pediatric Brain Tumor Foundation, the Terry Fox Research Institute, the Canadian Institutes of Health Research, the Cure Search Foundation, b.r.a.i.n.child, Meagan's Walk, Genome Canada, Genome BC, Genome Quebec, the Ontario Research Fund, Worldwide Cancer Research, the V-Foundation for Cancer Research, a Canadian Cancer Society Research Institute impact grant, and the Garron Family Chair in Childhood Cancer Research at the Hospital for Sick Children and the University of Toronto. The Children's Cancer Centre Tissue Bank at RCH Melbourne runs thanks to the generous support of Cancer in Kids @ RCH, the Leukaemia Auxiliary at RCH, the Murdoch Children's Research Institute, and the RCH Foundation. C.C.L.C. is supported by a fellowship from RI-MUHC sponsored by Toronto Dominion Bank and Alex's Lemonade Stand Foundation. S.J. is supported by fellowships from CIHR and FRQS. N.D.J. is a recipient of a fellowship from FRQS and RMGA. T.G. is a recipient of the Henry R. Shibata Fellowship. P.S. is supported by DZNE, the Wilhelm Sander Foundation, and Helmholtz Aging and Metabolic Programming (AMPro). J.V. was supported by the ÚNKP-20-4-II grant of the Ministry for Innovation and Technology, Hungary. S.C.M. is supported by a Cancer Prevention Research Institute of Texas (CPRIT) Scholar in Cancer Research award (RR170023), and an Alex's Lemonade Stand Foundation (ALSF) A award. M. Zapotocky was supported by the PRIMUS/19/MED/06 Grant Agency of Charles University in Prague. A. Klekner was supported by the 2017-1.2.1-NKP-2017-00002 National Brain Research Program NAP 2.0. We also acknowledge support from the We Love You Connie Foundation (to P.B. and N.J.), the Pediatric Brain Tumor Foundation (to P.B.), NIH 4R00CA201592-03 (to P.B.), the German Childhood Cancer Foundation (Molecular Neuropathology 2.0), the German Cancer Consortium, the German Federal Ministry of Education and Research, and the Scheu family (INFORM).

AUTHOR CONTRIBUTIONS

Conceptualization, C.C.L.C., S.D., S.J., D.H., C.L.K., and N. Jabado; Methodology, S.D., V.L., A.F.A., M.P., D.A., and A.B.; Software, S.J., V.L., S.H., N.D.J., and M.C.; Formal Analysis: C.C.L.C., S.J., D.H., V.L., R.D., H.S., F.D., E.W., S.H., M.C., N.D.J., T.G., D.M.M., A.V.B., and C.L.K.; Investigation, C.C.L.C., S.D., S.J., D.H., A.F.A., D.F., W.J., M.P., J.K., S.A., S.B., A.B., A.S.H., D.M.M., M.Z., C.R., N.M., J.V., L.B., A.V., L.K., K.V., J.Z., B.E., J.R.H., D.-A.K.-Q., A.G.W., and S.C.M.; Resources, A. Klekner, M. Zapotocky, D. Sumerauer, P.G.E., D.S.Z., M.G.F., M.B., A.M.B., B.A.G., R.B., K.L.L., M.D.T., P.B., C.K., S.M.P., A. Korshunov, D. Sturm, D.T.W.J., P.S., C.L.K., and N. Jabado; Writing, C.C.L.C., S.D., S.J., D.H., C.L.K., and N. Jabado; Project Administration/Funding Acquisition, L.G.M. and N. Juretic; Supervision, C.L.K. and N. Jabado.

DECLARATION OF INTERESTS

P.B. and R.B. receive grant funding from the Novartis Institute of Biomedical Research for an unrelated project. J.R.H. has received compensation for consultation from Bayer for unrelated work.

Received: July 29, 2020
Revised: October 1, 2020
Accepted: November 6, 2020
Published: November 30, 2020

REFERENCES

Anderson, A.G., Kulkarni, A., Harper, M., and Konopka, G. (2020). Single-Cell Analysis of Foxp1-Driven Mechanisms Essential for Striatal Development. Cell Rep. *30*, 3051–3066.e7.

Barbie, D.A., Tamayo, P., Boehm, J.S., Kim, S.Y., Moody, S.E., Dunn, I.F., Schinzel, A.C., Sandy, P., Meylan, E., Scholl, C., et al. (2009). Systematic RNA interference reveals that oncogenic KRAS-driven cancers require TBK1. Nature *462*, 108–112.

Bolger, A.M., Lohse, M., and Usadel, B. (2014). Trimmomatic: a flexible trimmer for Illumina sequence data. Bioinformatics *30*, 2114–2120.

Bonev, B., Mendelson Cohen, N., Szabo, Q., Fritsch, L., Papadopoulos, G.L., Lubling, Y., Xu, X., Lv, X., Hugnot, J.-P., Tanay, A., and Cavalli, G. (2017). Multiscale 3D Genome Rewiring during Mouse Neural Development. Cell *171*, 557–572.e24.

Bourgey, M., Dali, R., Eveleigh, R., Chen, K.C., Letourneau, L., Fillon, J., Michaud, M., Caron, M., Sandoval, J., Lefebvre, F., et al. (2019). GenPipes: an

open-source framework for distributed and scalable genomic analyses. Gigascience *8*, giz037.

Butler, A., Hoffman, P., Smibert, P., Papalexi, E., and Satija, R. (2018). Integrating single-cell transcriptomic data across different conditions, technologies, and species. Nat. Biotechnol. *36*, 411–420.

Cameron, C.J., Dostie, J., and Blanchette, M. (2020). HIFI: estimating DNA-DNA interaction frequency from Hi-C data at restriction-fragment resolution. Genome Biol. *21*, 11.

Chapman, H., Waclaw, R.R., Pei, Z., Nakafuku, M., and Campbell, K. (2013). The homeobox gene Gsx2 controls the timing of oligodendroglial fate specification in mouse lateral ganglionic eminence progenitors. Development *140*, 2289–2298.

Chapman, H., Riesenberg, A., Ehrman, L.A., Kohli, V., Nardini, D., Nakafuku, M., Campbell, K., and Waclaw, R.R. (2018). Gsx transcription factors control neuronal versus glial specification in ventricular zone progenitors of the mouse lateral ganglionic eminence. Dev. Biol. *442*, 115–126.

Chen, F., and LoTurco, J. (2012). A method for stable transgenesis of radial glia lineage in rat neocortex by piggyBac mediated transposition. J. Neurosci. Methods *207*, 172–180.

Christoforides, A., Carpten, J.D., Weiss, G.J., Demeure, M.J., Von Hoff, D.D., and Craig, D.W. (2013). Identification of somatic mutations in cancer through Bayesian-based analysis of sequenced genome pairs. BMC Genomics *14*, 302.

Cibulskis, K., Lawrence, M.S., Carter, S.L., Sivachenko, A., Jaffe, D., Sougnez, C., Gabriel, S., Meyerson, M., Lander, E.S., and Getz, G. (2013). Sensitive detection of somatic point mutations in impure and heterogeneous cancer samples. Nat. Biotechnol. *31*, 213–219.

Dali, R., Bourque, G., and Blanchette, M. (2018). RobusTAD: A Tool for Robust Annotation of Topologically Associating Domain Boundaries. bioRxiv. https://doi.org/10.1101/293175.

Davis, C.A., Hitz, B.C., Sloan, C.A., Chan, E.T., Davidson, J.M., Gabdank, I., Hilton, J.A., Jain, K., Baymuradov, U.K., Narayanan, A.K., et al. (2018). The Encyclopedia of DNA elements (ENCODE): data portal update. Nucleic Acids Res. *46* (D1), D794–D801.

DePristo, M.A., Banks, E., Poplin, R., Garimella, K.V., Maguire, J.R., Hartl, C., Philippakis, A.A., del Angel, G., Rivas, M.A., Hanna, M., et al. (2011). A framework for variation discovery and genotyping using next-generation DNA sequencing data. Nat. Genet. *43*, 491–498.

Dobin, A., Davis, C.A., Schlesinger, F., Drenkow, J., Zaleski, C., Jha, S., Batut, P., Chaisson, M., and Gingeras, T.R. (2013). STAR: ultrafast universal RNA-seq aligner. Bioinformatics *29*, 15–21.

Durand, N.C., Robinson, J.T., Shamim, M.S., Machol, I., Mesirov, J.P., Lander, E.S., and Aiden, E.L. (2016). Juicebox provides a visualization system for Hi-C contact maps with unlimited zoom. Cell Syst. *3*, 99–101.

Filbin, M.G., Tirosh, I., Hovestadt, V., Shaw, M.L., Escalante, L.E., Mathewson, N.D., Neftel, C., Frank, N., Pelton, K., Hebert, C.M., et al. (2018). Developmental and oncogenic programs in H3K27M gliomas dissected by single-cell RNA-seq. Science *360*, 331–335.

Flavahan, W.A., Drier, Y., Liau, B.B., Gillespie, S.M., Venteicher, A.S., Stemmer-Rachamimov, A.O., Suvà, M.L., and Bernstein, B.E. (2016). Insulator dysfunction and oncogene activation in IDH mutant gliomas. Nature *529*, 110–114.

Fontebasso, A.M., Schwartzentruber, J., Khuong-Quang, D.A., Liu, X.Y., Sturm, D., Korshunov, A., Jones, D.T., Witt, H., Kool, M., Albrecht, S., et al. (2013). Mutations in SETD2 and genes affecting histone H3K36 methylation target hemispheric high-grade gliomas. Acta Neuropathol. *125*, 659–669.

Fontebasso, A.M., Gayden, T., Nikbakht, H., Neirinck, M., Papillon-Cavanagh, S., Majewski, J., and Jabado, N. (2014a). Epigenetic dysregulation: a novel pathway of oncogenesis in pediatric brain tumors. Acta Neuropathol. *128*, 615–627.

Fontebasso, A.M., Papillon-Cavanagh, S., Schwartzentruber, J., Nikbakht, H., Gerges, N., Fiset, P.O., Bechet, D., Faury, D., De Jay, N., Ramkissoon, L.A., et al. (2014b). Recurrent somatic mutations in ACVR1 in pediatric midline high-grade astrocytoma. Nat. Genet. *46*, 462–466.

Gessi, M., Gielen, G.H., Hammes, J., Dörner, E., Mühlen, A.Z., Waha, A., and Pietsch, T. (2013). H3.3 G34R mutations in pediatric primitive neuroectodermal tumors of central nervous system (CNS-PNET) and pediatric glioblastomas: possible diagnostic and therapeutic implications? J. Neurooncol. *112*, 67–72.

Hansen, D.V., Lui, J.H., Flandin, P., Yoshikawa, K., Rubenstein, J.L., Alvarez-Buylla, A., and Kriegstein, A.R. (2013). Non-epithelial stem cells and cortical interneuron production in the human ganglionic eminences. Nat. Neurosci. *16*, 1576–1587.

Hänzelmann, S., Castelo, R., and Guinney, J. (2013). GSVA: gene set variation analysis for microarray and RNA-seq data. BMC Bioinformatics *14*, 7.

Harutyunyan, A.S., Krug, B., Chen, H., Papillon-Cavanagh, S., Zeinieh, M., De Jay, N., Deshmukh, S., Chen, C.C.L., Belle, J., Mikael, L.G., et al. (2019). H3K27M induces defective chromatin spread of PRC2-mediated repressive H3K27me2/me3 and is essential for glioma tumorigenesis. Nat. Commun. *10*, 1262.

Heinrich, M.C., Corless, C.L., Demetri, G.D., Blanke, C.D., von Mehren, M., Joensuu, H., McGreevey, L.S., Chen, C.J., Van den Abbeele, A.D., Druker, B.J., et al. (2003). Kinase mutations and imatinib response in patients with metastatic gastrointestinal stromal tumor. J. Clin. Oncol. *21*, 4342–4349.

Heinz, S., Benner, C., Spann, N., Bertolino, E., Lin, Y.C., Laslo, P., Cheng, J.X., Murre, C., Singh, H., and Glass, C.K. (2010). Simple combinations of lineage-determining transcription factors prime cis-regulatory elements required for macrophage and B cell identities. Mol. Cell *38*, 576–589.

Ip, C.K.M., Ng, P.K.S., Jeong, K.J., Shao, S.H., Ju, Z., Leonard, P.G., Hua, X., Vellano, C.P., Woessner, R., Sahni, N., et al. (2018). Neomorphic PDGFRA extracellular domain driver mutations are resistant to PDGFRA targeted therapies. Nat. Commun. *9*, 4583.

Jessa, S., Blanchet-Cohen, A., Krug, B., Vladoiu, M., Coutelier, M., Faury, D., Poreau, B., De Jay, N., Hébert, S., Monlong, J., et al. (2019). Stalled developmental programs at the root of pediatric brain tumors. Nat. Genet. *51*, 1702–1713.

Karch, K.R., Sidoli, S., and Garcia, B.A. (2016). Identification and quantification of histone PTMs using high-resolution mass spectrometry. Methods Enzymol. *574*, 3–29.

Khuong-Quang, D.A., Buczkowicz, P., Rakopoulos, P., Liu, X.Y., Fontebasso, A.M., Bouffet, E., Bartels, U., Albrecht, S., Schwartzentruber, J., Letourneau, L., et al. (2012). K27M mutation in histone H3.3 defines clinically and biologically distinct subgroups of pediatric diffuse intrinsic pontine gliomas. Acta Neuropathol. *124*, 439–447.

Kim, S., Jeong, K., Bhutani, K., Lee, J., Patel, A., Scott, E., Nam, H., Lee, H., Gleeson, J.G., and Bafna, V. (2013). Virmid: accurate detection of somatic mutations with sample impurity inference. Genome Biol. *14*, R90.

Kloetgen, A., Thandapani, P., Ntziachristos, P., Ghebrechristos, Y., Nomikou, S., Lazaris, C., Chen, X., Hu, H., Bakogianni, S., Wang, J., et al. (2020). Three-dimensional chromatin landscapes in T cell acute lymphoblastic leukemia. Nat. Genet. *52*, 388–400.

Koboldt, D.C., Zhang, Q., Larson, D.E., Shen, D., McLellan, M.D., Lin, L., Miller, C.A., Mardis, E.R., Ding, L., and Wilson, R.K. (2012). VarScan 2: somatic mutation and copy number alteration discovery in cancer by exome sequencing. Genome Res. *22*, 568–576.

Korshunov, A., Capper, D., Reuss, D., Schrimpf, D., Ryzhova, M., Hovestadt, V., Sturm, D., Meyer, J., Jones, C., Zheludkova, O., et al. (2016). Histologically distinct neuroepithelial tumors with histone 3 G34 mutation are molecularly similar and comprise a single nosologic entity. Acta Neuropathol. *131*, 137–146.

Koschmann, C., Zamler, D., MacKay, A., Robinson, D., Wu, Y.M., Doherty, R., Marini, B., Tran, D., Garton, H., Muraszko, K., et al. (2016). Characterizing and targeting PDGFRA alterations in pediatric high-grade glioma. Oncotarget *7*, 65696–65706.

Krueger, F. (2012). Trim Galore. https://www.bioinformatics.babraham.ac.uk/projects/trim_galore/.

Krug, B., De Jay, N., Harutyunyan, A.S., Deshmukh, S., Marchione, D.M., Guilhamon, P., Bertrand, K.C., Mikael, L.G., McConechy, M.K., Chen, C.C.L., et al. (2019). Pervasive H3K27 Acetylation Leads to ERV Expression and a Therapeutic Vulnerability in H3K27M Gliomas. Cancer Cell *35*, 782–797.e8.

Landrum, M.J., Lee, J.M., Benson, M., Brown, G.R., Chao, C., Chitipiralla, S., Gu, B., Hart, J., Hoffman, D., Jang, W., et al. (2018). ClinVar: improving access to variant interpretations and supporting evidence. Nucleic Acids Res. *46* (D1), D1062–D1067.

Langmead, B., and Salzberg, S.L. (2012). Fast gapped-read alignment with Bowtie 2. Nat. Methods *9*, 357–359.

Larson, D.E., Harris, C.C., Chen, K., Koboldt, D.C., Abbott, T.E., Dooling, D.J., Ley, T.J., Mardis, E.R., Wilson, R.K., and Ding, L. (2012). SomaticSniper: identification of somatic point mutations in whole genome sequencing data. Bioinformatics *28*, 311–317.

Larson, J.D., Kasper, L.H., Paugh, B.S., Jin, H., Wu, G., Kwon, C.H., Fan, Y., Shaw, T.I., Silveira, A.B., Qu, C., et al. (2019). Histone H3.3 K27M Accelerates Spontaneous Brainstem Glioma and Drives Restricted Changes in Bivalent Gene Expression. Cancer Cell *35*, 140–155.e7.

Lewis, P.W., Müller, M.M., Koletsky, M.S., Cordero, F., Lin, S., Banaszynski, L.A., Garcia, B.A., Muir, T.W., Becher, O.J., and Allis, C.D. (2013). Inhibition of PRC2 activity by a gain-of-function H3 mutation found in pediatric glioblastoma. Science *340*, 857–861.

Li, H., and Durbin, R. (2009). Fast and accurate short read alignment with Burrows-Wheeler transform. Bioinformatics *25*, 1754–1760.

Li, H., Handsaker, B., Wysoker, A., Fennell, T., Ruan, J., Homer, N., Marth, G., Abecasis, G., and Durbin, R.; 1000 Genome Project Data Processing Subgroup (2009). The sequence alignment/map format and SAMtools. Bioinformatics *25*, 2078–2079.

Li, S., Mattar, P., Dixit, R., Lawn, S.O., Wilkinson, G., Kinch, C., Eisenstat, D., Kurrasch, D.M., Chan, J.A., and Schuurmans, C. (2014). RAS/ERK signaling controls proneural genetic programs in cortical development and gliomagenesis. J. Neurosci. *34*, 2169–2190.

Liao, Y., Smyth, G.K., and Shi, W. (2014). featureCounts: an efficient general purpose program for assigning sequence reads to genomic features. Bioinformatics *30*, 923–930.

Lindtner, S., Catta-Preta, R., Tian, H., Su-Feher, L., Price, J.D., Dickel, D.E., Greiner, V., Silberberg, S.N., McKinsey, G.L., McManus, M.T., et al. (2019). Genomic Resolution of DLX-Orchestrated Transcriptional Circuits Driving Development of Forebrain GABAergic Neurons. Cell Rep. *28*, 2048–2063.e8.

Liu, X.Y., Gerges, N., Korshunov, A., Sabha, N., Khuong-Quang, D.A., Fontebasso, A.M., Fleming, A., Hadjadj, D., Schwartzentruber, J., Majewski, J., et al. (2012). Frequent ATRX mutations and loss of expression in adult diffuse astrocytic tumors carrying IDH1/IDH2 and TP53 mutations. Acta Neuropathol. *124*, 615–625.

López-Juárez, A., Howard, J., Ullom, K., Howard, L., Grande, A., Pardo, A., Waclaw, R., Sun, Y.Y., Yang, D., Kuan, C.Y., et al. (2013). Gsx2 controls region-specific activation of neural stem cells and injury-induced neurogenesis in the adult subventricular zone. Genes Dev. *27*, 1272–1287.

Love, M.I., Huber, W., and Anders, S. (2014). Moderated estimation of fold change and dispersion for RNA-seq data with DESeq2. Genome Biol. *15*, 550.

Ma, F., and Pellegrini, M. (2020). ACTINN: automated identification of cell types in single cell RNA sequencing. Bioinformatics *36*, 533–538.

Ma, T., Wang, C., Wang, L., Zhou, X., Tian, M., Zhang, Q., Zhang, Y., Li, J., Liu, Z., Cai, Y., et al. (2013). Subcortical origins of human and monkey neocortical interneurons. Nat. Neurosci. *16*, 1588–1597.

Mackay, A., Burford, A., Carvalho, D., Izquierdo, E., Fazal-Salom, J., Taylor, K.R., Bjerke, L., Clarke, M., Vinci, M., Nandhabalan, M., et al. (2017). Integrated Molecular Meta-Analysis of 1,000 Pediatric High-Grade and Diffuse Intrinsic Pontine Glioma. Cancer Cell *32*, 520–537.e5.

Macosko, E.Z., Basu, A., Satija, R., Nemesh, J., Shekhar, K., Goldman, M., Tirosh, I., Bialas, A.R., Kamitaki, N., Martersteck, E.M., et al. (2015). Highly parallel genome-wide expression profiling of individual cells using nanoliter droplets. Cell *161*, 1202–1214.

Markovic-Mueller, S., Stuttfeld, E., Asthana, M., Weinert, T., Bliven, S., Goldie, K.N., Kisko, K., Capitani, G., and Ballmer-Hofer, K. (2017). Structure of the Full-length VEGFR-1 Extracellular Domain in Complex with VEGF-A. Structure *25*, 341–352.

Matys, V., Kel-Margoulis, O.V., Fricke, E., Liebich, I., Land, S., Barre-Dirrie, A., Reuter, I., Chekmenev, D., Krull, M., Hornischer, K., et al. (2006). TRANSFAC and its module TRANSCompel: transcriptional gene regulation in eukaryotes. Nucleic Acids Res. *34*, D108–D110.

McInnes, L., Healy, J., and Melville, J. (2018). Umap: Uniform manifold approximation and projection for dimension reduction. arXiv, arXiv:1802.03426. https://arxiv.org/abs/1802.03426.

Mizrak, D., Levitin, H.M., Delgado, A.C., Crotet, V., Yuan, J., Chaker, Z., Silva-Vargas, V., Sims, P.A., and Doetsch, F. (2019). Single-Cell Analysis of Regional Differences in Adult V-SVZ Neural Stem Cell Lineages. Cell Rep. *26*, 394–406.e5.

Nagy, C., Maitra, M., Tanti, A., Suderman, M., Théroux, J.-F., Mechawar, N., Ragoussis, J., and Turecki, G. (2019). Single-nucleus RNA sequencing shows convergent evidence from different cell types for altered synaptic plasticity in major depressive disorder. Nat. Neurosci. *23*, 771–781.

Neftel, C., Laffy, J., Filbin, M.G., Hara, T., Shore, M.E., Rahme, G.J., Richman, A.R., Silverbush, D., Shaw, M.L., Hebert, C.M., et al. (2019). An Integrative Model of Cellular States, Plasticity, and Genetics for Glioblastoma. Cell *178*, 835–849.e21.

Ngan, C.Y., Wong, C.H., Tjong, H., Wang, W., Goldfeder, R.L., Choi, C., He, H., Gong, L., Lin, J., Urban, B., et al. (2020). Chromatin interaction analyses elucidate the roles of PRC2-bound silencers in mouse development. Nat. Genet. *52*, 264–272.

Nitarska, J., Smith, J.G., Sherlock, W.T., Hillege, M.M., Nott, A., Barshop, W.D., Vashisht, A.A., Wohlschlegel, J.A., Mitter, R., and Riccio, A. (2016). A Functional Switch of NuRD Chromatin Remodeling Complex Subunits Regulates Mouse Cortical Development. Cell Rep. *17*, 1683–1698.

Nowakowski, T.J., Bhaduri, A., Pollen, A.A., Alvarado, B., Mostajo-Radji, M.A., Di Lullo, E., Haeussler, M., Sandoval-Espinosa, C., Liu, S.J., Velmeshev, D., et al. (2017). Spatiotemporal gene expression trajectories reveal developmental hierarchies of the human cortex. Science *358*, 1318–1323.

Parsons, D.W., Jones, S., Zhang, X., Lin, J.C., Leary, R.J., Angenendt, P., Mankoo, P., Carter, H., Siu, I.M., Gallia, G.L., et al. (2008). An integrated genomic analysis of human glioblastoma multiforme. Science *321*, 1807–1812.

Pathania, M., De Jay, N., Maestro, N., Harutyunyan, A.S., Nitarska, J., Pahlavan, P., Henderson, S., Mikael, L.G., Richard-Londt, A., Zhang, Y., et al. (2017). H3.3^{K27M} Cooperates with Trp53 Loss and PDGFRA Gain in Mouse Embryonic Neural Progenitor Cells to Induce Invasive High-Grade Gliomas. Cancer Cell *32*, 684–700.e9.

Paugh, B.S., Zhu, X., Qu, C., Endersby, R., Diaz, A.K., Zhang, J., Bax, D.A., Carvalho, D., Reis, R.M., Onar-Thomas, A., et al. (2013). Novel oncogenic PDGFRA mutations in pediatric high-grade gliomas. Cancer Res. *73*, 6219–6229.

Petryniak, M.A., Potter, G.B., Rowitch, D.H., and Rubenstein, J.L. (2007). Dlx1 and Dlx2 control neuronal versus oligodendroglial cell fate acquisition in the developing forebrain. Neuron *55*, 417–433.

Pollen, A.A., Nowakowski, T.J., Chen, J., Retallack, H., Sandoval-Espinosa, C., Nicholas, C.R., Shuga, J., Liu, S.J., Oldham, M.C., Diaz, A., et al. (2015). Molecular identity of human outer radial glia during cortical development. Cell *163*, 55–67.

Qiu, X., Hill, A., Packer, J., Lin, D., Ma, Y.-A., and Trapnell, C. (2017a). Single-cell mRNA quantification and differential analysis with Census. Nat. Methods *14*, 309–315.

Qiu, X., Mao, Q., Tang, Y., Wang, L., Chawla, R., Pliner, H.A., and Trapnell, C. (2017b). Reversed graph embedding resolves complex single-cell trajectories. Nat. Methods *14*, 979–982.

Quinlan, A.R., and Hall, I.M. (2010). BEDTools: a flexible suite of utilities for comparing genomic features. Bioinformatics *26*, 841–842.

Raju, C.S., Spatazza, J., Stanco, A., Larimer, P., Sorrells, S.F., Kelley, K.W., Nicholas, C.R., Paredes, M.F., Lui, J.H., Hasenstaub, A.R., et al. (2018). Secretagogin is Expressed by Developing Neocortical GABAergic Neurons in Humans but not Mice and Increases Neurite Arbor Size and Complexity. Cereb. Cortex *28*, 1946–1958.

Ramsey, S.A., Knijnenburg, T.A., Kennedy, K.A., Zak, D.E., Gilchrist, M., Gold, E.S., Johnson, C.D., Lampano, A.E., Litvak, V., Navarro, G., et al. (2010). Genome-wide histone acetylation data improve prediction of mammalian transcription factor binding sites. Bioinformatics *26*, 2071–2075.

Ran, F.A., Hsu, P.D., Wright, J., Agarwala, V., Scott, D.A., and Zhang, F. (2013). Genome engineering using the CRISPR-Cas9 system. Nat. Protoc. *8*, 2281–2308.

Rao, S.S., Huntley, M.H., Durand, N.C., Stamenova, E.K., Bochkov, I.D., Robinson, J.T., Sanborn, A.L., Machol, I., Omer, A.D., Lander, E.S., and Aiden, E.L. (2014). A 3D map of the human genome at kilobase resolution reveals principles of chromatin looping. Cell *159*, 1665–1680.

Rimmer, A., Phan, H., Mathieson, I., Iqbal, Z., Twigg, S.R.F., Wilkie, A.O.M., McVean, G., and Lunter, G.; WGS500 Consortium (2014). Integrating mapping-, assembly- and haplotype-based approaches for calling variants in clinical sequencing applications. Nat. Genet. *46*, 912–918.

Robinson, J.T., Thorvaldsdóttir, H., Winckler, W., Guttman, M., Lander, E.S., Getz, G., and Mesirov, J.P. (2011). Integrative genomics viewer. Nat. Biotechnol. https://www.nature.com/articles/nbt.1754

Saunders, C.T., Wong, W.S., Swamy, S., Becq, J., Murray, L.J., and Cheetham, R.K. (2012). Strelka: accurate somatic small-variant calling from sequenced tumor-normal sample pairs. Bioinformatics *28*, 1811–1817.

Schmitges, F.W., Prusty, A.B., Faty, M., Stützer, A., Lingaraju, G.M., Aiwazian, J., Sack, R., Hess, D., Li, L., Zhou, S., et al. (2011). Histone methylation by PRC2 is inhibited by active chromatin marks. Mol. Cell *42*, 330–341.

Schwartzentruber, J., Korshunov, A., Liu, X.Y., Jones, D.T., Pfaff, E., Jacob, K., Sturm, D., Fontebasso, A.M., Quang, D.A., Tönjes, M., et al. (2012). Driver mutations in histone H3.3 and chromatin remodelling genes in paediatric glioblastoma. Nature *482*, 226–231.

Sergushichev, A.A. (2016). An algorithm for fast preranked gene set enrichment analysis using cumulative statistic calculation. bioRxiv. https://doi.org/10.1101/060012.

Shim, A.H.-R., Liu, H., Focia, P.J., Chen, X., Lin, P.C., and He, X. (2010). Structures of a platelet-derived growth factor/propeptide complex and a platelet-derived growth factor/receptor complex. Proc. Natl. Acad. Sci. USA *107*, 11307–11312.

Shiraishi, Y., Sato, Y., Chiba, K., Okuno, Y., Nagata, Y., Yoshida, K., Shiba, N., Hayashi, Y., Kume, H., Homma, Y., et al. (2013). An empirical Bayesian framework for somatic mutation detection from cancer genome sequencing data. Nucleic Acids Res. *41*, e89.

Sidoli, S., Bhanu, N.V., Karch, K.R., Wang, X., and Garcia, B.A. (2016). Complete workflow for analysis of histone post-translational modifications using bottom-up mass spectrometry: from histone extraction to data analysis. J. Vis. Exp., 54112.

Solomon, D.A., Korshunov, A., Sill, M., Jones, D.T.W., Kool, M., Pfister, S.M., Fan, X., Bannykh, S., Hu, J., Danielpour, M., et al. (2018). Myxoid glioneuronal tumor of the septum pellucidum and lateral ventricle is defined by a recurrent *PDGFRA* p.K385 mutation and DNT-like methylation profile. Acta Neuropathologica. https://doi.org/10.1007/s00401-018-1883-2.

Stuart, T., Butler, A., Hoffman, P., Hafemeister, C., Papalexi, E., Mauck, W.M., 3rd, Hao, Y., Stoeckius, M., Smibert, P., and Satija, R. (2019). Comprehensive Integration of Single-Cell Data. Cell *177*, 1888–1902.e21.

Sturm, D., Witt, H., Hovestadt, V., Khuong-Quang, D.A., Jones, D.T., Konermann, C., Pfaff, E., Tönjes, M., Sill, M., Bender, S., et al. (2012). Hotspot mutations in H3F3A and IDH1 define distinct epigenetic and biological subgroups of glioblastoma. Cancer Cell *22*, 425–437.

Sturm, D., Orr, B.A., Toprak, U.H., Hovestadt, V., Jones, D.T.W., Capper, D., Sill, M., Buchhalter, I., Northcott, P.A., Leis, I., et al. (2016). New Brain Tumor Entities Emerge from Molecular Classification of CNS-PNETs. Cell *164*, 1060–1072.

Suzuki, H., Kumar, S.A., Shuai, S., Diaz-Navarro, A., Gutierrez-Fernandez, A., De Antonellis, P., Cavalli, F.M.G., Juraschka, K., Farooq, H., Shibahara, I., et al. (2019). Recurrent noncoding U1 snRNA mutations drive cryptic splicing in SHH medulloblastoma. Nature *574*, 707–711.

Thorvaldsdóttir, H., Robinson, J.T., and Mesirov, J.P. (2013). Integrative Genomics Viewer (IGV): high-performance genomics data visualization and exploration. Brief. Bioinform. *14*, 178–192.

Tickle, T., Tirosh, I., Georgescu, C., Brown, M., and Haas, B. (2020). inferCNV of the Trinity CTAT Project (Klarman Cell Observatory, Broad Institute of MIT and Harvard, Cambridge, MA, USA.).

Velmeshev, D., Schirmer, L., Jung, D., Haeussler, M., Perez, Y., Mayer, S., Bhaduri, A., Goyal, N., Rowitch, D.H., and Kriegstein, A.R. (2019). Single-cell genomics identifies cell type-specific molecular changes in autism. Science *364*, 685–689.

Venteicher, A.S., Tirosh, I., Hebert, C., Yizhak, K., Neftel, C., Filbin, M.G., Hovestadt, V., Escalante, L.E., Shaw, M.L., Rodman, C., et al. (2017). Decoupling genetics, lineages, and microenvironment in IDH-mutant gliomas by single-cell RNA-seq. Science *355*, eaai8478.

Verhaak, R.G., Hoadley, K.A., Purdom, E., Wang, V., Qi, Y., Wilkerson, M.D., Miller, C.R., Ding, L., Golub, T., Mesirov, J.P., et al.; Cancer Genome Atlas Research Network (2010). Integrated genomic analysis identifies clinically relevant subtypes of glioblastoma characterized by abnormalities in PDGFRA, IDH1, EGFR, and NF1. Cancer Cell *17*, 98–110.

Visel, A., Taher, L., Girgis, H., May, D., Golonzhka, O., Hoch, R.V., McKinsey, G.L., Pattabiraman, K., Silberberg, S.N., Blow, M.J., et al. (2013). A high-resolution enhancer atlas of the developing telencephalon. Cell *152*, 895–908.

Vladoiu, M.C., El-Hamamy, I., Donovan, L.K., Farooq, H., Holgado, B.L., Sundaravadanam, Y., Ramaswamy, V., Hendrikse, L.D., Kumar, S., Mack, S.C., et al. (2019). Childhood cerebellar tumours mirror conserved fetal transcriptional programs. Nature *572*, 67–73.

Waltman, L., and Van Eck, N.J. (2013). A smart local moving algorithm for large-scale modularity-based community detection. Eur. Phys. J. B *86*, 471.

Wang, K., Li, M., and Hakonarson, H. (2010). ANNOVAR: functional annotation of genetic variants from high-throughput sequencing data. Nucleic Acids Res. *38*, e164.

Wen, H., Li, Y., Xi, Y., Jiang, S., Stratton, S., Peng, D., Tanaka, K., Ren, Y., Xia, Z., Wu, J., et al. (2014). ZMYND11 links histone H3.3K36me3 to transcription elongation and tumour suppression. Nature *508*, 263–268.

Wingett, S., Ewels, P., Furlan-Magaril, M., Nagano, T., Schoenfelder, S., Fraser, P., and Andrews, S. (2015). HiCUP: pipeline for mapping and processing Hi-C data. F1000Res *4*, 1310.

Wu, G., Broniscer, A., McEachron, T.A., Lu, C., Paugh, B.S., Becksfort, J., Qu, C., Ding, L., Huether, R., Parker, M., et al.; St. Jude Children's Research Hospital–Washington University Pediatric Cancer Genome Project (2012). Somatic histone H3 alterations in pediatric diffuse intrinsic pontine gliomas and non-brainstem glioblastomas. Nat. Genet. *44*, 251–253.

Wu, G., Diaz, A.K., Paugh, B.S., Rankin, S.L., Ju, B., Li, Y., Zhu, X., Qu, C., Chen, X., Zhang, J., et al. (2014). The genomic landscape of diffuse intrinsic pontine glioma and pediatric non-brainstem high-grade glioma. Nat. Genet. *46*, 444–450.

Younesy, H., Möller, T., Lorincz, M.C., Karimi, M.M., and Jones, S.J.M. (2015). VisRseq: R-based visual framework for analysis of sequencing data. BMC Bioinformatics *16* (*Suppl 11*), S2.

Zhang, Y., Liu, T., Meyer, C.A., Eeckhoute, J., Johnson, D.S., Bernstein, B.E., Nusbaum, C., Myers, R.M., Brown, M., Li, W., and Liu, X.S. (2008). Model-based analysis of ChIP-Seq (MACS). Genome Biol. *9*, R137.

Zhang, Y., Shan, C.M., Wang, J., Bao, K., Tong, L., and Jia, S. (2017). Molecular basis for the role of oncogenic histone mutations in modulating H3K36 methylation. Sci. Rep. *7*, 43906.

STAR★METHODS

KEY RESOURCES TABLE

REAGENT or RESOURCE	SOURCE	IDENTIFIER
Antibodies		
phospho-p44/42 MAPK (Erk1/2) (Thr202/Tyr204)	Cell Signaling Technology	4376, RRID:AB_331772
PDGFRA	R&D Systems	AF-307-NA, RRID:AB_354459
Histone H3.3 G34R	RevMab	31-1120, RRID:AB_2716433
Histone H3.3 G34V	RevMab	31-1193, RRID:AB_2716435
Gsx2	Millipore Sigma	ABN162, RRID:AB_11203296
H3K27me3	Cell Signaling Technology	9733, RRID:AB_2616029
H3K27ac	Diagenode	C15410196, RRID:AB_2637079
H3K36me3	Active Motif	61021, RRID:AB_2614986
H3.3	Millipore	09–838, RRID:AB_10845793
SUZ12	Cell Signaling Technology	3737, RRID:AB_2196850
CTCF	Diagenode	C15410210, RRID:AB_2753160
Critical Commercial Assays		
Klenow fragment (3′ → 5′ exo-)	New England Biolabs	Cat#M0212L
T4 polynucleotide kinase	New England Biolabs	Cat#M0201L
NEB DNA Quick ligase	New England Biolabs	Cat# M2200
NEB T4 DNA polymerase I	New England Biolabs	Cat#M0203L
NEB Klenow exo minus	New England Biolabs	Cat#M0212L
DNA Polymerase I, Large (Klenow) Fragment	New England Biolabs	Cat# M0210L
Biotin-14-dATP	Life Technologies	Cat#19524-016
T4 DNA ligase	New England Biolabs	Cat#M0202M
KAPA HiFi HotStart ReadyMix	KAPA Biosystems	Cat#KK2602
Dynabeads MyOne Streptavidin T1 beads	Life technologies	Cat#65602
DpnII enzyme	New England Biolabs	Cat# R0543
Deposited Data		
ChIP-seq, RNA-seq, Hi-C sequencing data for cell lines and murine samples	This paper	GEO: GSE146731
WES, RNA-seq, ChIP-seq and scRNA-seq sequencing data for human tumors	This paper	EGA: EGAS00001004301
RNA-seq sequencing data for non-G34R/V tumor entities	Jessa et al., 2019	EGA: EGAD00001005131
Experimental Models: Organisms/Strains		
Mouse: NOD SCID: NOD.Cg-Prkdc^{scid}Il2rg^{tm1Wjl}/SzJ	The Jackson Laboratory	RRID:IMSR_JAX:005557
Mouse: B6C3F1/Crl	Charles River Laboratories	RRID:IMSR_CRL:031
Mouse: FoxG1-Cre: B6.129T(SJL)-Foxg1$^{tm1.1(cre)Ddmo}$/J	The Jackson Laboratory	RRID:IMSR_JAX:029690
Mouse: C57BL/6J	The Jackson Laboratory	RRID:IMSR_JAX:000664
Oligonucleotides		
H3F3A G34V gRNA: TTCTTCACCACTCCAGTAG	This paper	N/A
H3F3A G34R crRNA: TTCTTCACCCTTCCAGTAG	This paper	N/A
shATRX vector1: 5′-TTCATTTACATTCTCATCCGTG-3′	Pathania et al., 2017	N/A
shATRX vector2: 5′-TCATTTACATTCTCATCCG-3′	Pathania et al., 2017	N/A
Trp53 sgRNA: 5′-ACAGCCATCACCTCACTGCA-3′	Pathania et al., 2017	N/A

(*Continued on next page*)

Continued

REAGENT or RESOURCE	SOURCE	IDENTIFIER
Recombinant DNA		
pSpCas9(BB)-2A-Puro (PX459 V2.0)	Addgene	RRID:Addgene_62988
CAG-PBase, PBCAG-GFP	Chen and LoTurco, 2012	N/A
CRISPR/Cas9 pX330	Pathania et al., 2017	N/A
Software and Algorithms		
TrimGalore v0.6.5	Krueger, 2012	https://github.com/FelixKrueger/TrimGalore/releases
Cutadapt v2.6	Krueger, 2012	https://cutadapt.readthedocs.io/en/stable/
Fastqc v0.11.9	Krueger, 2012	https://github.com/s-andrews/FastQC
HiCUP v0.7.2	Wingett et al., 2015	https://github.com/nerves-hub/nerves_hub/releases
Bowtie2 v2.3.5	Wingett et al., 2015	http://bowtie-bio.sourceforge.net/bowtie2/index.shtml
Juicer and associated Juicer Tools v1.22.01	Durand et al., 2016	https://github.com/aidenlab/juicer
Juicebox	Durand et al., 2016	https://github.com/aidenlab/Juicebox
HIFI algorithm	Cameron et al., 2020	https://github.com/BlanchetteLab/HIFI
Samtools v0.1.19	Li et al., 2009	https://github.com/samtools/samtools
Trimmomatic v0.32	Bolger et al., 2014	http://www.usadellab.org/cms/?page=trimmomatic
FASTQC v0.11.2	N/A	http://www.bioinformatics.babraham.ac.uk/projects/fastqc/
STAR v2.3.0e	Dobin et al., 2013	https://github.com/alexdobin/STAR
featureCounts v1.4.4	Liao et al., 2014	http://bioinf.wehi.edu.au/featureCounts/
DESeq2 v1.14.1	Love et al., 2014	https://bioconductor.org/packages/release/bioc/html/DESeq2.html
fgsea v1.8.0	Sergushichev, 2016	https://bioconductor.org/packages/release/bioc/html/fgsea.html
GSVA v1.27.0	Hänzelmann et al., 2013	https://www.bioconductor.org/packages/release/bioc/html/GSVA.html
Monocle v2.0.1	Qiu et al., 2017a, 2017b	https://www.bioconductor.org/packages/release/bioc/html/monocle.html
Cell Ranger	10X Genomics	https://support.10xgenomics.com/single-cell-gene-expression/software/downloads/latest
Seurat v2.3	Butler et al., 2018	https://github.com/satijalab/seurat
Seurat v3.2.1	Stuart et al., 2019	https://github.com/satijalab/seurat
UMAP	McInnes et al., 2018	https://github.com/lmcinnes/umap
ACTINN	Ma and Pellegrini, 2020	https://github.com/mafeiyang/ACTINN
inferCNV	Tickle et al., 2020	https://github.com/broadinstitute/inferCNV
BWA-MEM	Li and Durbin, 2009	http://bio-bwa.sourceforge.net/bwa.shtml
Picard	Broad Institute	https://broadinstitute.github.io/picard/
BEDtools	Quinlan and Hall, 2010	https://bedtools.readthedocs.io/en/latest/
IGV	Robinson, 2011	http://software.broadinstitute.org/software/igv/
GATK	DePristo et al., 2011	https://gatk.broadinstitute.org/hc/en-us
Annovar	Wang et al., 2010	https://doc-openbio.readthedocs.io/projects/annovar/en/latest/
biobambam	Wellcome Sanger Institute	https://github.com/gt1/biobambam
MuTect2	Cibulskis et al., 2013	https://gatk.broadinstitute.org/hc/en-us/articles/360037593851-Mutect2
EBCall	Shiraishi et al., 2013	https://github.com/friend1ws/EBCall
Varscan2	Koboldt et al., 2012	http://dkoboldt.github.io/varscan/

(*Continued on next page*)

Continued

REAGENT or RESOURCE	SOURCE	IDENTIFIER
Strelka	Saunders et al., 2012	https://github.com/Illumina/strelka
SomaticSniper	Larson et al., 2012	http://gmt.genome.wustl.edu/packages/somatic-sniper/
Virmid	Kim et al., 2013	https://sourceforge.net/p/virmid/wiki/Home/
Platypus	Rimmer et al., 2014	https://www.well.ox.ac.uk/research/research-groups/lunter-group/lunter-group/platypus-a-haplotype-based-variant-caller-for-next-generation-sequence-data
GenPipes v3.1.2	Bourgey et al., 2019	https://bitbucket.org/mugqic/genpipes/src/master/
Homer v4.9.1	Heinz et al., 2010	http://homer.ucsd.edu/homer/
VisRSeq v0.9.40	Younesy et al., 2015	https://visrsoftware.github.io/
SeqMonk	Babraham Bioinformatics	https://www.bioinformatics.babraham.ac.uk/projects/seqmonk/
MACS	Zhang et al., 2008	https://github.com/macs3-project/MACS

RESOURCE AVAILABILITY

Lead Contact

Further information and requests for resources and reagents should be directed to and will be fulfilled by the Lead Contact, Nada Jabado (nada.jabado@mcgill.ca).

Materials Availability

This study did not generate new unique reagents.

Data and Code Availability

ChIP-seq, RNA-seq, Hi-C sequencing data for cell lines and murine samples (Table S7) have been deposited in the Gene Expression Omnibus (GEO) under accession number GEO: GSE146731. WES, bulk RNA-seq, ChIP-seq, and scRNA-seq sequencing data for human tumors (Table S7) have been deposited in the European Genome-phenome Archive (EGA) under accession number EGA: EGAS00001004301. Bulk RNA-seq sequencing data for non-G34R/V tumor entities have been previously deposited in EGA under dataset accession number EGA: EGAD00001005131.

EXPERIMENTAL MODEL AND SUBJECT DETAILS

Patient samples and clinical information

Protocols for this study involving collection of patient samples and information were approved by the Research Ethics and Review Board of McGill University and affiliated Hospitals Research Institutes. Informed consent was obtained from all research participants. Clinical information (age, sex) and mutation status of primary HGG tumor samples are presented in Table S1.

Primary cell lines

We thank Drs. Angel M. Carcaboso and Dinesh Rakheja for generously sharing primary HGG-derived cell lines. The HSJD-GBM002 cell line was cultured in NeuroCult NS-A proliferation media (StemCell Technologies) supplemented with bFGF (10 ng/mL), rhEGF (20 ng/mL), and heparin (0.0002%) (StemCell Technologies) and on plates coated with poly-L-ornithine (0.01%) (Sigma) and laminin (0.01 mg/mL) (Sigma). KNS-42, PS10-801 and CMC1118G8 cell lines were cultured in DMEM containing 4.5 g/L glucose, L-glutamine, phenol red, and 10% FBS (Wisent). All lines were tested monthly for mycoplasma contamination (MycoAlert Mycoplasma Detection kit by Lonza), and STR fingerprinting was regularly performed. Clinical information (age, sex) and mutation status of primary HGG cell lines are presented in Table S7.

Animal models

All mice were housed, bred, and subjected to listed procedures according to the McGill University Health Center Animal Care Committee and in compliance with Canadian Council on Animal Care guidelines, and Animal Welfare and Ethical Review Body (AWERB) and UK Home Office guidelines (Project license 70/8240, 70/7428 and 80/2325). Live colonies were maintained and genotyped as per

Jackson Laboratories guidelines and protocols. Mice were housed together and monitored daily for neurological symptoms of brain tumors (weight loss, epilepsy, altered gait, lethargy) and euthanized immediately at clinical endpoint when recommended by veterinary and biological services staff members.

Female NOD SCID (RRID:IMSR_JAX:005557) mice (4-6 weeks, 18-25 g) were used for xenograft experiments. Tissue from ganglionic eminences and cortex was isolated from embryos at gestation day E13 (plug day considered as day 0) using B6C3F1/J (RRID:IMSR_CRL:031) or FoxG1-cre (B6.129T(SJL)-Foxg1tm1.1(cre)Ddmo/J) (RRID:IMSR_JAX:029690) pregnant mice (6-8 weeks, 20-25 g). In utero electroporations were performed on pregnant C57BL/6J (RRID:IMSR_JAX:000664) female mice at E13.5.

METHOD DETAILS

Immunohistochemistry for patient tumors

Immunohistochemistry (IHC) was performed at Histology Platform (RI-MUHC) and the Segal Cancer Centre Research Pathology Facility (Jewish General Hospital). G34R/V high-grade glioma samples were cut at 4-6 μm, placed on SuperFrost/Plus slides (Fisher) and dried overnight at 37°C, before IHC processing. After de-paraffinization and epitope retrieval, sections were incubated with primary antibodies: phospho-p44/42 MAPK (Erk1/2) (Thr202/Tyr204, 4376 Cell Signaling, RRID:AB_331772) in 1:100; and PDGFRA (AF-307-NA, R&D Systems, 1:100, RRID:AB_354459). Slides were then loaded onto the Discovery XT Autostainer or Ventana Discovery Ultra Instrument (Ventana Medical Systems). Slides were counterstained with hematoxylin, blued with Bluing Reagent, washed, dehydrated through graded alcohols, cleared in xylene, and mounted with mounting medium (Eukitt, Fluka Analytical) or Leica CV 5030 coverslipper. Sections were analyzed by conventional light microscopy or scanned using the Aperio AT Turbo Scanner (Leica Biosystems).

CRISPR/Cas9 gene editing

CRISPR-Cas9 editing of KNS-42 cell line was performed as described in Ran et al. (2013). The pSpCas9(BB)-2A-Puro (PX459 V2.0) was a gift from Feng Zhang (Addgene plasmid #62988). A sgRNA targeting the *H3F3A* G34V mutation was cloned into the plasmid, and the construct was transfected using lipofectamine 2000 (Thermo Fisher Scientific) as per manufacturer's protocol. Transfected cells were selected with puromycin for 3 days. CRISPR-Cas9 editing of HSJD-GBM002 cell line was performed by designing a synthetic ALT-R crRNA (IDT) guide targeting the *H3F3A* G34R mutation. Nucleofection was performed using program A-023 on the Amaxa Nucleofector 2b (Lonza) device, following manufacturer's instructions to introduce crRNA, tracrRNA and recombinant Alt-R S.p. Cas9 Nuclease V3 (IDT). Single cell clones were isolated by limiting dilution, expanded and screened for editing events at the target locus by Sanger sequencing and confirmed through targeted deep sequencing using Illumina MiSeq.

Guide RNA sequences:

H3F3A G34V gRNA: TTCTTCACCACTCCAGTAG
H3F3A G34R crRNA: TTCTTCACCCTTCCAGTAG

Immunofluorescence

HSJD-GBM002 and KNS-42 CRISPR clones were cultured in 8-well chambers. Cells were fixed with 4% paraformaldehyde and 15% sucrose in PBS solution for 20 minutes at 4°C. Permeabilization was performed with 0.1% Triton X-100 for 3 mins on ice, followed by incubation in blocking buffer of 5% goat serum for 1 h at room temperature. Cells were incubated overnight at 4°C with primary antibodies specific for Histone H3.3 G34R or G34V (RevMab 31-1120 RRID:AB_2716433 and 31-1193 RRID:AB_2716435), diluted 1:200 in 1% BSA/PBS solution. Incubation with secondary anti-rabbit Alexa Fluor 488 or 594 antibodies (ThermoFisher Scientific) was performed at 1:1000 dilution in PBS under light protection for 90 minutes. ProLong Diamond Antifade Mountant with blue DNA DAPI stain (ThermoFisher Scientific) was applied. Fluorescent signal was captured the following day.

Histone post-translational modification by nLC/MS

The complete workflow for histone extraction, LC/MS, and data analysis was described in detail (Karch et al., 2016; Sidoli et al., 2016). Briefly, cell pellets (~1 × 10^6 cells) were lysed on ice in nuclear isolation buffer supplemented with 0.3% NP-40 alternative. Isolated nuclei were incubated with 0.4 N H2SO4 for 3 h at 4°C with agitation. 100% trichloroacetic acid (w/v) was added to the acid extract to a final concentration of 20% and samples were incubated on ice overnight to precipitate histones. The resulting histone pellets were rinsed with ice cold acetone + 0.1% HCl and then with ice cold acetone before resuspension in water and protein estimation by Bradford assay. Approximately 20 μg of histone extract was then resuspended in 100 mM ammonium bicarbonate and derivatized with propionic anhydride. 1 μg of trypsin was added and samples were incubated overnight at 37°C. After tryptic digestion, a cocktail of isotopically-labeled synthetic histone peptides was spiked in at a final concentration of 250 fmol/μg and propionic anhydride derivatization was performed for second time. The resulting histone peptides were desalted using C18 Stage Tips, dried using a centrifugal evaporator, and reconstituted using 0.1% formic acid in preparation for nanoLC-MS analysis.

nanoLC was performed using a Thermo ScientificTM Easy nLCTM 1000 equipped with a 75 μm × 20 cm in-house packed column using Reprosil-Pur C18-AQ (3 μm; Dr. Maisch GmbH, Germany). Buffer A was 0.1% formic acid and Buffer B was 0.1% formic acid in

80% acetonitrile. Peptides were resolved using a two-step linear gradient from 5 to 33% B over 45 min, then from 33 to 90% B over 10 min at a flow rate of 300 nL/min. The HPLC was coupled online to an Orbitrap Elite mass spectrometer operating in the positive mode using a Nanospray FlexTM Ion Source (Thermo Scientific) at 2.3 kV. Two full MS scans (m/z 300–1100) were acquired in the orbitrap mass analyzer with a resolution of 120,000 (at 200 m/z) every 8 DIA MS/MS events using isolation windows of 50 m/z each (e.g., 300–350, 350–400, ...,650–700). MS/MS spectra were acquired in the ion trap operating in normal mode. Fragmentation was performed using collision-induced dissociation (CID) in the ion trap mass analyzer with a normalized collision energy of 35. AGC target and maximum injection time were 10e6 and 50 ms for the full MS scan, and 10e4 and 150 ms for the MS/MS can, respectively. Raw files were analyzed using EpiProfile.

Mouse orthotopic xenograft

Female NOD SCID mice (4-6 weeks) were used for xenograft experiments. Mice were injected with the following cell lines at a density of $7x10^5$ cells in the parietal cortex, using the following coordinates from bregma: anteroposterior −1.94 mm, mediolateral 2.5 mm, dorsoventral 1.4 mm. For KNS-42: (1) Parental cells (*H3F3A*$^{+/G34V}$, n = 3), Clone 1-9 (*H3F3A*$^{+/-}$, n = 3), Clone 2-2 (*H3F3A*$^{+/-}$, n = 3). For HSJD-GBM002: (1) Parental cells (*H3F3A*$^{+/G34R}$, n = 2), Clone F06 (*H3F3A*$^{+/G34R}$, n = 4), Clone A10 (*H3F3A*$^{+/G34R}$, n = 4), Clone C08 (*H3F3A*$^{+/-}$, n = 4), Clone A09 (*H3F3A*$^{+/+}$, n = 4). Stereotaxic injections were performed using the Robot Stereotaxic machine from Neurostar. At clinical endpoint, brains were removed and fixed in formalin for histological analysis. Kaplan-Meier survival curves were generated using Graphpad Prism software.

Ganglionic eminences and cortices isolation

Tissue from ganglionic eminences (GEs) and cortex was isolated from embryos at gestation day 13 (plug day considered as day 0) using B6C3F1/J or FoxG1-cre (B6.129T(SJL)-Foxg1tm1.1(cre)Ddmo/J) pregnant mice. Mice were anesthetized, and euthanized by CO_2 exposure followed by cervical dislocation. Uterine horns containing the embryos were removed and placed in cold 1X HBSS buffer (containing 1% Penicillin/streptomycin). Embryos were removed and dissected under the microscope. The brain was removed from the skull, forebrain was separated, and placed in a new Petri dish containing cold 1X HBSS buffer. Cortices of each hemisphere were cut using micro-scissors to expose the GEs. GEs were then isolated and placed in 12-well plates until cell dissociation. Matching cortices were recovered and similarly processed. Cells were dissociated by pipetting the tissue into a single-cell suspension that was processed as per requirements for downstream experiments. In addition, whole brains at E13 and P0 were fixed in formalin for histological analyses.

IHC for PDOX and mouse brain tissue

Immunohistochemistry (IHC) was performed at Histology Platform (RI-MUHC) and the Segal Cancer Centre Research Pathology Facility (Jewish General Hospital). PDOX and mouse brain tissue samples were cut at 4-6 μm, placed on SuperFrost/Plus slides (Fisher) and dried overnight at 37°C, before IHC processing. After de-paraffinization and epitope retrieval, sections were incubated with primary antibodies: Gsx2 (ABN162, Millipore Sigma RRID:AB_11203296) in 1:100; H3.3 G34R (RM240, RevMAb Biosciences, RRID:AB_2716433) in 1:50; and H3.3 G34V (RM307, RevMAb Biosciences RRID:AB_2716435) in 1:40. Slides were then loaded onto the Discovery XT Autostainer or Ventana Discovery Ultra Instrument (Ventana Medical Systems). Slides were counterstained with hematoxylin, blued with Bluing Reagent, washed, dehydrated through graded alcohols, cleared in xylene, and mounted with mounting medium (Eukitt, Fluka Analytical) or Leica CV 5030 coverslipper. Sections were analyzed by conventional light microscopy or scanned using the Aperio AT Turbo Scanner (Leica Biosystems).

Mouse in utero electroporation (IUE)

Vector Construction

The piggyBac donor and helper vector system (CAG-PBase, PBCAG-GFP) was used to transduce NPCs in utero as described previously (Chen and LoTurco, 2012). Two ATRX shRNA vectors, cDNA encoding murine Pdgfra and cDNA encoding C-terminal HA-tagged *Drosophila His3.3A* (highly conserved ortholog of mammalian *H3f3a*) were cloned into the PBCAG-GFP vector to generate shAtrx-Pdgfra^{WT}-H3f3a^{WT} constructs, previously described in Pathania et al. (2017). CRISPR/Cas9 pX330 vectors containing *Trp53*-targeted gRNA were similarly used. G34R and Pdgfra^{D842V} mutants were generated using Quikchange Lightning site-directed mutagenesis (Agilent).

shRNA and sgRNA sequences:

shATRX vector1: 5′-TTCATTTACATTCTCATCCGTG-3′
shATRX vector2: 5′-TCATTTACATTCTCATCCG-3′
Trp53 sgRNA: 5′-ACAGCCATCACCTCACTGCA-3′

In Utero Electroporation

In utero electroporations were performed using sterile technique on isoflurane/oxygen-anesthetized pregnant C57BL/6J female mice at E13.5 (cortex) as described (Nitarska et al., 2016). Analgesic support was provided pre-emptively (subcutaneous delivery of Vetergesic and Carpofen at 0.1 mg/kg and 5 mg/kg, respectively). Uterine horns were exposed through a 1 cm incision and individual

embryos were digitally manipulated into the correct orientation for intraventricular injection. Pulled borosilicate capillaries were loaded with endotoxin-free DNA and Fast Green dye (0.05%, Sigma) for visualization, and a microinjector (Eppendorf) was used to inject either the lateral or fourth ventricles with the DNA-dye mixture. 3-5 plasmids were injected simultaneously, each at a final concentration of 2 μg/μl and 1-2 μL of total solution was injected per embryo. DNA was electroporated into cortical neural progenitors using 5 mm tweezertrodes (BTX), or into lower rhombic lip progenitors using 3 mm tweezertrodes, applying 5 square pulses at 35 V, 50 ms each with 950 ms intervals. The embryos were returned into the abdominal cavity, the muscle and skin were sutured and the animal was monitored until fully recovered from the procedure.

Ex vivo NPC Isolation and Culture

Animals were euthanized by CO_2 exposure and/or cervical dislocation and cortices were rapidly dissected in ice-cold dissociation medium containing: 20 mM glucose, 81.8 mM Na_2SO_4, 30 mM K_2SO_4, 5.8 mM $MgCl_2$, 250 μM $CaCl_2$, 1 mM HEPES, 160 μM NaOH, 0.8 mM kynurenic acid, 50 μM D-APV, 100 U/mL penicillin, 100 μg/mL streptomycin, 5 μg/ml plasmocin and 100 μg/ml primocin. GFP^+ regions were microdissected under an epifluorescence stereomicroscope in the same medium and enzymatically digested into a single-cell suspension using the Papain Dissociation System (Worthington Biochemicals) followed by mechanical trituration through a series of fire-polished Pasteur pipettes. The dissociated cell solution was then separated on an OptiPrep density gradient to remove debris and $GFP^+TdTomato^+$ cells were sorted using a FACSAria III or LSRFortessa X-20 (BD Biosciences) into Hibernate-E media (Life Technologies) containing 2% B-27, 2 mM Glutamax, 0.8 mM kynurenic acid, 50 μM D-APV, 100 U/mL penicillin, 100 μg/mL streptomycin, 5 μg/ml plasmocin and 100 μg/ml primocin. Sorted cells were plated into NeuroCult NSC proliferation media (STEMCELL Technologies) containing 10 ng/ml of epidermal growth factor (EGF, Peprotech) and basic fibroblast growth factor (bFGF, Peprotech) on laminin-coated culture vessels (Sigma).

Model Figures

Graphical abstract was created with the aid of BioRender software.

QUANTIFICATION AND STATISTICAL ANALYSIS

Description of statistical details for each experiment can be found in figure legends.

Structural molecular modeling

The PDGFRA mutants Y288C and C235Y, in the Ig-like domain 3, were modeled using the structure of PDGFRB (PDB ID: 3MJG), with a 29% sequence identity to PDGFRA in this region, where the residues of interest are conserved (Shim et al., 2010). The PDGFRA mutant K385M, in the Ig-like domain 4, was modeled using the structure of Vascular Endothelial Growth Factor Receptor (VGFR1) (PDB ID: 5T89), with a 29% sequence identity to PDGFRA in this region (Markovic-Mueller et al., 2017). The corresponding three residues were mutated and subsequently modeled in PyMOL.

Whole exome- and RNA-sequencing

WES sample and library preparation

DNA was extracted from tumors using the AllPrep DNA/RNA/miRNA Universal Kit (QIAGEN) following manufacturer instructions. The Nextera Rapid Capture Exome kit (Illumina) or SureSelect Reagent Exome kit (Agilent) were used to prepare libraries according to manufacturer's instructions. Paired-end sequencing (100 bp) was performed on Illumina HiSeq 2500/4000 platform.

RNA-seq sample and library preparation

Total RNA was extracted from cell pellets using the Aurum Total RNA Mini Kit (Bio-Rad) and tumors using the AllPrep DNA/RNA/miRNA Universal Kit (QIAGEN) according to instructions from the manufacturers. Library preparation was performed with ribosomal RNA (rRNA) depletion according to instructions from the manufacturer (Epicenter) to achieve greater coverage of mRNA and other long non-coding transcripts. Paired-end sequencing (100 bp) was performed on Illumina HiSeq 2500/4000 or NovaSeq 6000 platforms.

Data processing

Raw reads were trimmed using Trimmomatic v0.32 (Bolger et al., 2014). Adaptors and other Illumina-specific sequences were removed using palindrome mode. Next, a four-nucleotide sliding window was used to remove the bases once the average quality within the window fell below 30. Finally, reads shorter than 30 base pairs were dropped. For WES, cleaned reads were aligned to the human reference genome build hg19 using BWA-MEM (Li and Durbin, 2009) v0.7.17 with default settings. Read duplicates were removed using Picard tools v2.10.7. For RNA-seq, cleaned reads were aligned to the human reference genome build hg19 using STAR (Dobin et al., 2013) v2.3.0e with default settings. Multiple control metrics (Table S2A) were obtained using FASTQC (v0.11.2), samtools (Li et al., 2009) (v0.1.20), BEDtools (Quinlan and Hall, 2010) (v2.17.0) and custom scripts. For visualization, normalized Bigwig tracks were generated using BEDtools and UCSC tools. Integrative Genomic Viewer (Thorvaldsdóttir et al., 2013) was used for data visualization.

Variant calling

GATK (DePristo et al., 2011) v3.2-2 split'N'Trim was used to split reads in splice junction and rescale the mapping quality from 255 to 60. Then, GATK v3.2-2 IndelRealigner was used to realign the indels. Single-nucleotide variants were called using samtools (Li et al., 2009) (v0.1.20) mpileup and Annovar (Wang et al., 2010) v2016Feb01 was used for annotation (Table S1). More specifically, variants were annotated using hg19 build with RefSeq gene, dbSNP (snp138), 1000 Genomes Project (1000 g2015aug_all), SIFT, PolyPhen, LRT, MutationTaster, GERP++ and PhastCons. Variants with a total read count of less than 10, an alternative allele read count of less than three, a SNV ratio of less than 0.2, an indel read ratio of less than 0.15, a variant quality of less than 20, a mapping quality less than 15, a strand bias p value lower than 0.001 and a minor allele frequency higher than 0.001 were filtered out. Variants in repetitive regions (RepeatMasker, InterruptedRpts, segmentalDups, simpleRepeats and retroposons) or annotated as benign or likely benign from ClinVar (Landrum et al., 2018) were also filtered out. In addition, only variants of the following types were kept for downstream analyses: nonsynonymous SNV, splicing, splicing-extended, stop-gain and stop-loss. For gene amplification inference from WES, copy number variants (CNVs) were inferred from calculating RPKM coverage over annotated ENSEMBL genes. Samples were denoted as being positive for genic amplification if RPKM coverage was > 2-fold of the median RPKM.

Reconstruction of tumor phylogeny

For reconstruction of tumor phylogeny (Table S6), somatic variant calling was performed as previously described in Suzuki et al. (2019). Sequencing reads were aligned to human reference genome 'hs37d5′ by 1000 Genomes Project Phase II, using Burrows Wheeler aligner (BWA) – MEM (Li and Durbin, 2009) (v0.7.9) with '-T 0' option. Duplicates were marked using biobambam v.0.0.148. Samples without matched controls were run with a pseudo-control generated from 25 randomly selected WES samples from 1000 Genomes Project. Fastq files were mapped with the same settings and subsampled using the samtools view function to adjust sequencing coverage around 200x.

Variants were called using eight variant callers: MuTect2 (Cibulskis et al., 2013), EBCall (Shiraishi et al., 2013), Varscan2 (Koboldt et al., 2012), Strelka (Saunders et al., 2012), SomaticSniper (Larson et al., 2012), Virmid (Kim et al., 2013), Platypus (Rimmer et al., 2014) and Seurat (Christoforides et al., 2013). Each caller except for Strelka was run as previously described in Suzuki et al. (2019). Because the previously described method was for whole genome sequencing, Strelka was run with 'isSkipDepthFilters = 1'. Variants were identified if called by at least two callers, with $\geq$ 2 variant reads, $\geq$ 7 total reads and $\geq$ 0.05 variant allele frequency in the tumor and $\leq$ 1 variant read in the control, as calculated using the realignment function of Genomon-MutationFilter v.0.2.1.

For samples without matched controls, variants with a frequency $\geq$ 0.01 in 1000 Genomes, dbSNP138, Exome Aggregation Consortium database, NHLBI-ESP project, Kaviar Genomic Variant Database, Haplotype Reference Consortium database, Greater Middle East Variome, or Brazilian genomic variants database were discarded. Missense, synonymous mutations or non-frameshift indels registered in any SNP databases listed above a frequency of 0.01 and registered with fewer than 10 samples in COSMIC v87 were also discarded. Variants with SIFT score $\geq$ 0.05, PolyPhen-2 HDIV $\leq$ 0.908, PolyPhen-2 HVAR $\leq$ 0.956, ''polymorphism'' or ''polymorphism_automatic'' by MutationTaster, and variants ''predicted non-functional'' by MutationAssessor were discarded. Phylogenetic trees were constructed based on shared mutations detected in exons, splice sites, or UTRs. Fish-plots were generated using R package fish-plot (v0.5).

Gene expression quantification from RNA-seq data

Gene expression levels were estimated by quantifying reads uniquely mapped to exonic regions defined by ensGene annotation set from Ensembl (GRCh37, n = 60,234 genes) using featureCounts (Liao et al., 2014) (v1.4.4). Normalization (mean-of-ratios), variance-stabilized transformation of the data and differential gene expression analysis were performed using DESeq2 (Love et al., 2014) (v1.14.1). Unless otherwise stated, all reported *p-value*s have been adjusted for multiple testing using the Benjamini-Hochberg procedure. For tumors, comparisons were performed between G34R/V samples and each other tumor entity, with batch included as a covariate.

Assessment of developmental programs in tumors

To evaluate developmental gene programs in tumor samples, a reference panel of 167 forebrain cell-type specific signatures was assembled using data from five published scRNaseq atlases (Anderson et al., 2020; Jessa et al., 2019; Mizrak et al., 2019; Nowakowski et al., 2017; Velmeshev et al., 2019), spanning embryonal mouse forebrain, P9 striatum, adult mouse sub-ventricular zone, fetal huma n telencephalon, and pediatric and adult human cortex. For the mouse forebrain dataset, 100-gene signatures were used as reported in the original study. For the mouse striatum and the two human datasets, we derived 100-gene signatures from the published cluster markers by filtering out genes encoding ribosomal proteins (defined as having a gene symbol matching ''Rps,'' ''Rpl,'' ''Mrps,'' ''Mrpl''), and selecting the top 100 genes ranked by adjusted p value. Finally, for the mouse SVZ dataset, we called markers by performing differential gene expression analysis for the clusters reported by the authors in the original study, and subsequently derived the 100-gene signatures. Proliferating clusters were identified as those either annotated by the authors of the original studies, or with high expression of the proliferation marker *Top2a* (mean cluster expression > 0.4). Signatures from these clusters were excluded from analysis to prevent spurious enrichment due to cell cycle genes. Gene set enrichment analysis (GSEA) was performed with these signatures as input, applied to expressed genes in tumor transcriptomes (bulk RNA-seq) ranked using the Negative Binomial Wald test statistic from differential expression analysis, using the fgsea package (Sergushichev, 2016) (v1.8.0).

With fgsea, leading edge genes were obtained and normalized enrichment scores (NES) were computed by normalizing enrichment to the average enrichment of 10,000 random gene samples. *P values* were adjusted using the Benjamini-Hochberg procedure; signatures with adjusted *p value* < 0.01 were considered significantly enriched or depleted.

In the case of cell line datasets, the sample size was not adequate to perform GSEA, and thus enrichment of human radial glia and interneuron gene signatures was evaluated using single-sample GSEA (ssGSEA) (Barbie et al., 2009) using the GSVA (Hänzelmann et al., 2013) package (v1.27.0) as described previously (Jessa et al., 2019).

Gene expression profiling in normal development

Gene expression patterns of individual genes during human and mouse brain development were assessed across three previously reported scRNaseq reference developmental datasets (Anderson et al., 2020; Jessa et al., 2019; Nowakowski et al., 2017). Dendrograms of gene expression in neural cell types displayed in Figure 3 and Figure S5 were constructed as follows: normalized gene expression, cell type annotations (cluster assignments) and cluster gene signatures (cluster markers) were obtained from original publications (Jessa et al., 2019; Nowakowski et al., 2017). For each cluster and each gene, the mean expression across cells from the cluster was computed, as well as the proportion of cells in which the gene was detected (UMI counts > 0). Genes appearing in any of the clusters' signatures were selected for unsupervised hierarchical clustering. Spearman's rank correlation was used as distance metric on the cluster mean gene expression profiles, and complete linkage as agglomeration method. For visualization purposes, mean gene expression was scaled across clusters to [0,1].

Gene expression along interneuron differentiation

To profile gene expression during normal interneuron differentiation, displayed in Figure 2F, we used a previously reported reconstruction of the interneuron differentiation trajectory (Jessa et al., 2019), in which ventral radial glial cells, interneuron progenitors, and interneurons from the E12.5, E15.5, and P0 mouse forebrain were ordered in pseudotime using Monocle (Qiu et al., 2017a, 2017b). For visualization, Monocle (v2.0.1) was used to fit, for each gene, a smooth spline to the nonlinear expression dynamics as a function of pseudotime. Smoothed expression was then z-scored across pseudotime and extreme upper and lower values were set to 3 and −3 respectively. The genes displayed in the heatmap are the union of genes identified as specific to G34R/V gliomas by RNA-seq and ChIP-seq. Genes enriched in G34R/V were defined as those 1) in the leading edge of the human interneuron gene signature most significantly enriched in G34R/V (ranked by NES, GSEA analysis), or 2) significantly upregulated in G34R/V (adj. p value < 0.01 and log2 fold-change > 2, RNA-seq differential expression analysis) and enriched for promoter H3K27ac in G34R/V (z-score > 0.6, ChIP-seq analysis). Conversely, genes were defined as depleted in G34R/V were genes 1) in the leading edge of the human interneuron gene signature most significantly depleted in G34R/V (ranked by NES, GSEA analysis), or 2) significantly downregulated in G34R/V (adj. p value < 0.01 and log2 fold-change < −2, RNA-seq differential expression analysis) and enriched for promoter H3K27me3 in G34R/V (z-score > 0.6).

Chromatin immunoprecipitation sequencing

Sample and library preparation

ChIP-seq was performed as previously described in Harutyunyan et al. (2019). Briefly, cells (cell lines or dissociated tumor cells) were fixed with 1% formaldehyde (Sigma). Fixed cell preparations were washed, pelleted and stored at −80°C. Sonication of lysed nuclei (lysed in a buffer containing 1% SDS) was performed on a BioRuptor UCD-300 for 60 cycles, 10 s on 20 s off. Samples were checked for sonication efficiency using the criteria of 150–500 bp by gel electrophoresis. After sonication, the chromatin was diluted to reduce SDS level to 0.1% and before ChIP reaction 2% of sonicated *Drosophila* S2 cell chromatin was spiked-in the samples.

ChIP reaction for histone modifications was performed on a Diagenode SX-8G IP-Star Compact using Diagenode automated Ideal ChIP-seq Kit. Twenty-five microliter Protein A beads (Invitrogen) were washed and then incubated with antibodies (anti-H3K27me3 (1:40, CST 9733 RRID:AB_2616029), (anti-H3K27ac (1:80, Diagenode C15410196 RRID:AB_2637079)), (anti-H3K36me3 (1:100, Active Motif 61021 RRID:AB_2614986)), (anti-H3.3 (1:66, Millipore 09–838)), and 2 million cells of sonicated cell lysate combined with protease inhibitors for 10 h, followed by 20 min wash cycle with provided wash buffers. ChIP reactions for SUZ12 and CTCF were performed RRID:AB_10845793 as follows: anti-SUZ12 (1:150, CST 3737 RRID:AB_2196850) or anti-CTCF (1 μg/reaction, Diagenode C15410210 RRID:AB_2753160) antibodies were conjugated by incubating with 40 μl protein A beads at 4°C for 6 h, then chromatin from ~4 million cells was added in RIPA buffer, incubated at 4°C o/n, washed using buffers from Ideal ChIP-seq Kit (one wash with each buffer, corresponding to RIPA, RIPA + 500 mM NaCl, LiCl, TE), eluted from beads by incubating with Elution buffer for 30 min at room temperature.

Reverse cross linking took place on a heat block at 65°C for 4 h. ChIP samples were then treated with 2 μl RNase Cocktail at 65°C for 30 min followed by 2 μl Proteinase K at 65°C for 30 min. Samples were then purified with QIAGEN MiniElute PCR purification kit as per manufacturers' protocol. In parallel, input samples (chromatin from about 50,000 cells) were reverse crosslinked and DNA was isolated following the same protocol.

Library preparation was carried out using Kapa HTP Illumina library preparation reagents, following manufacturer's instructions. Briefly, 25 μl of ChIP sample was incubated with 45 μl end repair mix at 20°C for 30 min followed by Ampure XP bead purification. A tailing: bead bound sample was incubated with 50 μl buffer enzyme mix at 30°C for 30 min, followed by PEG/NaCl purification. Adaptor ligation: bead-bound sample was incubated with 45 μl buffer enzyme mix and 5 μl of TruSeq DNA adapters (Illumina), for

20°C 15 min, followed by PEG/NaCl purification (twice). Library enrichment: 12 cycles of PCR amplification. Size selection was performed after PCR using a 0.6 × /0.8x ratio of Ampure XP beads (double size selection) set to collect 250–450 bp fragments. ChIP libraries were sequenced on Illumina HiSeq 4000 or NovaSeq 6000 platforms at 50 bp single reads or paired-reads.

Data processing

Murine embryonic stem cell and adult cortex ChIP-seq datasets were obtained from the ENCODE consortium portal (Davis et al., 2018). E13.5 ganglionic eminence ChIP-seq were obtained from Lindtner et al., 2019 (GSE124936) (Lindtner et al., 2019). ChIP-seq datasets were processed using the ChIP-seq module of GenPipes (v3.1.2) (Bourgey et al., 2019). Briefly, raw reads were trimmed using Trimmomatic (Bolger et al., 2014) v0.32 to remove adaptor and sequencing-primer associated reads, then aligned to hg19 or mm10 using bwa-mem (Li and Durbin, 2009) (v0.7.12) with default parameters. PCR duplicate reads as defined by reads with identical mapping coordinates were then collapsed by Picard (v2.0.1) to produce uniquely aligned reads. Reads were then filtered for mapping quality of > 5. For single-end (SE) 50bp datasets, reads were extended by 250bp. Wiggle tracks are generated using uniquely aligned reads using Homer (v4.9.1) (Heinz et al., 2010). RPKM was calculated using VisRSeq (v0.9.40) (Younesy et al., 2015) or SeqMonk (v1.46) at annotated genes. Promoter is defined as a 5kb centered bin on the transcription start site. Median values were generated for promoter-associated H3K27me3 and H3K27ac in the two subgroups - 1) G34R/V tumors and 2) non-G34R/V IDH1, SETD2, and WT cortical tumors. Z-score was calculated from the median RPKM as $z-score = ((mutant\ median\ RPKM - WT\ median\ RPKM)/\sqrt{mutant\ median\ RPKM + WT\ median\ RPKM})$. Z-score > |0.5| were designated as significant changes for ChIP-seq datasets (Table S3). Gene ontology analyses were performed using PANTHER.

Core regulatory circuitry analysis

H3K27ac ChIP-sequence reads were aligned to the human genome (HG19) using Bowtie2 (Langmead and Salzberg, 2012) (v2.1.0) under default settings. PCR duplicates were removed using Picard tools generating BAM. Significant peaks were identified using Model- Based Analysis for ChIP-seq (MACS) (v1.4) (Zhang et al., 2008) with a p value cutoff of $1e^{-9}$. Peaks were annotated using HOMER (Heinz et al., 2010) (v3.12) with promoter regions classified as any peak within ± 2.5 kb of a transcriptional start site (TSS), and enhancer region greater than 2.5 kb from a TSS. Peaks were also annotated using ChIP-atlas annotating distal enhancers to genes based upon public CHIA-PET datasets. Super enhancers were identified using the ROSE algorithm with exclusion of peaks within ± 2.5 kb of a TSS and a stitch distance of 12.5 kb.

Core regulatory circuitry (CRC) analysis was used with default parameters to quantify the interaction network of transcription factor (TF) regulation at super enhancers. Briefly, for all promoters within 100 kb, the most acetylated promoter was assigned as the target of the SE (excluding promoters that overlap SEs, which are automatically assigned the target. If there were no active promoters within 100kb, the SE was assigned to the nearest active promoter. All SE-associated promoters annotated to regulate a TF were considered as the node-list for network construction. For any given TF (TFi), the IN degree was defined as the number of TFs with an enriched binding motif at the proximal SE or promoter of TFi. The OUT degree was defined as the number of TF associated SEs containing an enriched binding site for TFi. Within any given SE, enriched TF binding sites were determined at putative nucleosome free regions (valleys) flanked by high levels of H3K27ac. Valleys were calculated using an algorithm adapted from Ramsey et al. (2010). In these regions, we searched for enriched TF binding sites using the FIMO59 algorithm with TF position weight matrices defined in the TRANSFAC database (Matys et al. (2006). An FDR cutoff of 0.01 was used to identify enriched TF binding sites. Hierarchal clustering of core TFs were performed using the heatmap function of R, and Gene Ontology assessment was performed using PANTHER.

Hi-C chromatin conformation capture

Sample and library preparation

In situ Hi-C libraries were generated from patient-derived glioma cell lines (5 million cells each), and murine embryonic brain tissue (1-3 million cells per sample), as described in Rao et al. (2014) with minor modifications. Briefly, *in situ* Hi-C was performed in 7 steps: (1) crosslinking cells with formaldehyde, (2) digesting DNA using a 4-cutter restriction enzyme (DpnII) within intact permeabilized nuclei, (3) filling in, biotinylating the resulting 5′ overhangs and ligating the blunt ends, (4) shearing the DNA, (5) pulling down biotinylated ligation junctions with streptavidin beads, (6) library amplification and (7) analyzing fragments using paired end sequencing. As quality control (QC) steps, efficient sonication was checked by agarose DNA gel electrophoresis and for appropriate size selection by Agilent Bioanalyzer profiles for libraries. For final QC, we performed superficial sequencing on the Illumina Hiseq 2500 (~30M reads/sample) to assess quality of the libraries using percent of reads passing filter, percent of chimeric reads, and percent of forward-reverse pairs. Hi-C libraries were sequenced (paired-end, 125 bp) on the Illumina HiSeq2500 platform.

Hi-C data analysis

Hi-C reads were trimmed and assessed for quality control using the Trim Galore package (Krueger, 2012) (TrimGalore v0.6.5, Cutadapt v2.6 and Fastqc v0.11.9) (Table S4). Reads were then mapped to hg19 or mm10, and filtered for common Hi-C artifacts using HiCUP (Wingett et al., 2015) (HiCUP v0.7.2, Bowtie2 v2.3.5, R v3.6.0_3.9). Analysis of Hi-C libraries and downloaded files was performed using Juicer and associated Juicer Tools (Durand et al., 2016) (v1.22.01). Contact maps were generated using Juicer with the following parameter: -s DpnII. Map resolution was determined by using Juicer's "calculate_map_resolution.sh" script. All observed matrices were computed using HOMER, accounting for both the linear distance between two given loci and sequencing depth. Hi-C contact maps and associated annotations were visualized using Juicebox (Durand et al., 2016). We used the HIFI algorithm (Cameron et al., 2020) to process 5-kb resolution Hi-C data to obtain higher accuracy estimates of interaction frequencies, using the following

parameters: bandSize = 1000, outputNormalized, boundaryKS = 1000. Virtual 4C plots were derived using HIFI 5 kb resolution heatmaps. Observed/expected ratios were extracted using the dump function in Juicer Tools from HIFI heatmaps, using the following anchor regions: *PDGFRA*/*Pdgfra* promoter (chr4:55090000-55105000 in hg19, chr5:75140000-751550000 in mm10), or *GSX2*/*Gsx2* promoter (chr4:54960000-54970000 in hg19, chr5:75070000-75080000 in mm10). TAD boundaries were calculated using robusTAD tool (Dali et al., 2018) at a 50kb resolution. For loop quantification, we extracted and calculated the mean interaction values for each 5kb bin at our region of interest with *PDGFRA*/*Pdgfra* or *GSX2*/*Gsx2* promoters. Quantification of interactions within a TAD was computed as the sum of normalized (observed/expected) interaction scores (Kloetgen et al., 2020) for each cell line, extracted using the dump function from Juicer Tools for the region of interest. Significant differences in intra-TAD activity or interaction loops anchored on *PDGFRA* or *GSX2* promoters were assessed using a one-tailed t test. All related quantification and statistical analyses are provided in Table S4. Publicly available Hi-C datasets on murine embryonic stem cells were downloaded from GEO (GSE96107) (Bonev et al., 2017), and processed as described above.

Hi-C data visualization

To ensure visual clarity for Hi-C heatmaps, we either plotted observed/expected interaction values or observed interaction values alone. When plotting broader windows for the Hi-C interaction heatmaps (e.g., Figure S5F), we plotted observed values since observed/expected values tend to exaggerate the intensity of long-range interactions. Observed values also allow better visualization of TAD structures across large-scale windows. Similarly, we represented observed values to represent the *Gsx2*-hs687 interaction in Figure S5G because they are better suited for small distances, unlike observed/expected values that tend to underestimate short interactions due to their proximity in the linear genome. By contrast, we represented observed/expected values for mid-range interactions across the *PDGFRA*-hs687 locus, as depicted in Figures 4A and 4B.

Single-cell and single-nuclei RNaseq

Tissue handling and dissociation

Fresh tumors collected after surgery were enzymatically digested and mechanically dissociated using the papain version of the Brain Tumor Dissociation kit (Miltenyi Biotech) or the Worthington Papain dissociation kit (Table S6). Red blood cells were lysed by ammonium chloride treatment for 5 min on ice. Cell viability was assessed with Trypan Blue. For samples with low viability (< 60%), dissociated cells were enriched for live cells using the Dead Cell Removal kit(Miltenyi Biotech). 10,000 dissociated cells per sample were loaded on the 10X Genomics Chromium controller. Nuclei were prepared from frozen tissue (5-50 mg) as previously described (Nagy et al., 2019). Nuclei concentration was assessed using the ReadyProbes Cell Viability fluorescence assay (ThermoFisher Scientific). As nuclei capture was 55%–60% less efficient than cell capture, we aimed to capture 22,000 nuclei per sample.

Single-cell and single-nuclei library preparation

The Chromium Single Cell 3′ (10X Genomics, Version 3) protocol was strictly followed to prepare libraries. The 10X libraries were sequenced on the Illumina HiSeq4000 or NovaSeq sequencing platforms (Table S6).

Data processing and quality control

Cell Ranger (10X Genomics) was used with default parameters to demultiplex reads and align sequencing reads to the genome, distinguish cells from background, and obtain gene counts per cell. Alignment was performed using the hg19 reference genome build, coupled with the Ensembl transcriptome (v75). For snRNaseq data, intronic counts were included. For each sample, cells were filtered using the following quality control (QC) metrics (Table S6): mitochondrial content (indicative of cell damage), number of genes, and number of unique molecular identifiers (UMIs), using the Seurat (Butler et al., 2018) package (v2.3). Thresholds for each sample were selected according to the distribution of each metric within the sample, which varies with sequencing coverage and the number of cells captured. Data was processed as described previously (Jessa et al., 2019) using Seurat. Briefly, libraries were scaled to 10,000 UMIs per cell and log-normalized. UMI counts and mitochondrial content were regressed from normalized gene counts and the residuals z-scored gene-wise. Dimensionality reduction was performed using principal component analysis (PCA) applied to the most variant genes, and PCA was used as input for projection to two dimensions using uniform manifold approximation and projection (McInnes et al., 2018) (UMAP) and clustering using a shared nearest neighbor modularity optimization algorithm (Waltman and Van Eck, 2013).

Integration of scRNaseq and snRNaseq data

For visualization of single-cell (scRNaseq) and single-nuclei (snRNaseq) datasets in a shared UMAP space as in Figure 5, cells from all G34R/V tumor datasets were integrated using the method implemented in Seurat (Stuart et al., 2019) (v3). The resulting matrix was subjected to z-scoring and dimensionality reduction as described above. Only cells identified as malignant (see below) were included in this visualization.

Projection of cells to a brain reference atlas

Cell type assignment for each cell was based on projection to the most similar cell type in the normal developing brain, with cell type signatures obtained from the mouse brain scRNaseq atlas (Jessa et al., 2019), using three different cell type projection methods, detailed below: (*i*) ACTINN (Ma and Pellegrini, 2020), (*ii*) pattern correlation, and (*iii*) random sampling (Filbin et al., 2018)). Signatures derived from proliferating clusters were excluded from analysis, resulting in 176 gene signatures. Each tumor cell was assigned a cell identity based on the majority vote of the three projection methods. For cells without a majority assignment, the cell identity was imputed based on the assigned cell type for the majority of the ten nearest neighbors obtained using the shared nearest neighbor (Waltman and Van Eck, 2013) method implemented in Seurat.

Neural network ACTINN projection

A neural network with three hidden layers (Ma and Pellegrini, 2020) designed for assigning cell type in scRNaseq data was trained on single-cell gene expression profiles from the mouse scRNaseq reference atlas. In the reference, the training data was the normalized single-cell gene expression profiles for the 1000 most variable genes, and the training labels were the cell types assigned to each individual cell. The trained neural network was applied to normalized single cell gene expression data for tumor samples.

Pattern correlation projection

We adapted a method developed for cell cycle phase assignment in scRNaseq data (Macosko et al., 2015) to cell type projection. Given our set of 176 signatures, $S = \{s_1, s_2, \ldots, s_{176}\}$ where $s_i = \{gene_1, gene_2, gene_3, \ldots, gene_{100}\}$, we compute, for each signature s_i and for each cell c_j, the average normalized expression of all the genes in s_i, defining a score $T_{s_i c_j}$. The scores $T_{s_i c_j}$ are z-scored across cells to yield normalized scores $N_{s_i c_j}$. Finally, for each cell, the scores $N_{s_i c_j}$ are z-scored across signatures to obtain a final score $F_{s_i c_j}$. In the reference atlas, each cluster of cells has a gene signature. Many clusters in the atlas are composed of cell types identified at multiple brain regions or time points (e.g., astrocyte clusters were identified in both brain regions sampled). We therefore define ''cell type identity'' vectors, representing the 37 distinct cell types captured. Each cell type identity vector is a binary vector of the same length as the signature set S, which takes on a value of 1 if the corresponding signature belongs to the given cell type, and 0 otherwise. We then compute, for each cell, the correlation between the final scores $F_{c_i s_k}$ and each of the cell type identity vectors. Finally, each cell is assigned the identity of the cell type with the greatest correlation.

Random sampling projection

We compute a score $T_{s_i c_j}$ for each cell as described above. For each signature, this score is compared to the score for a control gene set, computed in an identical manner. To define the control gene set, all detected genes are first binned based on their average expression across the dataset. The control gene set is generated by randomly sampling with replacement 100 genes of similar expression level for each gene in the signature. The final score for each signature is the difference between the score $T_{s_i c_j}$ and the score of the control set. Finally, each cell is assigned the identity of signature with the highest final score.

Re-analysis of published data

Normalized expression levels for scRNaseq (Smartseq2) datasets of other HGG entities from published studies were downloaded from GEO: IDH1 mutant HGG (Venteicher et al., 2017) (GSE89567), K27M HGG (Venteicher et al., 2017) (GSE102130) and WT HGG (Neftel et al., 2019) (GSM3828672). In the latter case, pediatric and adult samples were separated. For each dataset, normalized expression levels were subjected to z-scoring, dimensionality reduction, clustering and cell type projection as described above. Clusters of cells projected to immune cell types were flagged as normal.

Identification of normal and malignant cells

Malignant cells within a sample were identified as follows. First, cells from all samples, separately from each technology (scRNaseq and snRNaseq) were pooled and subjected to scaling, dimensionality reduction, cell projection and clustering as described above. Clusters composed of cells projecting to a single cell type and originating from multiple patients were labeled as normal. Specifically, we identified normal clusters as those for which a single patient accounted for at most 75% of the cells/nuclei in the cluster, and for which at least 70% of all the cells/nuclei in the cluster projected to the same cell type. Clusters of cells originating from multiple patients but projecting to different cell types were flagged as low quality and removed from the analysis. Next, copy number alterations (CNV) were inferred on a per sample basis as previously described (Filbin et al., 2018). For this, the cells labeled as normal as described above were used as reference. In some samples, a clear CNV distinction between normal and malignant cells was not present. In these cases, we identified groups of cells which, (1) clustered together based on transcriptional profiles and (2) were assigned the same cell type based on projections to the reference atlas and (3) no obvious CNV alteration was observed. The cells fulfilling all three criteria were then labeled as normal. Finally, independent CNV calls were obtained with the inferCNV package (v0.8.2) (Tickle et al., 2020) on a per sample basis, using cells labeled as normal pooled from all samples as a combined normal reference, in order to confirm aberrant CNV profiles in malignant cells.

Supplemental Figures

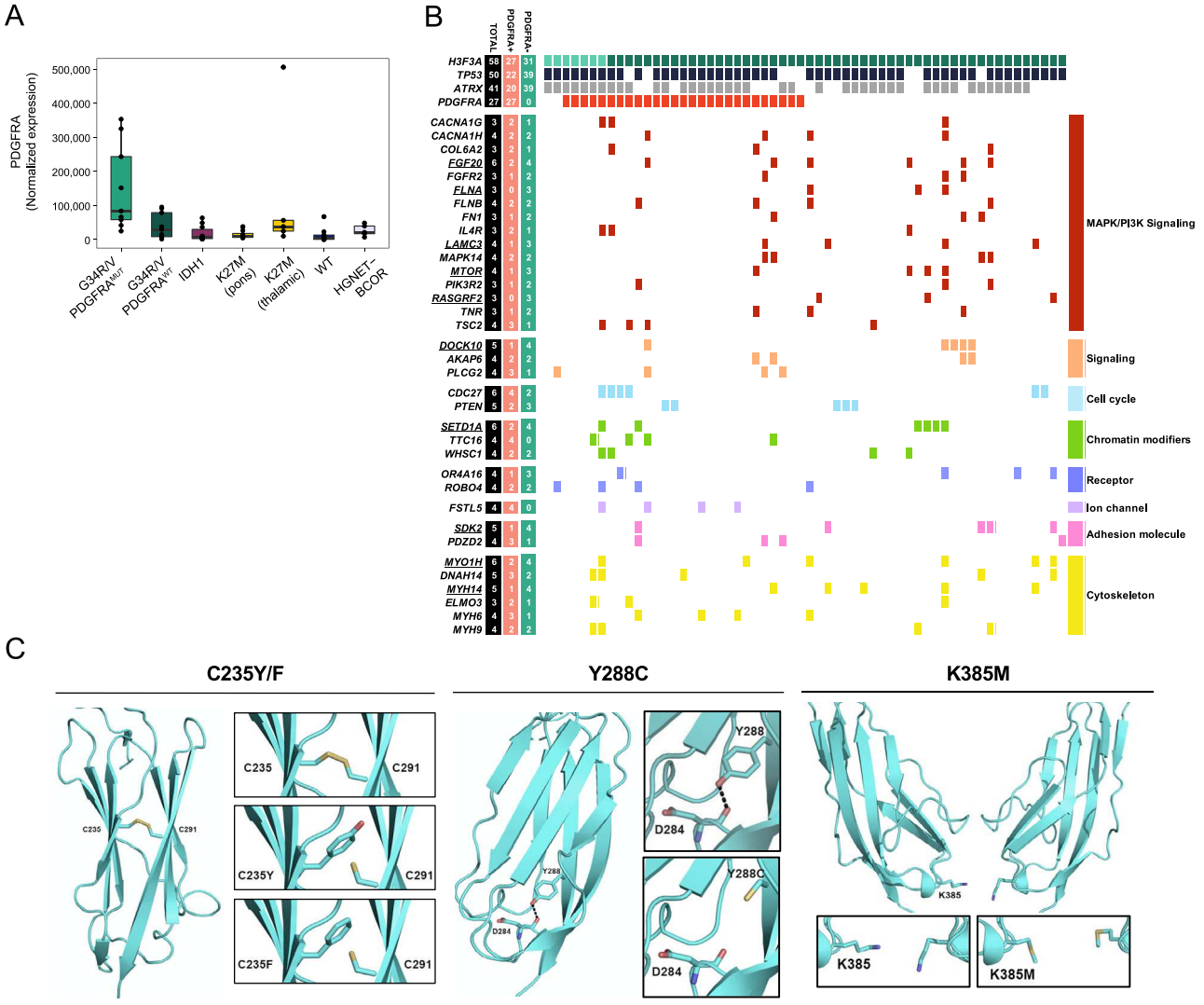

Figure S1. Recurrent Somatic Mutations in G34R/V HGGs, Related to Figure 1

A. Expression of PDGFRA in HGGs. PDGFRA is significantly upregulated in G34R/V tumors relative to others (*adjusted p value = 0.018, Negative Binomial Wald test*). B. Oncoprint depicting recurrently mutated genes (observed in > 3 patients) in G34R/V HGG, grouped by associated gene functions as determined by Gene Ontology. Columns adjacent to gene names represent the number of patients in which mutations were called, in the entire cohort or stratified by *PDGFRA* mutation status (red = $PDGFRA^{MUT}$, green = $PDGFRA^{WT}$). Underlined genes indicate a bias toward $PDGFRA^{WT}$ G34 samples. C. Complex structure diagrams depicting extracellular PDGFRA mutations C235Y/F, Y288C, and K385M. Crystal structures of PDGFRB (PDB: 3MJG) were used to model C235 and Y288 mutations, and VGFR1 (PDB: 5T89) for K385. The C235Y/F mutations destabilize the Ig-like domain, leaving C291 available to form another inter- or intra-molecular disulfide bond, potentially leading to receptor dimerization and activation, analogous to Y288C. Finally, for K385M, in the wild-type protein, the positive charges of two K385 residues at the dimerization interface create an unfavorable repulsive effect. The K385M mutation may promote a small hydrophobic patch adjacent to several salt-bridges, enhancing receptor dimer formation and activation.

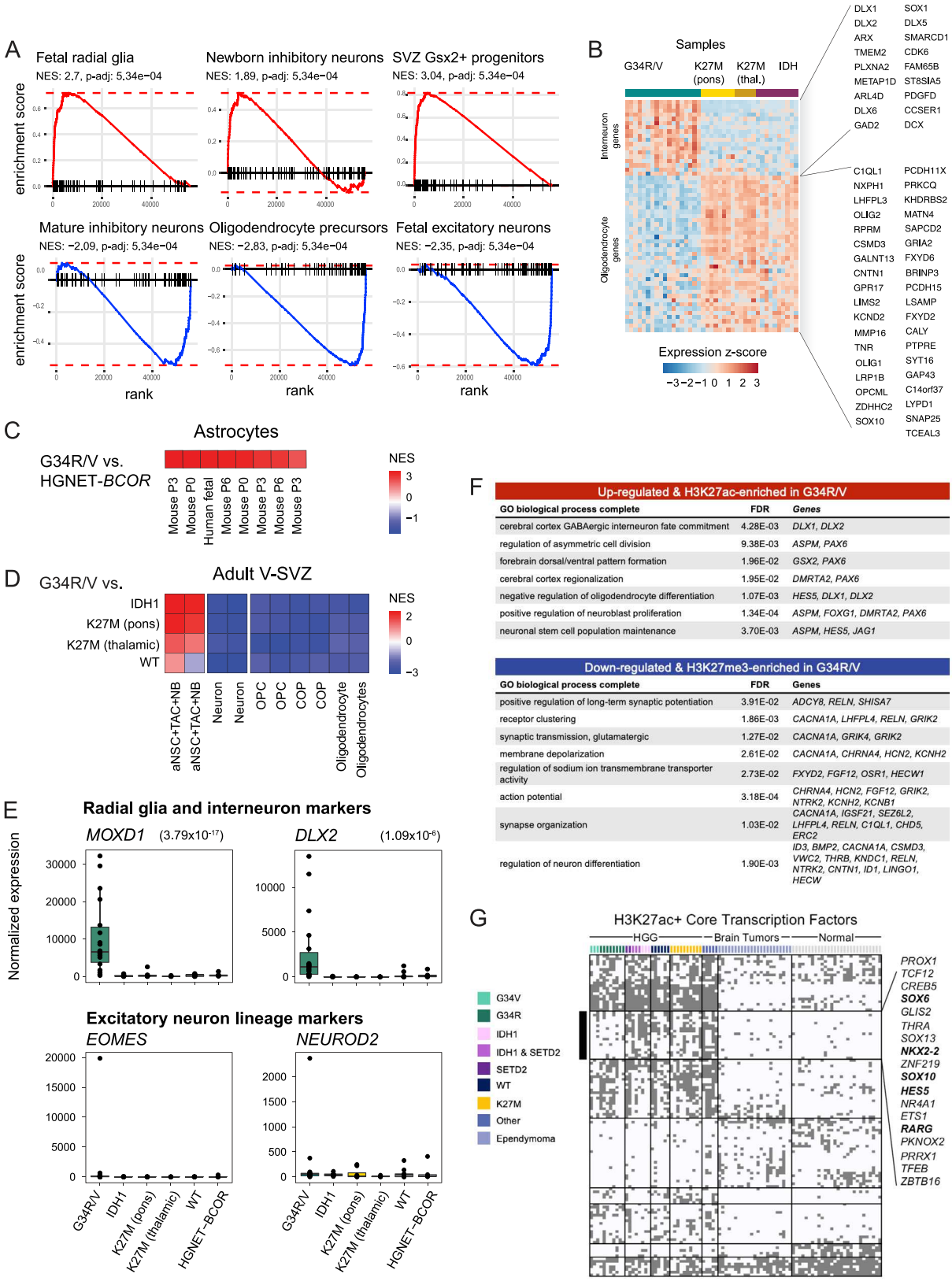

(legend on next page)

Figure S2. G34R/V Uniquely Exhibits a Transcriptome and Epigenome Program Specific to the Forebrain Interneuron Lineage, Related to Figure 2 and Tables S2 and S3

A. Gene set enrichment analysis (GSEA) plots for the most enriched or depleted signature of each cell type. Enrichments are computed for G34R/V compared to IDH1 HGGs. NES: normalized enrichment score. B. Heatmap of expression levels of genes driving the enrichment of interneuron gene signature, or the depletion of the oligodendrocyte signature, in G34R/V tumors compared to other HGG subgroups. Expression is z-scored across samples. C. Heatmap of GSEA NES scores of forebrain astrocyte signatures in G34R/V tumors compared to the HGNET-BCOR tumors (non-gliomas). D. Heatmap of GSEA NES scores of 8-10 week old mouse ventricular/sub-ventricular zone (V-SVZ) cell type signatures in G34R/V compared to IDH1, K27M and WT HGG subgroups, as in (A). Scores are shown for all signatures significantly enriched (*adjusted p value < 0.01*) in G34R/V versus IDH1. aNSC: actively dividing neural stem cells, TAC: transit amplifying cells, NB: neuroblasts, OPC: oligodendrocyte progenitor cells, COP: committed oligodendrocyte precursors. E. Expression levels of the human radial glia marker *MOXD1* and markers for cortical inhibitory and excitatory neurons in G34R/V, other HGG subgroups, and HGNET-BCOR. For genes upregulated in G34R/V, adjusted p values (Negative Binomial Wald test) for comparison of G34R/V to other entities are indicated in parentheses. F. Gene ontology analysis of differentially expressed genes that showed significant H3K27ac or H3K27me3 enrichment in G34R/V tumors (z-score > 0.5). G. Core transcription factors (inferred by H3K27ac enrichment) activated in G34R/V compared to other HGGs, non-glioma brain tumors, and normal brain. Indicated TFs from cluster 2 lack activation signals specifically in G34R/V HGGs. Bolded genes indicate transcription factors annotated as necessary for oligodendrocyte differentiation (*FDR = 0.0001*) based on Gene ontology enrichment analysis.

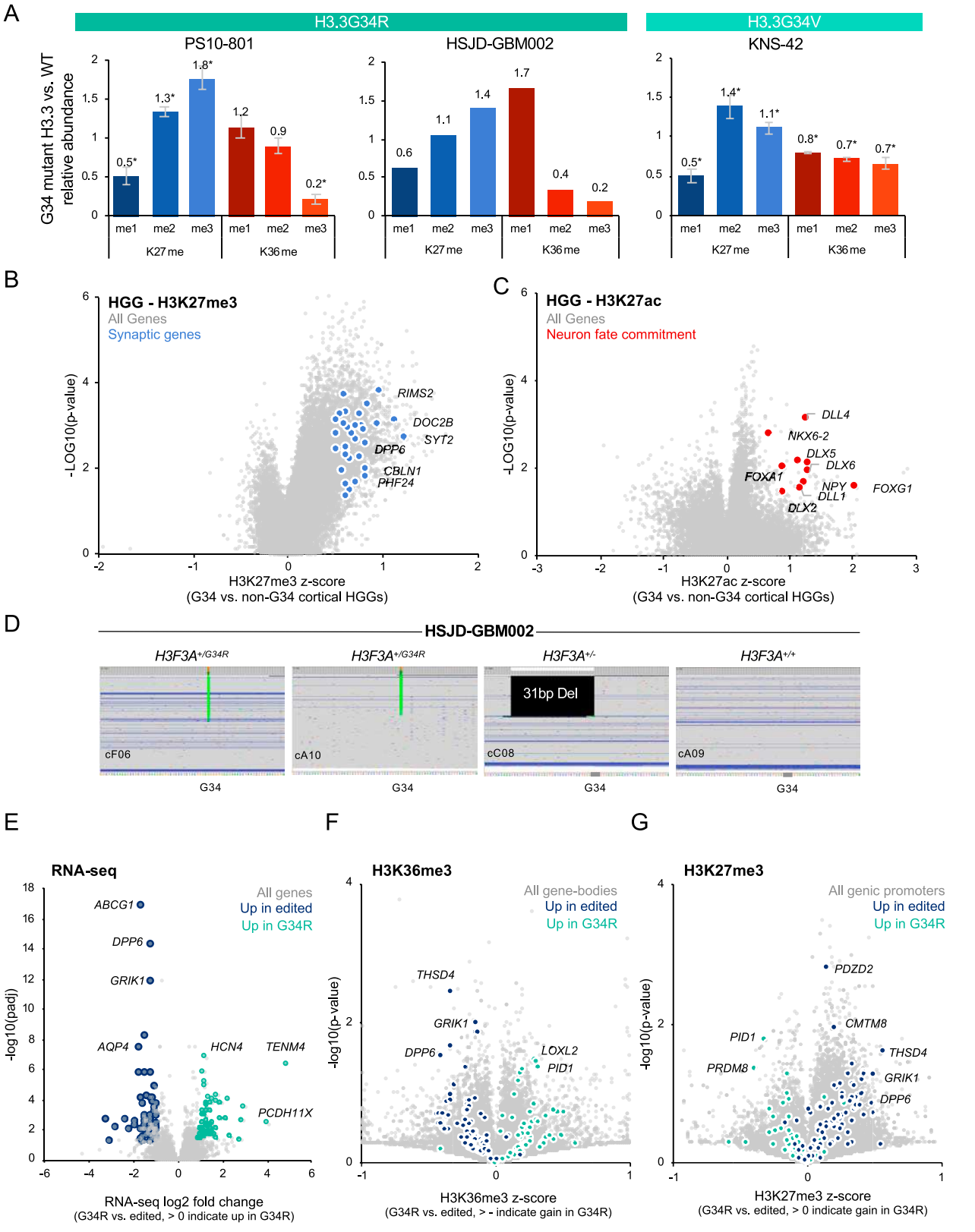

(legend on next page)

Figure S3. G34R/V Promotes Aberrant H3K27me3 Retention at Terminal Neuronal Genes, Related to Figure 3 and Tables S2 and S3

A. Quantification of H3K27 and H3K36 methylation states by histone mass spectrometry on the mutant H3.3G34R or H3.3G34V histone normalized by H3.3 WT abundance in PS10-801 (left, n = 3), HSJD-GBM002 (middle, n = 1) or KNS-42 (right, n = 6) cell lines respectively. * denotes p value < 0.05 (paired t test). B. Volcano plot depicting differential H3K27me3 enrichment between G34R/V and non-G34R/V cortical HGGs at all annotated promoters. Blue data points indicate G34R/V-specific H3K27me3+ genes (*z-score > 0.5, p value < 0.05*) involved in spontaneous synaptic transmission (*FDR = 0.0273*), calcium ion-regulated exocytosis of neurotransmitter (*FDR = 0.000269*), and regulation of GABAergic synaptic transmission (*FDR = 0.00332*). C. Volcano plot depicting differential H3K27ac enrichment between G34R/V and non-G34R/V cortical HGGs at all annotated promoters. Red data points indicate G34R/V-specific H3K27ac+ genes (*z-score > 0.5, p value < 0.05*) involved in neuron fate commitment (*FDR = 0.00243*). D. Targeted deep sequencing validation of CRISPR-mediated editing of *H3F3A* G34R in HSJD-GBM002 clones. E. Volcano plot depicting transcriptomic change in CRISPR HSJD-GBM002 clones. Genes significantly upregulated (log2FC > 1, p-adj < 0.05) in G34R unedited clones are highlighted in teal, whereas genes significantly upregulated upon G34R removal are highlighted in navy (log2FC > 1, p-adj < 0.05). F. Volcano plot depicting H3K36me3 change at all annotated genic promoters in CRISPR HSJD-GBM002 clones (gray points), highlighting differentially expressed genes from RNA-seq (from panel E, teal = upregulated in G34R, navy = upregulated in edited). G. Volcano plot depicting H3K27me3 change at all annotated genic promoters in CRISPR HSJD-GBM002 clones (gray points), highlighting differentially expressed genes from RNA-seq (from panel E, teal = upregulated in G34R, navy = upregulated in edited).

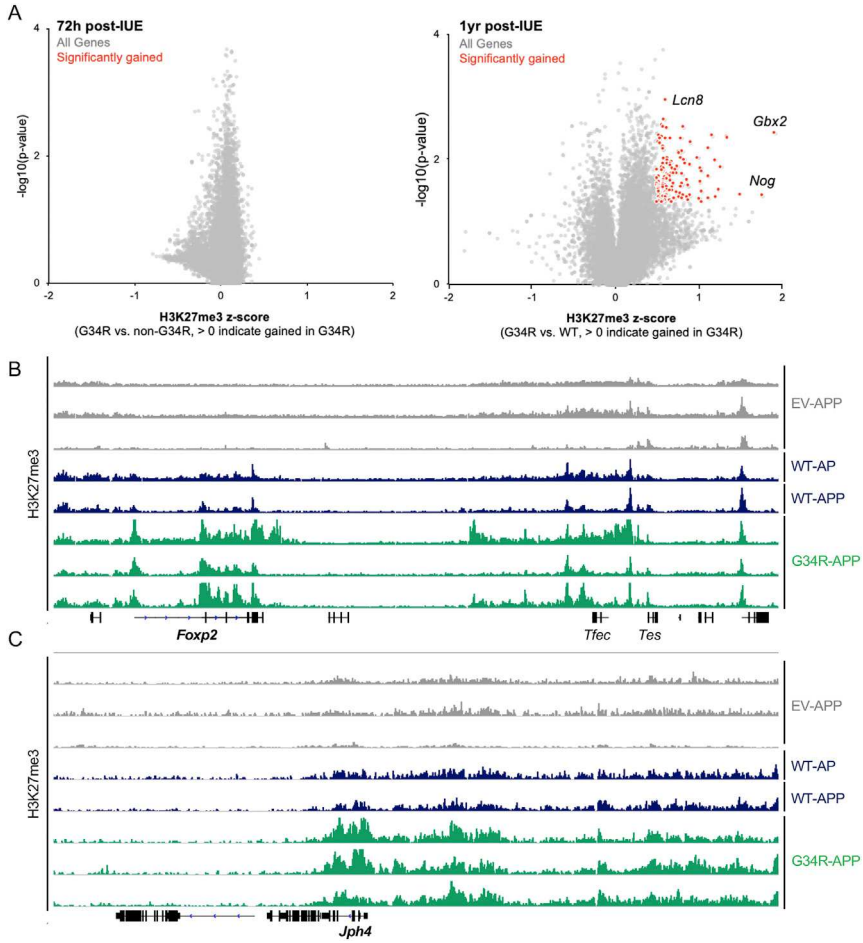

Figure S4. Introduction of G34R in Murine Embryonic Forebrain Induces H3K27me3 Epigenomic Reprogramming, Related to Figure 3

A. Volcano plot depicting differential promoter H3K27me3 enrichment between G34R and non-G34R sorted cells 72-hours post-electroporation (left) or > 1-year post-electroporation (right). Genic promoters with significantly increased H3K27me3 enrichment in G34R cells are indicated in red. B-C. Genome browser snapshot of ChIP-seq profiles in IUE-derived neural precursor cells showing H3K27me3 profiles associated with G34R-introduction. Some genic promoters, such as *Foxp2* (B) and *Jph4* (C) show striking H3K27me3 enrichment uniquely in G34R-electroporated cells. EV: empty vector. WT: wild-type H3.3. APP: *Atrx* shRNA, sgRNA for *Trp53*, *PDGFRA*^{WT}. AP: *Atrx* shRNA, sgRNA for *Trp53*.

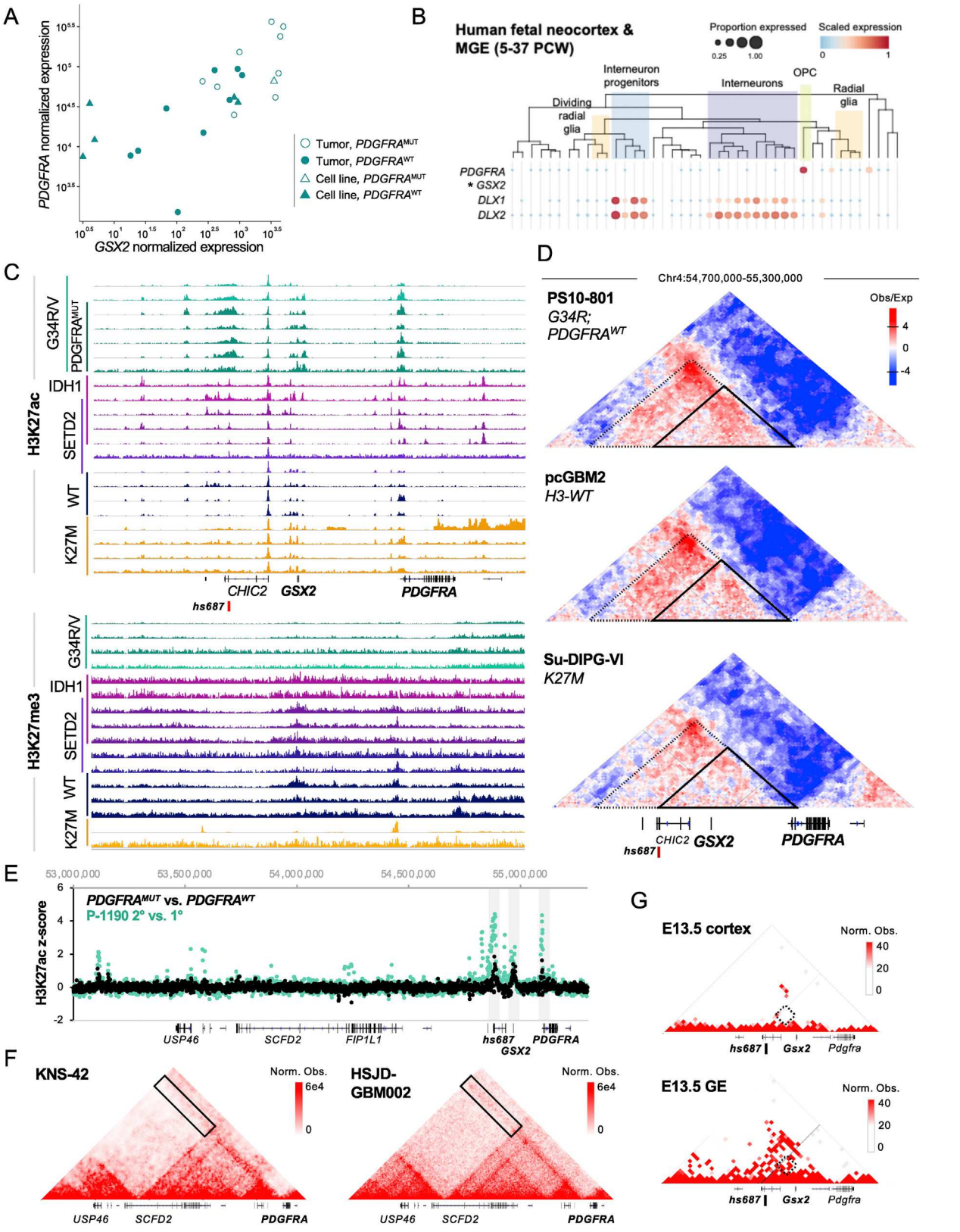

(legend on next page)

Figure S5. Active Chromatin Conformation Promotes *GSX2-PDGFRA* Co-expression in G34R/V HGGs, Related to Figure 4 and Table S4

A. Normalized expression of *PDGFRA* and *GSX2* in bulk RNA-seq of G34R/V tumors (circles) and cell lines (triangles). *Pearson correlation = 0.69, R^2 = 0.48, p value = 0.0002*. B. *PDGFRA, GSX2,* and *DLX1/2* expression in cell populations from scRNaseq atlas of the developing (5-37 PCW) human telencephalon. For each cell population (tree leaves), mean expression and proportion of cells expressing the gene are indicated. Dendrograms were constructed based on pairwise Spearman correlations of gene expression. MGE: medial ganglionic eminence, OPC: oligodendrocyte progenitor cells. *: *GSX2* is not detected in this dataset due to low coverage. C. Top, H3K27ac profiles at the *PDGFRA-GSX2-hs687* locus in individual G34R/V (n = 7), IDH1 (n = 5), SETD2 (n = 5), WT (n = 3), and K27M (n = 4) tumors. $PDGFRA^{MUT}$ samples are distinguished by darker teal. Note that *PDGFRA* is amplified in one K27M sample (first yellow track). Bottom, H3K27me3 profiles at the *PDGFRA-GSX2* locus in individual G34R/V tumors (n = 5), IDH1 (n = 5), SETD2 (n = 5), WT (n = 3), and K27M (n = 2) tumors. D. Hi-C heatmaps from a G34R, H3/IDH WT and K27M glioma cell lines depicting sub-TAD structure at the *PDGFRA-GSX2-hs687* locus. Small black triangle illustrates a TAD between *PDGFRA* and *hs687* enriched for contacts in G34R/V lines. Large dashed triangle demarcates the TAD formed by contact to a known distal insulator. Heatmap represents the log2 ratios of observed interactions relative to expected interactions across the *PDGFRA-hs687* locus at a 5kb resolution (red = positive, blue = negative). E. Manhattan plot depicting H3K27ac enhancer activation difference between $PDGFRA^{MUT}$ *and* $PDGFRA^{WT}$ G34R/V HGGs (z-score > 0 indicate H3K27ac enriched in $PDGFRA^{MUT}$) at far distal regions of *PDGFRA-GSX2* locus. Black points depict comparison across different patients (n = 5 $PDGFRA^{MUT}$ and n = 2 $PDGFRA^{WT}$), and teal points depict recurrence ($PDGFRA^{MUT}$) versus primary ($PDGFRA^{WT}$) comparison in the same patient P-1190. F. Hi-C heatmaps from two G34R/V cell lines, HSJD-GBM002 ($PDGFRA^{MUT}$) and KNS-42 ($PDGFRA^{WT}$), depicting TAD structure at the *PDGFRA-GSX2-hs687* locus. Black rectangles illustrate long-distance interactions between *PDGFRA* promoter and potential enhancers, enriched for contacts in HSJD-GBM002 versus KNS-42. Heatmap represents the normalized observed interactions across the locus at a 5kb resolution (red = high interaction, white = low interaction). G. Hi-C heatmaps from murine E13.5 cortex and ganglionic eminences (GE) depicting sub-TAD structure at the *Pdgfra-Gsx2-hs687* locus. The dashed square represents the interaction between *GSX2* promoter and *hs687*. Heatmap represents the normalized observed interactions across the locus at a 10kb resolution (red = high interaction, white = low interaction).

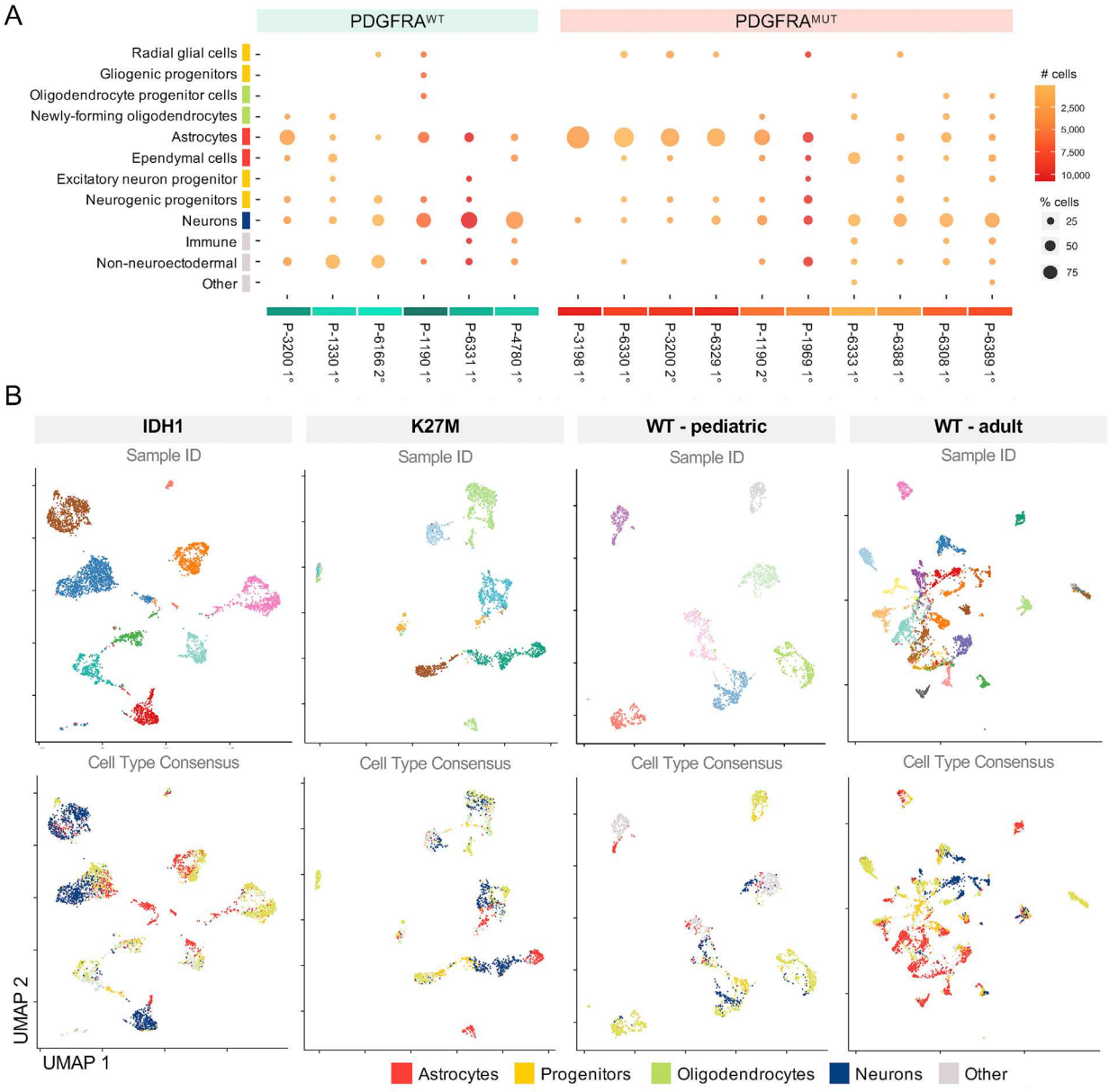

(legend on next page)

Figure S6. G34 HGGs Are Devoid of the Oligodendroglial Lineage, and Co-option of *PDGFRA*^{MUT} Promotes Neuronal-to-Astrocytic Transition, Related to Figure 5 and Table S5

A. Bubble plot representing the composition of cell types in each tumor. Circle size represents the proportion of each cell type per tumor, and circle color represents the total number of malignant cells within the tumor. B. UMAP embedding of IDH1, K27M, H3/IDH1-WT HGG (pediatric and adult) scRNA-seq datasets, color coded by patient of origin (top) and cell type projection (bottom). Oligodendrocytes (in green) are clearly detected in all non G34R/V HGG entities. C. Mean expression of fetal interneuron and astrocyte gene signatures in individual cells from the normal human telencephalon. Cells of the interneuron lineage, as well as radial glial cells and astrocytes were included.

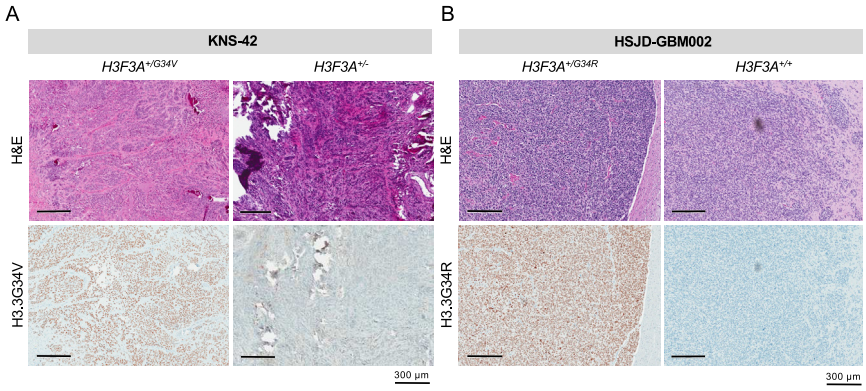

Figure S7. G34R/V Mutations Are Dispensable for Tumor Maintenance, Related to Figure 6

A. Hematoxylin & eosin (H&E) and immunohistochemical analysis of representative KNS-42 parental and edited clone-derived PDOX tumors using a G34V-specific antibody. B. H&E and immunohistochemical analysis of representative HSJD-GBM002 parental and edited clone-derived PDOX tumors using a G34R-specific antibody.

Příloha 2

Trkova K, Sumerauer D, Krskova L, Vicha A, Koblizek M, Votava T, Priban V, Zapotocky M. DIPG-like MYB-altered diffuse astrocytoma with durable response to intensive chemotherapy. ***Childs Nerv Syst.*** 2023 Sep;39(9):2509-2513. doi: 10.1007/s00381-023-05976-3. Epub 2023 May 11. PMID: 37165121; PMCID: PMC10432314 **[IF 1.39]**

Autorský podíl: Genetické a epigenetické testování – Sangerovo sekvenování, methylační array, NGS, analýza molekulárních a klinických dat, příprava publikace a revizí publikace.

Child's Nervous System (2023) 39:2509–2513
https://doi.org/10.1007/s00381-023-05976-3

CASE REPORT

DIPG-like MYB-altered diffuse astrocytoma with durable response to intensive chemotherapy

Katerina Trkova[1,2,3] · David Sumerauer[1,2,3] · Lenka Krskova[1,2,4] · Ales Vicha[1,2,3] · Miroslav Koblizek[1,2,4] · Tomas Votava[5] · Vladimir Priban[6] · Michal Zapotocky[1,2,3]

Received: 28 February 2023 / Accepted: 29 April 2023 / Published online: 11 May 2023

Abstract

Pontine gliomas represent difficult to treat entity due to the location and heterogeneous biology varying from indolent low-grade gliomas to aggressive diffuse intrinsic pontine glioma (DIPG). Making the correct tumor diagnosis in the pontine location is thus critical. Here, we report a case study of a 14-month-old patient initially diagnosed as histone H3 wild-type DIPG. Due to the low age of the patient, the MRI appearance of DIPG, and anaplastic astrocytoma histology, intensive chemotherapy based on the HIT-SKK protocol with vinblastine maintenance chemotherapy was administered. Rapid clinical improvement and radiological regression of the tumor were observed with nearly complete remission with durable effect and excellent clinical condition more than 6.5 years after diagnosis. Based on this unexpected therapeutic outcome, genome-wide DNA methylation array was employed and the sample was classified into the methylation class "Low-grade glioma, MYB(L1) altered." Additionally, RT-PCR revealed the presence of *MYB::QKI* fusion. Taken together, the histopathological classification, molecular-genetic and epigenetic features, clinical behavior, and pontine location have led us to reclassify the tumor as a pontine MYB-altered glioma. Our case demonstrates that more intensive chemotherapy can achieve long-term clinical effect in the treatment of MYB-altered pontine gliomas compared to previously used LGG-based regimens or radiotherapy. It also emphasizes the importance of a biopsy and a thorough molecular investigation of pontine lesions.

Keywords MYB-altered glioma · MYB::QKI fusion · Pediatric pontine glioma · DIPG · Chemotherapy

Introduction

Pediatric pontine gliomas represent the most challenging diagnosis in pediatric oncology due to the location and heterogeneous biology varying from indolent low-grade gliomas to aggressive diffuse intrinsic pontine glioma (DIPG) [1, 2]. DIPG is one of the deadliest tumors of childhood with a lack of curative treatment options. The majority of these tumors harbor mutations in histone H3 and are hence classified as diffuse midline gliomas H3 K27-altered. Only anecdotal cases with long-term survival have been reported so far. Making the correct tumor diagnosis in the pontine location is thus critical. Nevertheless, the majority of international institutions initiate palliative focal radiation therapy based on clinical symptoms and MRI characteristics without previous biopsy.

Here, we describe a unique case of a very young child with histone H3 wild-type DIPG that was later characterized by the presence of MYB::QKI fusion treated with radiation sparing approach.

✉ Michal Zapotocky
michal.zapotocky@fnmotol.cz

1 Prague Brain Tumor Research Group, Second Faculty of Medicine, Charles University and University Hospital Motol, V Uvalu 84, 15006 Prague 5, Czech Republic

2 Pediatric Neurooncology Centre, University Hospital Motol, V Uvalu 84, 15006 Prague 5, Czech Republic

3 Department of Pediatric Hematology and Oncology, Second Faculty of Medicine, Charles University Prague and University Hospital Motol, V Uvalu 84, 15006 Prague 5, Czech Republic

4 Department of Pathology and Molecular Medicine, Second Faculty of Medicine, Charles University Prague and University Hospital Motol, V Uvalu 84, 15006 Prague 5, Czech Republic

5 Department of Pediatrics, University Hospital in Pilsen, Alej Svobody 80, Pilsen-Lochotin 323 00, Czech Republic

6 Department of Neurosurgery, University Hospital in Pilsen, Alej Svobody 80, Pilsen-Lochotin 323 00, Czech Republic

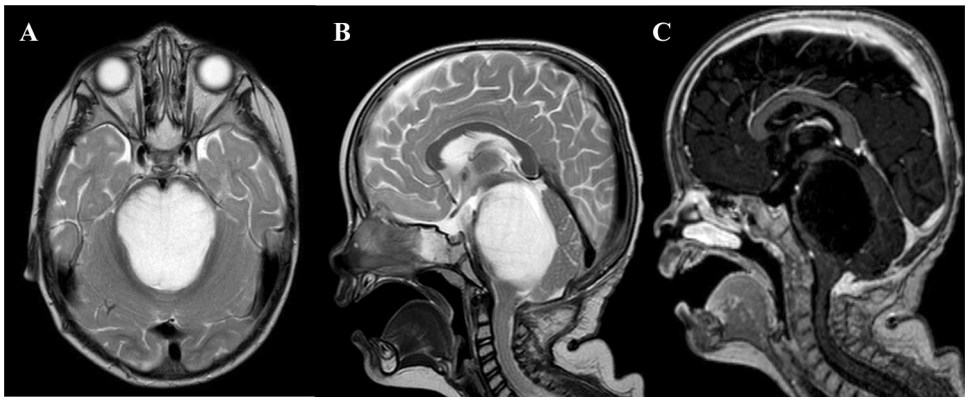

Fig. 1 Diagnostic MRI of large pontine tumor. **A** T2-weighted axial images demonstrating pons involvement (over 66% of the diameter). **B** T2 sagittal sequence. **C** T1 sagittal after gadolinium administration displaying hypointense contrast non-enhancing tumor

Case presentation

At the time of diagnosis in 2016, a 14-month-old previously healthy boy presented with a 2-month history of cranial nerve palsies (n. VI and n. VII in the left side) and progressive psychomotor regression. Brain MRI revealed a T2/FLAIR hyperintense, T1 hypointense, non-enhancing extensive intraaxial posterior fossa mass centered in the pons and causing hydrocephalus. Based on MRI and clinical characteristics, the diagnosis was consistent with DIPG; however, the age at presentation was rather atypical (Fig. 1A–C). A posterior fossa craniotomy with a tumor biopsy was

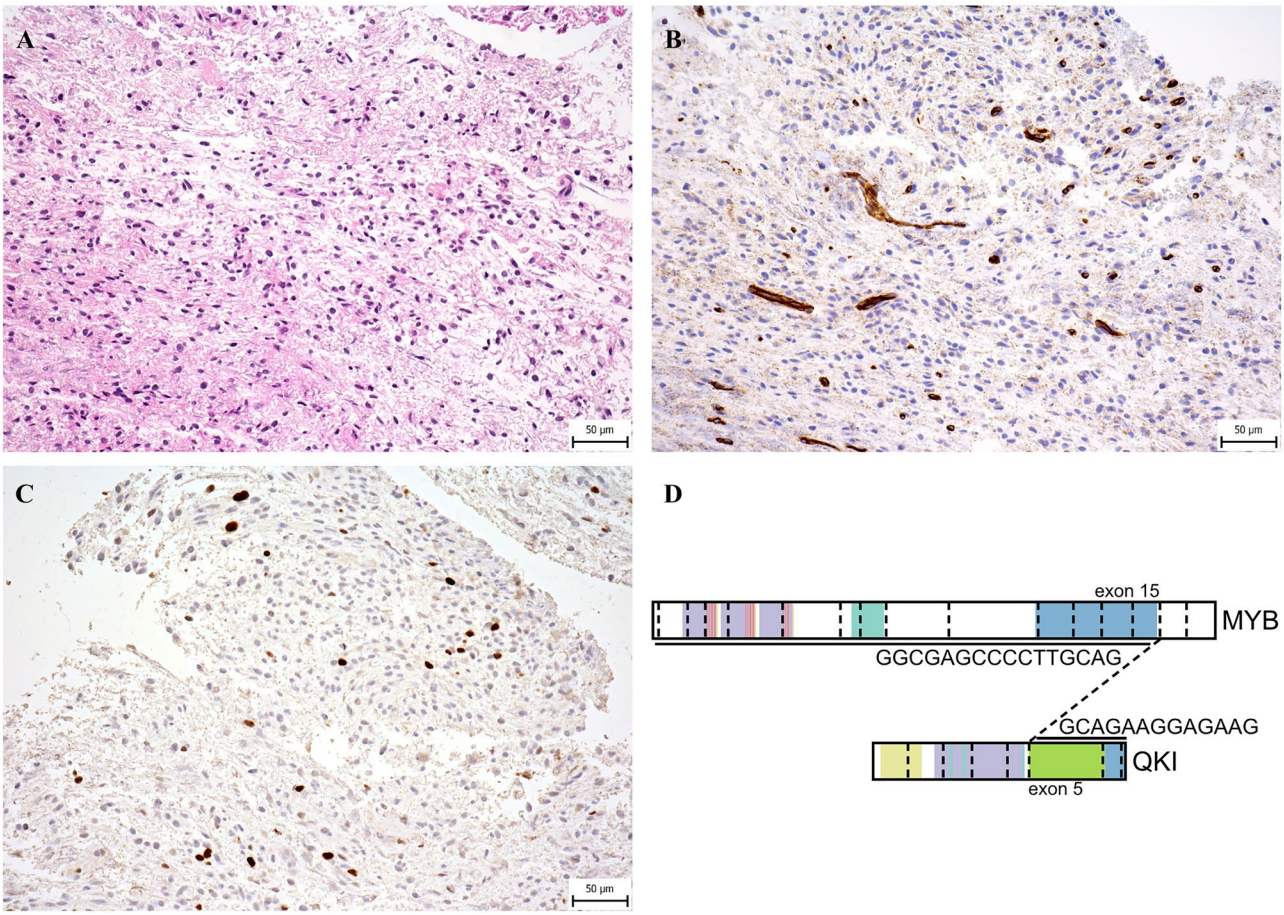

Fig. 2 Photomicrographs of the representative tumor sections. **A** Hematoxylin and eosin–stained slide shows moderately cellular glioma with mild cytological atypia and with no obvious growth pattern. **B** Immunohistochemical staining for CD34 is negative in tumor cells and positive in endothelial cells. It highlights the absence of perivascular growth pattern. **C** Proliferative activity of tumor cells shown by Ki-67 positivity is mildly increased (generally with relatively low positivity (up to 5%), but in several hotspots clearly increased (about 10%). **D** Schematic display of *MYB::QKI* fusion transcript

performed. Histopathological examination revealed a moderately cellular tumor composed of medium-sized multipolar or elongated glial fibrillary acidic protein (GFAP)–positive astrocytes with projections creating a fibrillar background. A pathologist classified this tumor as anaplastic astrocytoma grade 3 as per the 3rd version of the WHO Classification of Central Nervous Tumors from 2007 (Fig. 2A–C) [3]. Direct sequencing of the tumor tissue sample was performed at the time of diagnosis using primers described elsewhere, and neither mutations exon 15 of *BRAF* gene nor histone 3 (*H3F3A*, *HIST3B1*) was present [4, 5]. Reverse transcription PCR (RT-PCR) did not reveal any variant of the *KIAA1549::BRAF* fusion [6].

Due to the child's age and better outcome of DIPG in young children (less than 3 years old) [7], intensive chemotherapy was initiated according to the German HIT-SKK-based regimen for infant high-grade glioma, consisting of 39 weeks of alternating cycles of vincristine plus cyclophosphamide, high-dose methotrexate, and carboplatin plus etoposide [8, 9]. Rapid clinical improvement followed by significant radiological partial tumor regression (> 50%) was achieved after 6 months (Fig. 3A, B). After completion of intensive chemotherapy, the patient continued with maintenance vinblastine monotherapy at a dose of 6 mg/m^2 for a total duration of 70 weeks. Vinblastine was reduced to 5 mg/m^2 due to hematological toxicity. At the end of the treatment, the MRI showed almost complete regression of the disease (Fig. 3C). Our patient is currently more than 6.5 years after the diagnosis with insignificant residual changes (T2-weighted images) in the pons (Fig. 3D). Clinically, he is in excellent condition without neurological deficits, living the life of a healthy child.

This favorable treatment response to chemotherapy alone and sustained durable remission were highly unlikely to occur in DIPG. Therefore, molecular analysis was expanded to evaluate true tumor biology and uncover underlying genetic aberrations. Genome-wide DNA methylation array was performed, and the sample was classified using the v12.5 version of the Heidelberg classifier into the methylation class "Low-grade glioma, MYB(L1) altered" with a calibrated score of 0.90 [10]. Consequently, we performed RT-PCR, which revealed the presence of *MYB::QKI* fusion (*ex15::ex5*) as

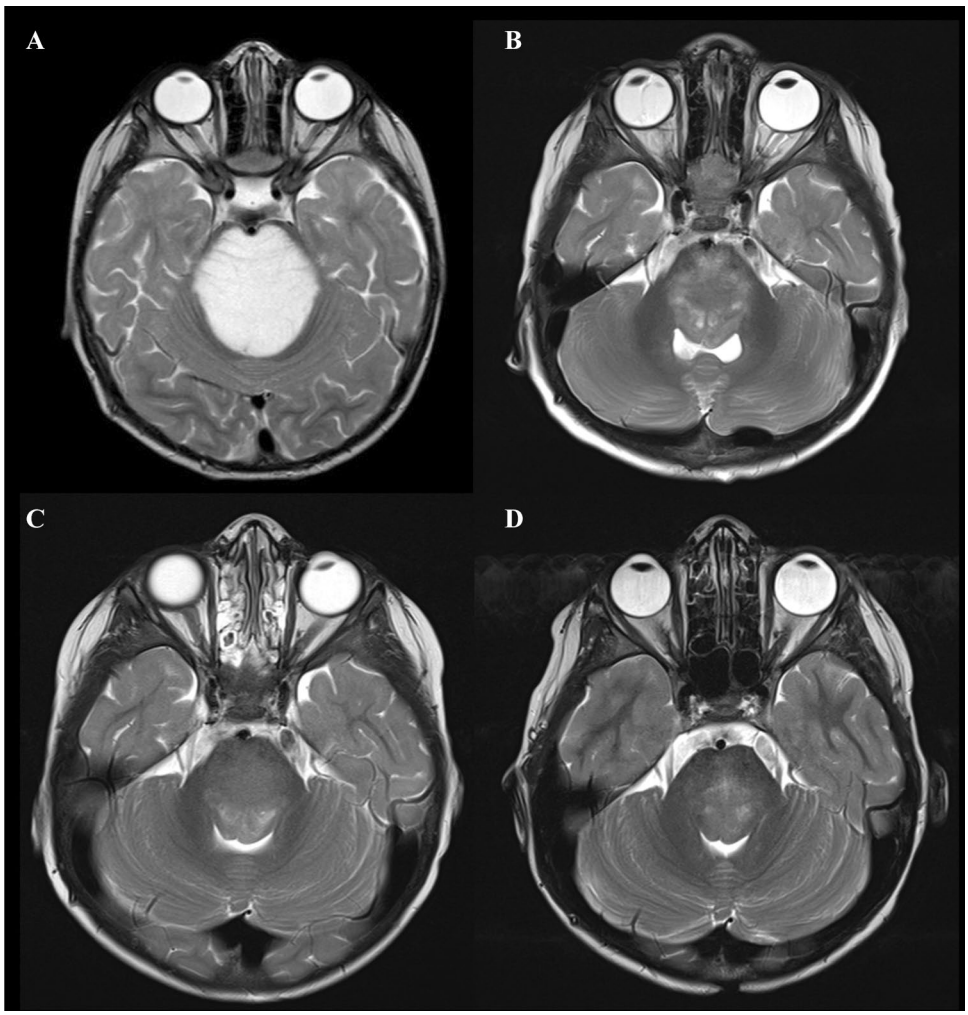

Fig. 3 MRI demonstrating response to the therapy using T2-weighted axial images. **A** Tumor extent at the time of diagnosis. **B** Partial regression of the tumor during intensive chemotherapy (after 6 months). **C** At the end of intensive treatment and **D** continuous remission after 6.5 years from diagnosis

displayed in Fig. 2D [11]. Taken together, the histopathological classification, molecular-genetic and epigenetic features, clinical behavior, and pontine location have led us to reclassify the tumor as a pontine MYB-altered glioma.

Discussion and conclusion

According to the fifth edition of the WHO Classification of Central Nervous System Tumors from 2021, pediatric MYB-altered gliomas are split into two main groups: "Diffuse astrocytoma, MYB- or MYBL1-altered" and "Angiocentric glioma" [12]. Both tumor types are predominantly localized in the cerebral cortex [13, 14] and are associated with epilepsy, and their resection usually has curative potential [15]. Genetically, they are characterized by the presence of the *MYB* alteration; angiocentric gliomas mostly by *MYB::QKI* gene fusion; in contrast, *PCDHGA1*, *MMP16*, and *MAML* are reported fusion partner genes of *MYB/MYBL1* in diffuse astrocytomas [13].

However, only a few cases of angiocentric gliomas localized in the pons with a proven gene fusion *MYB::QKI* have been described in the literature so far [13, 16, 17]. Therapeutic LGG-based regimens used for these cases included vincristine plus carboplatin, bevacizumab, or mTOR inhibitor everolimus [16, 17]. The combined chemotherapy did not lead to a sufficient therapeutic response; only the addition of mTOR inhibitor in one patient provided stabilization of the disease [16]. Seven patients with *MYB/MYBL1*-altered brainstem gliomas were included in the single-center study from St. Jude Children's Research Hospital. Radiation therapy was used in four out of five patients with treatment information available. All exhibited stable disease as the best response to the therapy [13]. We also reviewed the literature documenting cases of histopathologically confirmed angiocentric gliomas, but without any data on *MYB/MYBL1* alteration available [17–19]. Reported use of a LGG-based regimen consisting of vincristine and carboplatin resulted in disease progression in treated patients ($n = 2$).

Despite the fact that MYB(L1)-altered gliomas represent group of indolent low-grade tumors with reported overall survival reaching 95% at 5 years [13], tumors within brainstem location frequently require therapy. In contrast to reported treatment outcomes, our patient achieved objective response and long-term remission of the disease with radiation sparing approach. Although this is an anecdotal experience based on a single patient, it suggests that an intensive chemotherapy regimen such as HIT-SKK chemotherapy could be more effective for MYB-altered diffuse astrocytomas or angiocentric gliomas localized in the pons.

Our experience further underscores the role of biopsy in patients with brain stem tumors with the distinctive MRI appearance of DIPG in all age groups, but especially in infants, where other entities outside DMG can be encountered. As exemplified by our case, diffuse brainstem gliomas with unknown drivers should be investigated for *MYB* alterations even if they do not histologically bear an angiocentric pattern.

Author contribution Conceptualization: KT, MZ; methodology: KT, MZ, DS, AV, LK, MK; investigation: KT, MZ, DS, AV, LK, MK, VB; writing—original draft: KT, MZ; writing—review and editing: MZ, DS, KT; funding acquisition: MZ, KT, DS, AV, LK. All authors read and approved the final manuscript.

Funding Open access publishing supported by the National Technical Library in Prague. This work was supported by the Charles University Grant Agency GAUK No. 204220 (KT, MZ); PRIMUS/19/MED/06 Charles University Grant Agency, Prague, Czech Republic (MZ, LK, AM, KT); MH CZ–DRO, University Hospital Motol, Prague, Czech Republic (00064203) (DS, AV, MZ); and the Project National Institute for Cancer Research (Programme EXCELES, ID Project No. LX22NPO5102)—Funded by the European Union—Next Generation EU. (MZ, KT, AV).

Availability of data and materials The datasets used and/or analyzed during the current study are available from the corresponding author on reasonable request.

Declarations

Ethics approval and consent to participate Approval for the study herein reported was provided by Institutional Ethics Committee of the Second Faculty of Medicine Charles University in Prague (ethics committee approval 17.6.2020).

Consent for publication The authors of this publication declare that they have obtained the informed consent of the patient's legal representatives for the publication of their anonymized data for this case report.

Conflict of interest The authors declare no competing interests.

References

1. Roux A, Pallud J, Saffroy R, Edjlali-Goujon M, Debily MA, Boddaert N, Sanson M, Puget S, Knafo S, Adam C et al (2020)

High-grade gliomas in adolescents and young adults highlight histomolecular differences from their adult and pediatric counterparts. Neuro Oncol 22:1190–1202. https://doi.org/10.1093/neuonc/noaa024
2. Mackay A, Burford A, Carvalho D, Izquierdo E, Fazal-Salom J, Taylor KR, Bjerke L, Clarke M, Vinci M, Nandhabalan M et al (2017) Integrated molecular meta-analysis of 1,000 pediatric high-grade and diffuse intrinsic pontine glioma. Cancer Cell 32:520–537. https://doi.org/10.1016/j.ccell.2017.08.017
3. Louis DN, Ohgaki H, Wiestler OD, Cavenee WK, Burger PC, Jouvet A, Scheithauer BW, Kleihues P (2007) The 2007 WHO Classification of Tumours of the Central Nervous System. Acta Neuropathol 114:97–109. https://doi.org/10.1007/s00401-007-0243-4
4. Agaimy A, Terracciano LM, Dirnhofer S, Tornillo L, Foerster A, Hartmann A, Bihl MP (2009) V600E BRAF mutations are alternative early molecular events in a subset of KIT/PDGFRA wild-type gastrointestinal stromal tumours. J Clin Pathol 62:613–616. https://doi.org/10.1136/jcp.2009.064550
5. Castel D, Philippe C, Calmon R, Le Dret L, Truffaux N, Boddaert N, Pages M, Taylor KR, Saulnier P, Lacroix L et al (2015) Histone H3F3A and HIST1H3B K27M mutations define two subgroups of diffuse intrinsic pontine gliomas with different prognosis and phenotypes. Acta Neuropathol 130:815–827. https://doi.org/10.1007/s00401-015-1478-0
6. Jones DT, Kocialkowski S, Liu L, Pearson DM, Backlund LM, Ichimura K, Collins VP (2008) Tandem duplication producing a novel oncogenic BRAF fusion gene defines the majority of pilocytic astrocytomas. Can Res 68:8673–8677. https://doi.org/10.1158/0008-5472.CAN-08-2097
7. Hoffman LM, Veldhuijzen van Zanten SEM, Colditz N, Baugh J, Chaney B, Hoffmann M, Lane A, Fuller C, Miles L, Hawkins C et al (2018) Clinical, radiologic, pathologic, and molecular characteristics of long-term survivors of diffuse intrinsic pontine glioma (DIPG): a collaborative report from the International and European Society for Pediatric Oncology DIPG Registries. J Clin Oncol Off J Am Soc Clin Oncol 36:1963–1972. https://doi.org/10.1200/JCO.2017.75.9308
8. Kramm CM, Butenhoff S, Rausche U, Warmuth-Metz M, Kortmann RD, Pietsch T, Gnekow A, Jorch N, Janssen G, Berthold F et al (2011) Thalamic high-grade gliomas in children: a distinct clinical subset? Neuro Oncol 13:680–689. https://doi.org/10.1093/neuonc/nor045
9. Rutkowski S, Gerber NU, von Hoff K, Gnekow A, Bode U, Graf N, Berthold F, Henze G, Wolff JE, Warmuth-Metz M et al (2009) Treatment of early childhood medulloblastoma by postoperative chemotherapy and deferred radiotherapy. Neuro Oncol 11:201–210. https://doi.org/10.1215/15228517-2008-084
10. Capper D, Jones DTW, Sill M, Hovestadt V, Schrimpf D, Sturm D, Koelsche C, Sahm F, Chavez L, Reuss DE et al (2018) DNA methylation-based classification of central nervous system tumours. Nature 555:469–474. https://doi.org/10.1038/nature26000
11. Bandopadhayay P, Ramkissoon LA, Jain P, Bergthold G, Wala J, Zeid R, Schumacher SE, Urbanski L, O'Rourke R, Gibson WJ et al (2016) MYB-QKI rearrangements in angiocentric glioma drive tumorigenicity through a tripartite mechanism. Nat Genet 48:273–282. https://doi.org/10.1038/ng.3500
12. Figarella-Branger D, Appay R, Metais A, Tauziede-Espariat A, Colin C, Rousseau A, Varlet P (2022) The 2021 WHO Classification of Tumours of the Central Nervous System. Ann Pathol 42:367–382. https://doi.org/10.1016/j.annpat.2021.11.005
13. Chiang J, Harreld JH, Tinkle CL, Moreira DC, Li X, Acharya S, Qaddoumi I, Ellison DW (2019) A single-center study of the clinicopathologic correlates of gliomas with a MYB or MYBL1 alteration. Acta Neuropathol 138:1091–1092. https://doi.org/10.1007/s00401-019-02081-1
14. Ryall S, Zapotocky M, Fukuoka K, Nobre L, Guerreiro Stucklin A, Bennett J, Siddaway R, Li C, Pajovic S, Arnoldo A et al (2020) Integrated molecular and clinical analysis of 1,000 pediatric low-grade gliomas. Cancer Cell 37:569–583. https://doi.org/10.1016/j.ccell.2020.03.011
15. Ampie L, Choy W, DiDomenico JD, Lamano JB, Williams CK, Kesavabhotla K, Mao Q, Bloch O (2016) Clinical attributes and surgical outcomes of angiocentric gliomas. J Clin Neurosci: Off J Nuerosurg Soc Australas 28:117–122. https://doi.org/10.1016/j.jocn.2015.11.015
16. D'Aronco L, Rouleau C, Gayden T, Crevier L, Decarie JC, Perreault S, Jabado N, Bandopadhayay P, Ligon KL, Ellezam B (2017) Brainstem angiocentric gliomas with MYB-QKI rearrangements. Acta Neuropathol 134:667–669. https://doi.org/10.1007/s00401-017-1763-1
17. Chan E, Bollen AW, Sirohi D, Van Ziffle J, Grenert JP, Kline CN, Tihan T, Perry A, Gupta N, Solomon DA (2017) Angiocentric glioma with MYB-QKI fusion located in the brainstem, rather than cerebral cortex. Acta Neuropathol 134:671–673. https://doi.org/10.1007/s00401-017-1759-x
18. Almubarak AO, Alahmari A, Al Hindi H, AlShail E (2020) Angiocentric glioma of brainstem. Neurosciences 25:416–420. https://doi.org/10.17712/nsj.2020.5.20200026
19. Weaver KJ, Crawford LM, Bennett JA, Rivera-Zengotita ML, Pincus DW (2017) Brainstem angiocentric glioma: report of 2 cases. J Neurosurg Pediatr 20:347–351. https://doi.org/10.3171/2017.5.PEDS16402

Příloha 3

Trkova K, Sumerauer D, Bubenikova A, Krskova L, Vicha A, Koblizek M, Zamecnik J, Jurasek B, Kyncl M, Malinova B, Ondrova B, Jones DTW, Sill M, Strnadova M, Stolova L, Misove A, Benes V 3rd, Zapotocky M. Clinical and molecular study of radiation-induced gliomas. ***Sci Rep.*** 2024 Feb 7;14(1):3118. doi: 10.1038/s41598-024-53434-0. PMID: 38326438; PMCID: PMC10850080. **[IF 4.6]**

Autorský podíl: Genetické a epigenetické testování – Sangerovo sekvenování, methylační array, analýza molekulárních a klinických dat, příprava publikace a revizí publikace.

scientific reports

Check for updates

OPEN

Clinical and molecular study of radiation-induced gliomas

Katerina Trkova[1,2,3], David Sumerauer[1,2,3], Adela Bubenikova[6], Lenka Krskova[1,2,4], Ales Vicha[1,2,3], Miroslav Koblizek[1,2,4], Josef Zamecnik[1,2,4], Bruno Jurasek[5], Martin Kyncl[2,5], Bela Malinova[7], Barbora Ondrova[8], David T. W. Jones[9,10,11], Martin Sill[9,10,11], Martina Strnadova[4], Lucie Stolova[3], Adela Misove[1,2,3], Vladimir Benes III[2,6] & Michal Zapotocky[1,2,3]✉

In this study, we provide a comprehensive clinical and molecular biological characterization of radiation-induced gliomas (RIG), including a risk assessment for developing gliomas. A cohort of 12 patients who developed RIG 9.5 years (3–31 years) after previous cranial radiotherapy for brain tumors or T-cell acute lymphoblastic leukemia was established. The derived risk of RIG development based on our consecutive cohort of 371 irradiated patients was 1.6% at 10 years and 3.02% at 15 years. Patients with RIG glioma had a dismal prognosis with a median survival of 7.3 months. We described radiology features that might indicate the suspicion of RIG rather than the primary tumor recurrence. Typical molecular features identified by molecular biology examination included the absence of *Histon3* mutation, methylation profile of pedHGG-RTK1 and the presence of recurrent *PDGFRA* amplification and *CDKN2A/B* deletion. Of the two long-term surviving patients, one had gliomatosis cerebri, and the other had pleomorphic xanthoastrocytoma with BRAF V600E mutation. In summary, our experience highlights the need for tissue diagnostics to allow detailed molecular biological characterization of the tumor, differentiation of the secondary tumor from the recurrence of the primary disease and potentially finding a therapeutic target.

Radiotherapy (RT) is an essential component of therapy for both solid and, mainly in the past, hematological malignancies in the pediatric population. RT improves the outcome of pediatric patients but is also associated with long-term risks. These can be observed especially in children with long-term follow-up[1]. One of the most serious risks is the development of radiation-induced gliomas (RIGs), which have been described in patients primarily treated mainly for acute lymphoblastic leukemia (ALL) and central nervous system (CNS) malignancies by cranial RT[2,3]. Anamnestic information about previous radiotherapy of the cranium in the treatment of the primary diagnosis is always crucial in the management of subsequent diagnostic procedures. It is necessary to use advanced diagnostic tools to reliably distinguish them from the recurrence of primary CNS tumors or from primary high-grade glioma. Radiological features to distinguish RIG from sporadic tumors have not yet been comprehensively described. Consequently, most RIG histologically fulfill the characteristics of high-grade gliomas, and it is difficult to distinguish them from their primary counterparts at this diagnostic level[4,5]. However, significant progress is now being made in their molecular biological characterization[6,7]. Unlike their primary counterparts, RIG do not usually carry the typical mutations in the *Histon3, IDH1/2 or BRAF* genes[1,8,9]. Based

[1]Prague Brain Tumor Research Group, Second Faculty of Medicine, Charles University and University Hospital Motol, V Uvalu 84, 15006 Prague 5, Czech Republic. [2]Center for Pediatric Neuro-Oncology, University Hospital Motol, V Uvalu 84 , 15006 Prague 5, Czech Republic. [3]Department of Pediatric Hematology and Oncology, Second Faculty of Medicine, Charles University Prague and University Hospital Motol, V Uvalu 84, 15006 Prague 5, Czech Republic. [4]Department of Pathology and Molecular Medicine, Second Faculty of Medicine, Charles University Prague and University Hospital Motol, V Uvalu 84, 15006 Prague 5, Czech Republic. [5]Department of Radiology, Second Faculty of Medicine, Charles University Prague and University Hospital Motol, V Uvalu 84, 15006 Prague 5, Czech Republic. [6]Department of Neurosurgery, Second Faculty of Medicine, Charles University Prague and University Hospital Motol, V Uvalu 84, 15006 Prague 5, Czech Republic. [7]Department of Oncology, Second Faculty of Medicine, Charles University Prague and University Hospital Motol, V Uvalu 84, 15006 Prague 5, Czech Republic. [8]Proton Therapy Center Czech, Budínova 1a, 180 00 Prague, Czech Republic. [9]Division of Pediatric Glioma Research, Hopp Children's Cancer Center (KiTZ), Heidelberg, Germany. [10]National Center for Tumor Diseases (NCT), NCT Heidelberg, a partnership between DKFZ and Heidelberg University Hospital, Heidelberg, Germany. [11]German Cancer Research Center (DKFZ), Heidelberg, Germany. ✉email: michal.zapotocky@fnmotol.cz

on methylation profiling, RIG mostly clustered within the GBM_pedRTK1 methylation group. In addition to *TP53* mutations, *PDGFRA* amplification and *CDKN2A/B* deletion are the most frequently described molecular alterations in RIG[6,7].

RIGs are characterized by an aggressive clinical course with a poor prognosis[1,3,10]. Treatment regimens are not defined and include modalities used to treat primary high-grade gliomas. Unfortunately, these procedures have no curative potential in the majority of patients[10]. Here, we performed a single-institution retrospective study of 12 RIG patients with complete clinical, imaging and comprehensive molecular-biological data. We have attempted to define the radiological characteristics of RIG and to present detailed clinical information on each case, including two rare cases of RIG long-term survivors. We present comprehensive genetic and epigenetic data of the examined tumor samples. Due to the availability of follow-up in patients from the primary treatment cohort, we present a unique statistical dataset on the risk of developing RIG in irradiated patients.

Materials and methods

Patient cohort and tumor samples

This study was conducted upon ethics approval (Institutional Ethics Committee of the Second Faculty of Medicine Charles University in Prague 17.6.2020). The authors of this publication declare that they have obtained the informed consent of the patient's legal representatives for the publication of their anonymized data for this study. All methods were performed in accordance with the relevant guidelines and regulations.

Patients with RIG located in the radiation field and fulfilling the Cahan's criteria were identified[11]. Patients' charts were reviewed to obtain demographic information, primary tumor histology, tumor location and histology at the time of RIG diagnosis. Archival tissue blocks of the RIG tumors were retrieved and used for subsequent molecular analyses as detailed below.

DNA extraction and direct sequencing

The most representative tissue blocks, containing the maximum percentage of tumor tissue, were selected by the pathologist. Genomic DNA was extracted from each formalin-fixed, paraffin-embedded (FFPE) tissue block using a QIAamp DNA FFPE Tissue Kit (Qiagen, Germany) or from fresh frozen sections using TRIzol Reagent (Life Technologies, Merelbeke, Belgium). The hotspot mutations at codons 27 and 34 of *H3F3A*, codon 27 of *HIST1H3B*, codon 600 of *BRAFex15*, codons 546 and 656 of *FGFR1ex12*, and codon of *FGFRex14* were examined using previously described primer pairs[12–14]. Amplification was performed using 2 × PCRBIO HS Taq Mix Red (PCR Biosystems Ltd., London, UK). The PCR products were electrophoresed in a 1.5% agarose gel and recovered using the Gel DNA Fragments Extraction Kit (Geneaid, Taiwan). Direct Sanger sequencing was performed using BigDye Terminator v 3.1 chemistry (Life Technologies) and an ABI PRISM 3130 genetic analyzer (Applied Biosystems). The results were analyzed using Chromas lite 2.01 (Technelysium, Pty Ltd., Brisbane, Australia).

Genome-wide DNA methylation profiling

DNA methylation was evaluated in eight RIG with the Infinium MethylationEPIC BeadChip Kit (Illumina, San Diego, CA, USA). A total of 250 ng of DNA from fresh frozen tumor tissue or FFPE was treated with bisulfite conversion using the ZymoResearch EZ DNA Methylation kit (Zymo Research Corp, Irvine, CA, USA). The Infinium HD Methylation Assay was performed according to the manufacturer's explicit specifications. The methylation class was established using web-based analysis via https://www.molecularneuropathology.org/. Copy number variation (CNV) analysis was performed by the conumee Bioconductor package[15].

T-SNE analysis was performed as described previously using a reference cohort of primary HGG subgroups as well as a published RIG dataset by Deng et al.[7,15].

Next-generation sequencing

The DNA NGS VariantPlex HS Solid Tumor kit (Archer) (Supplementary data) was used following the manufacturer´s instructions. DNA was extracted from FFPE sections (QIAamp DNA FFPE Tissue kit, Qiagen) followed by library preparation. Anchored Multiplex polymerase chain reaction amplicons were sequenced on an Illumina MiSeq, and the data were analyzed using Archer software.

Radiology

All patients were scanned either during scheduled follow-up sessions or extraordinarily in cases of neurological symptoms. Various MRI scanners certified for diagnostic imaging have been used, all of which use a 1.5 Tesla magnetic field. In all cases, the examination protocol included T1- and T2-weighted imaging, FLAIR imaging, DWI/ADC evaluation and T1-weighted imaging with gadolinium-based contrast agent (GBCA) administration. MRI findings were evaluated within the central tumor board by a radiology expert.

Statistics

The normality of the data was evaluated according to Shapiro—Wilk's test. Overall survival analysis was analyzed according to the Kaplan—Meier method with p values derived from the log-rank test. The hazard model function in time-to-event analysis was applied for the evaluation of mortality and RIG-development risk over time. All calculations were performed in the open-source R environment (v4.1.2). Graphical interpretations were modeled in OriginPro software (OriginLab Corporation).

Results

Demographics and cumulative risk of RIG development

Between 2000 and 2022, a total of 12 RIG patients were diagnosed at our institution. All patients had received previous treatment with RT for a primary CNS tumor or T-ALL. Three of these patients were originally treated in the 1980s and 1990s. One patient was referred from abroad. Remaining 8 patients were diagnosed and treated for primary malignancy between 2000 and 2015. All 12 patients were used for survival analysis, radiological analysis and molecular profiling. The RIG patient group consisted of six males and six females. Their primary diagnoses comprised T-ALL ($n=3$), ependymoma ($n=4$), choroid-plexus carcinoma ($n=1$), medulloblastoma ($n=2$), meningioma ($n=1$) and skull chondrosarcoma ($n=1$). Age at the primary diagnosis ranged between 2 and 11 years (median 9 years). Patients underwent photon radiotherapy at doses ranging from 12 to 59.4 Gy (median 50.65 Gy). They developed RIG in the median 9.5 years after the primary diagnosis in the range of 3 to 31 years. All RIGs were located in the radiation field and fullfiled the Cahan's criteria[11]. RIG tumor samples were histologically reported as glioblastoma gr. 4 ($n=7$), anaplastic astrocytoma gr. 3 ($n=1$), anaplastic ganglioglioma gr. 3 ($n=1$), gliomatosis cerebri gr. 3 ($n=1$) and embryonal high-grade tumors ($n=2$). The clinical, demographic and molecular biological characteristics of the RIG patients are summarized in Table 1.

To calculate the cumulative risk of RIG development after RT, a single institutional cohort of patients with irradiated craniums between 2000 and 2015 was established consisting of 371 cases (219 primary brain tumors and 152 acute lymphoblastic leukemias) with follow-up censored by the end of 2022. Median time of follow-up was 13.3 years. Eight out of our 12 patients were treated within this range and developed RIG (six after brain tumor and two after ALL). Based on hazard functions, the derived risk of RIG development was 1.60% at 10 years

ID	Primary diagnosis	RT dose (Gy) (Fractions)	Age primary Dx (y)	Age RIG (y)	RIG OS (m)	RIG location	Histology	Methylation class	CS	CNV	SNV	Therapy
RIG1	EPE	50.4* (28×1.8)	11	29	5	PF	GBM	RTK1c	0.9	neg	ND	50.4 Gy (28×1.8), TMZ
RIG2	CPC	54 (30×1.8)	6	11	3	Right thalamus	GBM	RTK1c	0.28	CDKN2A del, MYCN amp	ND	TMZ
RIG3	EPE	54* (30×1.8)	9	18	3	PF	AA	no match	<0.3	ND	No SNV	COMBAT
RIG4	MBL	59.4* (33×1.8)	10	21	6	PF	HG ET	RTK1c	0.67	PDGFRA amp, CDKN2A del	No SNV	MEMMAT
RIG5	T-ALL	18 (12×1.5)	7	11	8	Right F lobe	GBM	RTK1b	1	neg	No SNV	None
RIG6	T-ALL	12 (8×1.5)	10	20	alive (108)	Both hemispheres	GC	failed	ND	ND	ND	50.4 Gy (28×1.8), TMZ
RIG7	MBL	55.8* (31×1.8)	11	15	10	PF	GBM	RTK1c	0.45	PDGFRA amp, CDK4 amp	ROS1 R2035C	45 Gy (25×1.8), TMZ
RIG8	EPE	59.4 (33×1.8)	2	7	12	PF	GBM	RTK1c	0.96	CDKN2A del	PIK3CA D454_P458del insA	BVZ
RIG9	T-ALL	12 (8×1.5)	5	9	15	Left P lobe	HG ET	RTK1c	0.99	PDGFRA amp	No SNV	54 Gy (30×1.8), TMZ
RIG10	MNG	45 (SRS)	9	23	alive (99)	Left T lobe	aGG	PXA	0.99	CDKN2A del	BRAF V600E	RT/CHT
RIG11	EPE	50.4 (28×1.8)	5	37	3	Right P lobe	GBM	ND	ND	ND	ND	60 Gy (30×2), TMZ
RIG12	CSa	50.4 (28×1.8)	10	45	2	Right T lobe	GBM	RTK1	0.73	PDGFRA amp, CDKN2A del	TP53 c.560-1G>APTEN R130*	None

Table 1. Clinical, demographic and molecular data. Radiation doses marked with * indicate that craniospinal radiation was used. AA—anaplastic astrocytoma grade 3, aGG—anaplastic ganglioglioma grade 3, CNV—copy number variant, CPC—choroid plexus carcinoma, COMBAT—combined metronomic low dose biodifferentiating antiangiogenic therapy, CSa—chondrosarcoma, Dx—diagnosis, EPE—ependymoma, F frontal, GC—gliomatosis cerebri, GBM—glioblastoma, Gy—gray, HG ET—high grade embryonal tumor, m—month, MBL—medulloblastoma, MEMMAT—Medulloblastoma European Multitarget Metronomic Anti-Angiogenic Trial, MNG—meningioma, NA—not available, ND—not done, P—parietal, PF—posterior fossa, PXA—Pleomorphic xanthoastrocytoma, RIG—radiation-induced glioma, RTK1c—Glioblastoma, pediatric RTK1 type, subtype C, RTK1b—Glioblastoma, pediatric RTK1 type, subtype B, SNV—single nucleotide variant, SRS—stereotactic radiosurgery, T—temporal, T-ALL—T-cell acute lymphoblastic leukemia, TMZ—temozolomide, Y—year.

and 3.02% at 15 years (Fig. 1A). The hazard difference between the CNS tumor group and leukemias was not significantly different ($p = 0.72$) (Fig. 1B). Table 2 displays the increasing risk of developing RIG with the time elapsed since the primary diagnosis.

Furthermore, we aimed to estimate the prevalence of RIG among late events occurring later than 3 years after cranial radiation therapy. We identified all patients treated with radiation therapy for primary brain tumors between 2000 and 2015 (219 primary brain tumors as mentioned above). All intraaxial intracranial tumor recurrences/progressions and secondary malignancies occurring later than 3 years from radiation therapy were evaluated. Altogether, 30 patients with late events were identified, 28 of whom underwent histopathological verification of the subsequent tumor. The RIG diagnosis was confirmed in 6 patients, representing 21.4% of all histologically verified late events.

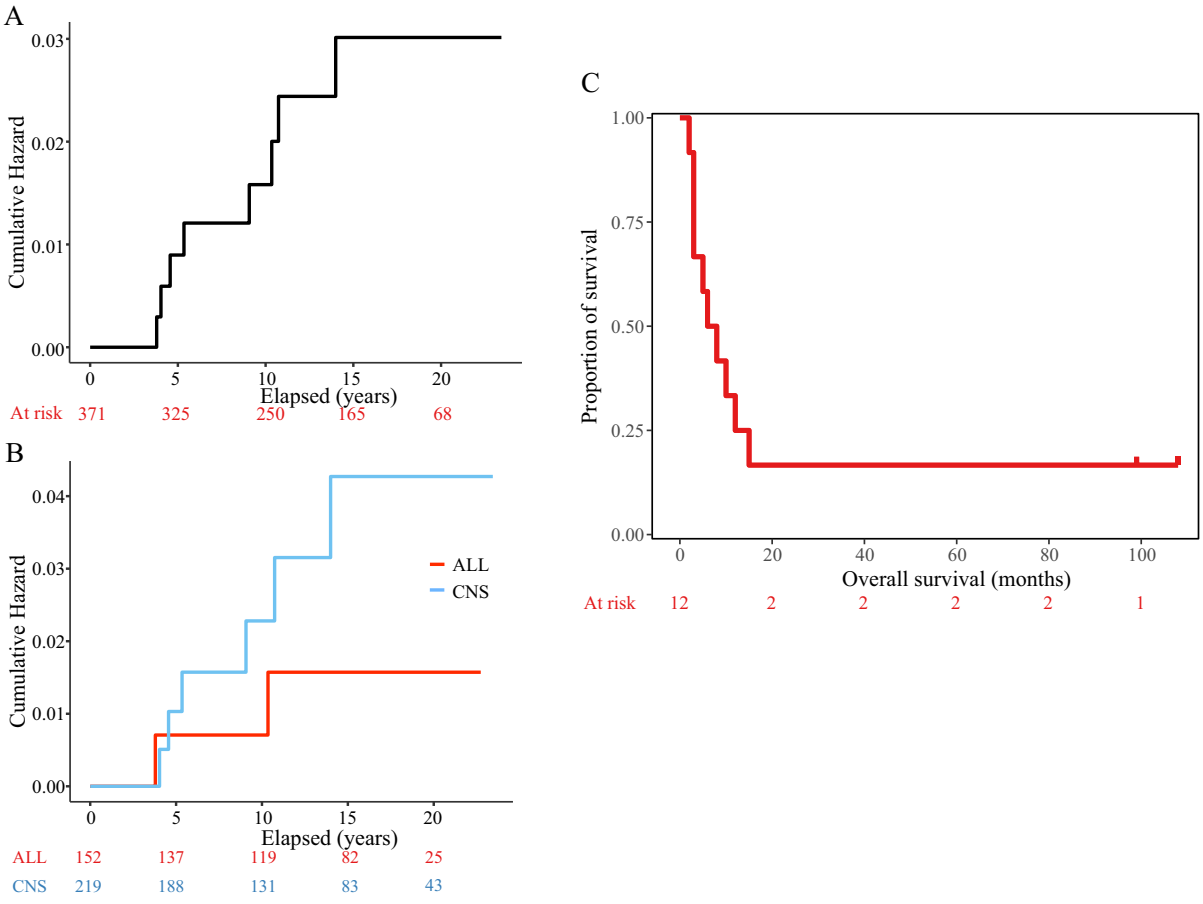

Figure 1. Risk analysis of the development of RIG and overall survival analysis. (**A**) Overall hazard function evaluating the risk of RIG development within the primary cohort after RT. (**B**) Analogous demonstration of the risk of RIG development when divided into two groups based on primary diagnosis (CNS group ($n = 219$) vs ALL group ($n = 152$)). (**C**) Overall survival of patients with RIG.

Years	Risk of RIG development (%)
3	0.28
4	0.89
5	1.20
9	1.60
11	2.45
13	3.02

Table 2. Derived risks of RIG development based on Hazard Function seen in Fig. 1A.

Treatment and outcome of RIG

RIG therapy is very challenging because it affects a vulnerable population of patients previously treated for malignancy and dealing with various late effects and chronic medical conditions. The available treatment options are thus limited and sometimes cannot be used at all.

Similar to primary pediatric high-grade glioma, surgery is an essential component of treatment. Complete resection of the tumor was attempted and achieved in three cases (RIG1, 9, 10). In all other cases except for RIG8, only partial resection or biopsy was performed. In addition to surgery, patients were treated mostly by another course of radiotherapy combined with temozolomide chemotherapy ($n=6$). RIG4, originally diagnosed by histology as an embryonal high-grade tumor, was treated by oral metronomic combined chemotherapy as per Medulloblastoma European Multitarget Metronomic Anti-Angiogenic Trial (MEMMAT)[16]. Patients RIG2 and RIG3, who were unfit to receive radiotherapy, were treated with a palliative oral chemotherapy regimen. In the case of RIG5 and RIG12, no anticancer treatment was initiated because of the very poor clinical and neurological condition of the patients. RIG8 was initially diagnosed due to the new occurrence of cranial nerve palsies as brainstem radiation necrosis 5 years after posterior fossa ependymoma irradiation. The diagnosis was based solely on MRI radiological appearance of brain stem involvement, and the patient was treated with repeated courses of bevacizumab. At the time of clinical deterioration and tumor confirmation on imaging, no further treatment was pursued, and the true histological origin of the tumor was discovered only postmortem.

There were two long-term survivors in our RIG cohort, patients RIG6 and RIG10. Patient RIG6 was diagnosed with T-ALL at the age of 10 years. She was exposed to cranial radiotherapy at a dose of 12 Gy at that time as per the protocol treatment[17]. She developed RIG, radiologically fitting to the diagnosis of gliomatosis cerebri, histopathologically described as anaplastic astrocytoma gr. 3 (IDH1 wild-type) from the needle biopsy. She then underwent radiotherapy to the affected brain areas to a dose of 50.4 Gy and concomitant chemotherapy with temozolomide. Unfortunately, only four months after the end of the radiotherapy course was progression of the disease into the frontal lobe detected on MRI. The patient was indicated for palliative reirradiation at a dose of 30.6 Gy and metronomic oral chemotherapy using the combined metronomic low dose biodifferentiating antiangiogenic therapy (COMBAT) regimen for 21 months[18]. Since then, the patient has had a stable disease (20 years from diagnosis of ALL and 7 years from the RIG diagnosis) in a remarkably good clinical condition.

RIG10 presented with a primary diagnosis of meningioma in the left temporal area. The tumor was resected, and a small residual tumor was irradiated by stereotactic radiosurgery (Leksell gamma knife) to a dose of 45 Gy. He developed RIG after 14 years, histopathologically described as anaplastic ganglioglioma WHO gr. 3 with BRAF V600E mutation. The tumor was resected, and the patient was treated with radiotherapy and concomitant chemotherapy with temozolomide. Seven years after the diagnosis of RIG, the patient´s tumor relapsed. Complete resection of the tumor recurrence was performed, and the patient was treated with temozolomide chemotherapy. No biological therapy with BRAF/MEK inhibitors has been attempted by the adult neuro-oncology service to date, but he has now been in second complete remission for more than 10 months.

Despite the two long-term survivors, the prognosis of the patients within the RIG cohort is rather dismal. In our cohort, ten patients died with a median survival of only 7.3 months after the diagnosis of RIG (Fig. 1C).

Radiological characteristics

The standard MRI sequences were reviewed to describe RIG imaging characteristics. We uncovered various patterns occurring in RIG patients. The first largest group ($n=7$, RIG1, 2, 4, 5, 7, 9, 10, and 12) was represented by T1 hypo-intense and T2 hyperintense lesions with perilesional edema in FLAIR and peripheral contrast enhancement with an arcuate pattern. Furthermore, two other patients exhibited different contrast enhancement with remarkably diffuse patterns (RIG3 and 11). Finally, the third radiologically distinct tumors showed little or no contrast enhancement at the time of lesion detection ($n=2$, RIG6 and 8) (Fig. 2).

Molecular biology

Out of 12 patients, 10 had a tissue sample available and sufficient quality DNA for the methylation array, 10 patients for direct sequencing, and 8 for next generation sequencing (NGS). Whole-genome DNA methylation profiling was performed to evaluate epigenetic differences between RIGs and primary pediatric high-grade gliomas. Heidelberg classifier v12.3 classified 8 samples as "Pediatric high-grade glioma, subclass RTK1" (pedHGG-RTK1) with calibrated scores (CS) over 0.9 in 5 cases and one sample as "Pleomorphic xanthoastrocytoma" with CS = 0.99. Two samples did not achieve a sufficient score to match any class. Interestingly, all pedHGG-RTK1 samples clustered with the methylation class "Glioblastoma IDH-wildtype, subclass midline" in the 11b4 version of the classifier with variable CS ranging from 0.21 to 0.99. Furthermore, t-SNE analysis was performed using a reference cohort and a previously published RIG cohort[7]. This demonstrated that our samples clustered with pedHGG-RTK1c ($n=7$), pedHGG-RTK1b ($n=2$), and PXA ($n=1$) (Fig. 3).

Copy number variations (CNVs) inferred from DNA methylation data were analyzed to evaluate possible recurrent CNV changes among RIG. *PDGFRA* amplification was found in ($n=4$, 44% of samples), *CDKN2A/B* homozygous deletion in ($n=5$, 55.5% of samples). Other high-level amplifications were detected in single patients, such as *CDK4* amplification (RIG7) and *MYCN* amplification (RIG2). Recurrent chromosomal alterations were also observed, in particular 1p loss ($n=6$; 66.6%), 1q gain ($n=5$; 55.5%), and various partial 6q deletions ($n=4$; 44.0%).

Proportion of our RIG cases presented with infiltration of midline structures; therefore, we performed direct sequencing focusing on mutations in *Hist1H3B* and *H3F3A* in all patients with available material (except for RIG6 and 11). Furthermore, none of these cases were positive for H3 K27M or H3 G34R mutations, which are usually present in a subset of pediatric HGG. Further sequencing involved other drivers typical for HGG, such

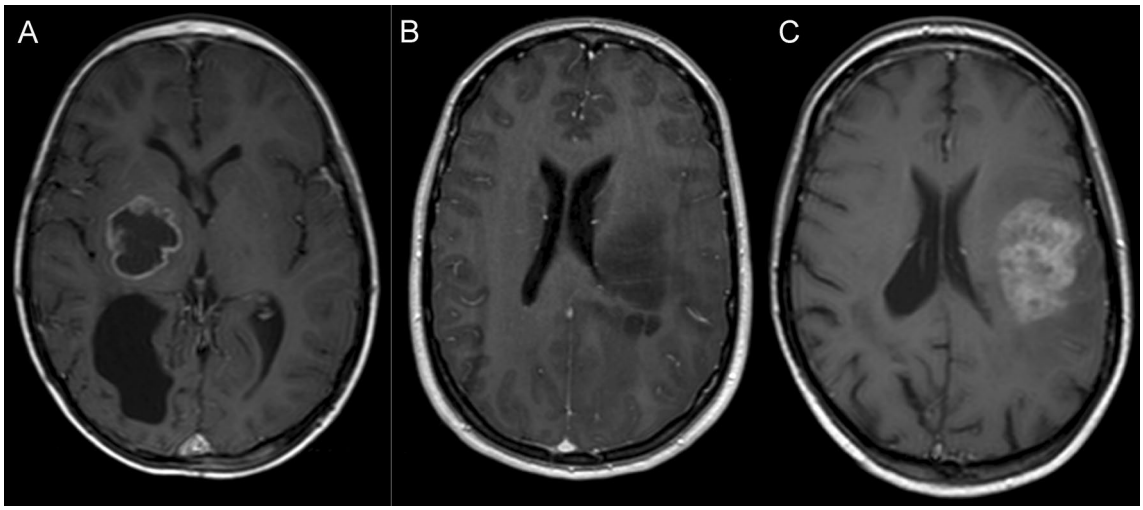

Figure 2. Radiological characteristics of RIG. Examples of radiological subgroups of RIG according to the character of contrast enhancement: (**A**) arcuate pattern enhancement—RIG2, (**B**) no enhancement—RIG6, (**C**) diffuse enhancement—RIG11.

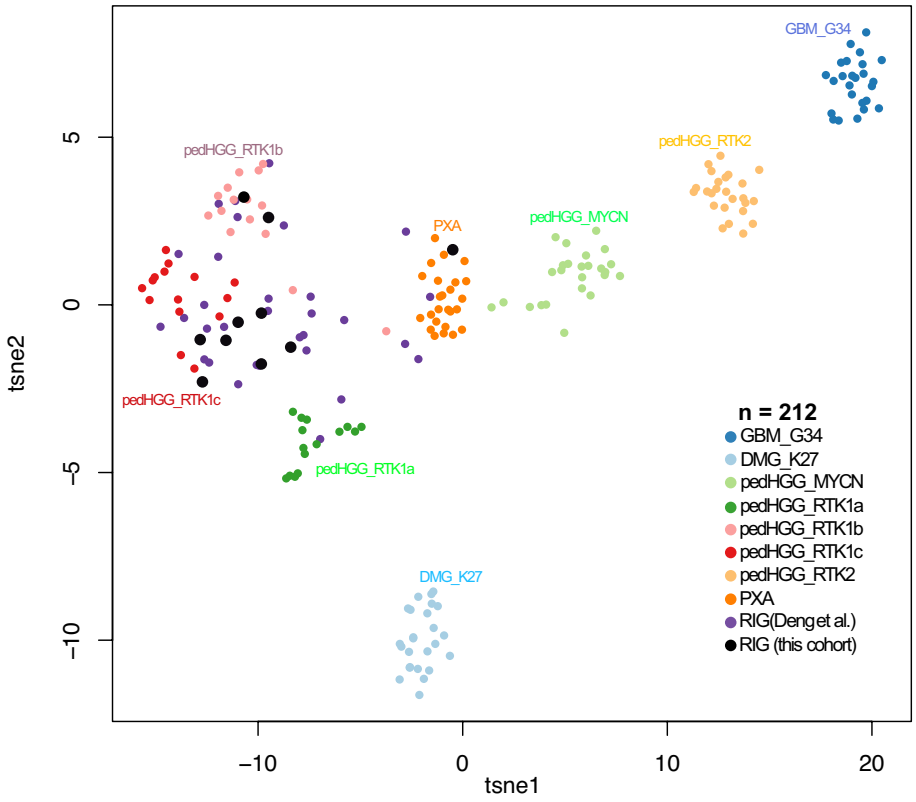

Figure 3. Molecular characterization of RIGs based on methylation profiling. T-SNE analysis demonstrated that the majority of RIG samples from our cohort clustered with the pedHGG-RTK1 subgroup. The previously published cohort of 32 RIG samples (Deng et al.) is shown here, which further validates our data. RIG samples were compared with a cohort of 170 reference samples of histologically and molecularly described CNS tumors. Abbreviations: PXA—pleomorphic xanthoastrocytoma; GBM_G34—Glioblastoma, H3.3 G34 mutant; DMG_K27—diffuse midline glioma H3 K27 mutant; pedHGG_MYCN—pediatric high-grade glioma subclass MYCN; pedHGG_RTK1a—Pediatric high-grade glioma, pediatric RTK1 type, subtype A; pedHGG_RTK1b—Pediatric high-grade glioma, pediatric RTK1 type, subtype B; pedHGG_RTK1c—Pediatric high-grade glioma, pediatric RTK1 type, subtype C; pedHGG_RTK2—Pediatric high-grade glioma, pediatric RTK2 type.

as the *FGFR1*, *IDH1*, and *BRAF* genes. All samples tested wild-type except one sample positive for BRAF V600E corresponding with a case classified as PXA using a methylation array (RIG10).

In addition to the direct sequencing, DNA panel NGS was performed on samples with sufficient quality material ($n = 8$) and revealed additional somatic variants in three cases involving the *PIK3CA*, *PTEN* and *ROS1* genes (Table 1). Interestingly, somatic pathogenic variant in the *TP53* gene was detected in only one case (RIG12). Furthermore, no IDH1/IDH2 mutations were identified.

Discussion

RIG represents serious late sequelae occurring 3–45 years after previous radiation therapy. Our data indicate that RIG represents a frequent late event after cranial irradiation. Strikingly, RIG represented over 20% of all intracranial intraaxial late events occurring later than 3 years after the diagnosis. Therefore, RIG should be excluded in all cases with suspected recurrence or progression after this time point. Furthermore, we presented a model estimating the risk of RIG development using a homogenous consecutive cohort treated in our center over a 15-year period. We have been able to estimate that the cumulative RIG risk will reach 3% after 15 years. Because our cohort and other published cohorts reported patients developing RIG even 35 to 45 years[19] after radiation therapy, it is very likely that the actual risk of developing RIG exceeds 3% more than 15 years after the primary tumor RT. Consistent with our findings, the increasing cumulative incidence of RIG development was also demonstrated using SEER data[20]. Based on SEER data, the risk of RIG development was estimated to be between 1 and 4%, and RIG was responsible for 2 to 10% of all pediatric brain tumor deaths[20].

The radiation doses at the primary diagnosis ranged from 12 to 59.4 Gy, demonstrating that even children who received as little as 12 Gy of neurocranium irradiation for leukemia were at risk of RIG development. This is in keeping with data from CCSS that demonstrated risk of secondary glioma in cases that received over 10 Gy brain irradiation. In the CCSS study, the peak odds ratio was identified at a radiation dose level of 30–44.9 Gy[21].

RIG represented a disease with a dismal prognosis with a median overall survival of 7.3 months in our cohort. These results are similarly unfavorable as in primary H3-mutant pediatric HGG. In contrast to these data, two long-term survivors of RIG were reported. One of them was a patient with IDH1 wild-type gliomatosis cerebri that could not be further characterized. Despite the clear documented progression, in the long term (7 years after diagnosis), the disease was therapeutically stabilized by reirradiation (third cycle of radiotherapy for this patient). The second patient with a biologically more favorable tumor profile (PXA) was characterized by the BRAF V600E mutation. Small proportion of RIG tumors were reported to cluster with PXA. They harbor MAPK pathway alterations including genes *RAF1, NTRK2*, but also *BRAF*. Hotspot mutation BRAF V600E has never been reported in previous studies (Table 3).

Comprehensive radiological characterization of RIG is currently lacking in the literature. The uniqueness of our cohort lies in the fact that all patients were examined in one department by one radiology team. Therefore, for the first time, we can provide a comprehensive analysis of a cohort of patients with RIG.

On this basis, we want to emphasize the most common MRI pattern found in patients with radiotherapy-induced gliomas that should be taken into account when evaluating the brain MRI of patients with a history of cranial radiotherapy. If the lesion is peripherally contrast-enhancing with an arcuate pattern, while the lesion is hypointense in T1, hyperintense in T2 and shows perilesional edema in FLAIR, RIG should be part of the differential diagnosis. Nevertheless, other patterns of enhancement were observed in our cohort, suggesting that lack of arcuate enhancement does not exclude RIG diagnosis. Furthermore, it may be challenging to differentiate RIG from radiation necrosis, as they might present with similar MRI features.

Study	Type of study	Patient number	Methylation class	Copy number variations	Focal somatic alterations	Gene fusions
DeSisto et al. (2021)	Multicentric	32	PedRTK1 (25/31) PXA (1/31)	1p loss (10/25), 1q gain (13/25), 13q loss (10/25), 14q loss (10/25),*PDGFRA* gain/amplification (11/31), *CDK4* amplification (6/31), *CDKN2A* loss (9/31), and *BCOR* loss (7/31)	*PDGFRA, CDKN2A, BCOR, BRAF, NF1, TP53, CDK4*	*MET* fusions
Deng et al. (2021)	Multicentric	32	PedRTK1 (29/32), PXA (3/32)	*PDGFRA* amplification (6/9 ALL-RIG; 11/23 MB- RIG), loss of *CDKN2A/B* (4/9 ALL-RIG; 17/23 MB-RIG)	*TP53, CBL, PDGFRA, NTRK2, EGFR, RAF1, ATRX, BCOR*	*PTPRZ1::MET, CAPZA2::MET, FYCO1::RAF1, GFAP1::NTRK2*
Whitehouse et. al (2021)	Metaanalysis	102	Not analyzed	*PDGFRA* amplification(10/21), *CDK4* amplification(4/10), *CDKN2A* deletion(13/28), 1q gain(53%), 1p loss(47%), 13q loss(59%)	*PDGFRA, TP53, ATRX, PTEN, PIK3CA, BRAF, IDH1*	*GTF2I::BRAF*
Trkova et al. (this study)	Single-centre	12	PedRTK1 (9/10), PXA (1/10)	*PDGFRA* amplification (4/9), *CDKN2A/B* deletion(5/9), *CDK4* amplification(1/9), *MYCN* amplification (1/9), 1p loss (6/9), 1q gain(1/9), 6q deletions (4/9)	*BRAF, ROS1, PIK3CA, TP53, PTEN*	not performed

Table 3. Molecular biology characteristic of RIG in the recent studies.

Comprehensive molecular characterization of the tissue from RIG patients proved to be critical to establish correct diagnosis and to identify possible targets for novel therapies. Morphological diagnosis proved to be challenging, as demonstrated in our cohort, with several tumors being reported as a recurrence of the original diagnosis. Whole genome DNA methylation array and subsequent Heidelberg methylation classifier refined the diagnosis in those patients. Overall, RIG cases were classified as pedHGG-RTK1, PXA or no match with insufficient score. Therefore, some cases might benefit from further analysis (for example, t-SNE clustering) to confirm the correct methylation class. In our study, t-SNE analysis was able to cluster tumors reliably with pedHGG-RTK1 or PXA subgroups, including cases with very low calibrated scores. Combining our cohort with a previously published dataset demonstrated that all samples clustered with pedHGG-RTK1b, pedHGG-RTK1c or PXA. CNV analysis inferred from DNA methylation data demonstrated consistent findings with previous studies documenting a high prevalence of *PDGFRA* amplification and *CDKN2A* homozygous deletion[6,7,22]. In addition to these recurrent CNVs, some cases harbored complex CNV changes with amplifications of *CDK4* or *MYCN* genes. DNA sequencing revealed targetable somatic single nucleotide variants (SNVs) in four cases, including BRAF V600E (PXA methylation class) and pathogenic somatic variants in the *PIK3CA, PTEN* and *ROS1* genes. Deng et al. reported high priority targets obtained from RNA sequencing (RNAseq) of RIG samples, including *MET, RAF1* or *NTRK2* gene fusions. Unfortunately, the yields of RNA from our archival tissue were not sufficient to perform RNAseq. Nevertheless, our study and previously published data strongly indicate that comprehensive molecular evaluation of RIG tissue is of utmost importance. The combination of CNV analysis (for PDGFRA amplification), DNA sequencing (targetable driver SNVs) and RNAseq (targetable fusions) significantly increases the chance of uncovering high priority targets in this disease with a dismal prognosis (Table 3).

Although the risk model was provided, radiological and molecular features were evaluated, there are certain limitations to this study. This study is retrospective with relatively small number of patients because of the rarity of RIG. Much larger cohort would be required in order to stratify the risk of RIG development depending on the radiation dose, to determine the role of extent of resection or to further evaluate specific MRI features of this rare disease.

Data availability

The datasets generated and analyzed during the current study are available in the Mendeley Data repository, https://doi.org/10.17632/vpgtz9pzw8.1.

Received: 20 October 2023; Accepted: 31 January 2024
Published online: 07 February 2024

References

1. Ohno, M. *et al.* Assessment of therapeutic outcome and role of reirradiation in patients with radiation-induced glioma. *Radiat. Oncol.* **17**, 85 (2022).
2. Relling, M. V. *et al.* High incidence of secondary brain tumours after radiotherapy and antimetabolites. *Lancet Lond. Engl.* **354**, 34–39 (1999).
3. Maluf, F. C., DeAngelis, L. M., Raizer, J. J. & Abrey, L. E. High-grade gliomas in patients with prior systemic malignancies. *Cancer.* **94**, 3219–3224 (2002).
4. Donson, A. M. *et al.* Unique molecular characteristics of radiation-induced glioblastoma. *J. Neuropathol. Exp. Neurol.* **66**, 740–749 (2007).
5. Brat, D. J. *et al.* Molecular genetic alterations in radiation-induced astrocytomas. *Am. J. Pathol.* **154**, 1431–1438 (1999).
6. DeSisto, J. *et al.* Comprehensive molecular characterization of pediatric radiation-induced high-grade glioma. *Nat. Commun.* **12**, 5531 (2021).
7. Deng, M. Y. *et al.* Radiation-induced gliomas represent H3-/IDH-wild type pediatric gliomas with recurrent PDGFRA amplification and loss of CDKN2A/B. *Nat. Commun.* **12**, 5530 (2021).
8. Paugh, B. S. *et al.* Integrated molecular genetic profiling of pediatric high-grade gliomas reveals key differences with the adult disease. *J. Clin. Oncol. Off. J. Am. Soc. Clin. Oncol.* **28**, 3061–3068 (2010).
9. Nakao, T. *et al.* Radiation-induced gliomas: A report of four cases and analysis of molecular biomarkers. *Brain. Tumor. Pathol.* **34**, 149–154 (2017).
10. Onishi, S. *et al.* Characteristics and therapeutic strategies of radiation-induced glioma: case series and comprehensive literature review. *J. Neurooncol.* **159**, 531–538 (2022).
11. Cahan, W. G., Woodard, H. Q., Higinbotham, N. L., Stewart, F. W. & Coley, B. L. Sarcoma arising in irradiated bone: Report of eleven cases. *Cancer Interdiscip. Int. J. Am. Cancer Soc.* **82**(1), 8–34 (1998).
12. Castel, D. *et al.* Histone H3F3A and HIST1H3B K27M mutations define two subgroups of diffuse intrinsic pontine gliomas with different prognosis and phenotypes. *Acta Neuropathol.* **130**, 815–827 (2015).
13. Agaimy, A. *et al.* V600E BRAF mutations are alternative early molecular events in a subset of KIT/PDGFRA wildtype gastrointestinal stromal tumours. *J. Clin. Pathol.* **62**, 613–616 (2009).
14. Pathak, P. *et al.* Genetic alterations related to BRAF-FGFR genes and dysregulated MAPK/ERK/mTOR signaling in adult pilocytic astrocytoma. *Brain Pathol.* **27**, 580–589 (2017).
15. Capper, D. *et al.* DNA methylation-based classification of central nervous system tumours. *Nature.* **555**, 469–474 (2018).
16. Slavc, I. *et al.* Improved long-term survival of patients with recurrent medulloblastoma treated with a "MEMMAT-like" metronomic antiangiogenic approach. *Cancers.* **14**(20), 5128 (2022).
17. Stary, J. *et al.* Intensive chemotherapy for childhood acute lymphoblastic leukemia: Results of the randomized intercontinental trial ALL IC-BFM 2002. *J. Clin. Oncol. Off. J. Am. Soc. Clin. Oncol.* **32**, 174–184 (2014).
18. Zapletalová, D. *et al.* Metronomic chemotherapy with the COMBAT regimen in advanced pediatric malignancies: A multicenter experience. *Oncology.* **82**(5), 249–260 (2012).
19. Grogan, P. T. *et al.* Case report: Radiographic complete response of radiation-induced glioblastoma to front-line radiotherapy: A report and molecular characterization of two unique cases. *Front. Neurol.* **21**(14), 1099424 (2023).
20. Leary, J. B., Anderson-Mellies, A. & Green, A. L. Population-based analysis of radiation-induced gliomas after cranial radiotherapy for childhood cancers. *Neuro-Oncol. Adv.* **4**(1), vdac159 (2022).
21. Neglia, J. P. *et al.* New primary neoplasms of the central nervous system in survivors of childhood cancer: A report from the childhood cancer survivor study. *J. Natl. Cancer Inst.* **98**, 1528–1537 (2006).

22. Whitehouse, J. P. *et al.* Defining the molecular features of radiation-induced glioma: A systematic review and meta-analysis. *Neuro-Oncol. Adv.* **3**, vdab109 (2021).

Acknowledgements

This work was supported by GAUK No. 204220 (KT, MZ); PRIMUS/19/MED/06 Charles University Grant Agency, Prague, Czech Republic (MZ, LK, AM, KT); MH CZ–DRO, University Hospital Motol, Prague, Czech Republic (00064203) (DS, AV, MZ); The project National Institute for Cancer Research (Program EXCELES, ID Project No. LX22NPO5102)—Funded by the European Union—Next Generation EU. (MZ, KT, AV). Ministry of Health of the Czech Republic, grant nr. NU21-07-00419 (MZ, DS, AV, LK, JZ) and grant nr. NU23-08-00460 (MK, MZ).

Author contributions

Conceptualization, K.T., M.Z.; Methodology, K.T., M.Z., D.S., A.V., L.K., M.K., J.Z., V.B., A.M., M.K., B.J., D.J., M.S., B.M., B.O., M.S., L.S.; Investigation, K.T., M.Z., D.S., A.V., L.K., M.K., J.Z., M.K., B.J., A.B., O.B.; Writing—original draft, K.T., M.Z.; Writing—review and editing, M.Z., D.S., K.T.; Funding acquisition, M.Z., K.T., A.V.; All authors read and approved the final manuscript.

Competing interests

The authors declare no competing interests.

Additional information

Supplementary Information The online version contains supplementary material available at https://doi.org/10.1038/s41598-024-53434-0.

Correspondence and requests for materials should be addressed to M.Z.

Reprints and permissions information is available at www.nature.com/reprints.

Publisher's note Springer Nature remains neutral with regard to jurisdictional claims in published maps and institutional affiliations.